Report No. K-TRAN: KSU-18-1 ▪ FINAL REPORT ▪ August 2018

Kansas Department of Transportation Column Expert: Shear Capacity of Circular Bridge Piers Confined with Fiber-Reinforced Polymer (FRP) Wrapping

AlaaEldin Abouelleil, M.S.
Hayder Rasheed, Ph.D., P.E., F.ASCE

Kansas State University Transportation Center

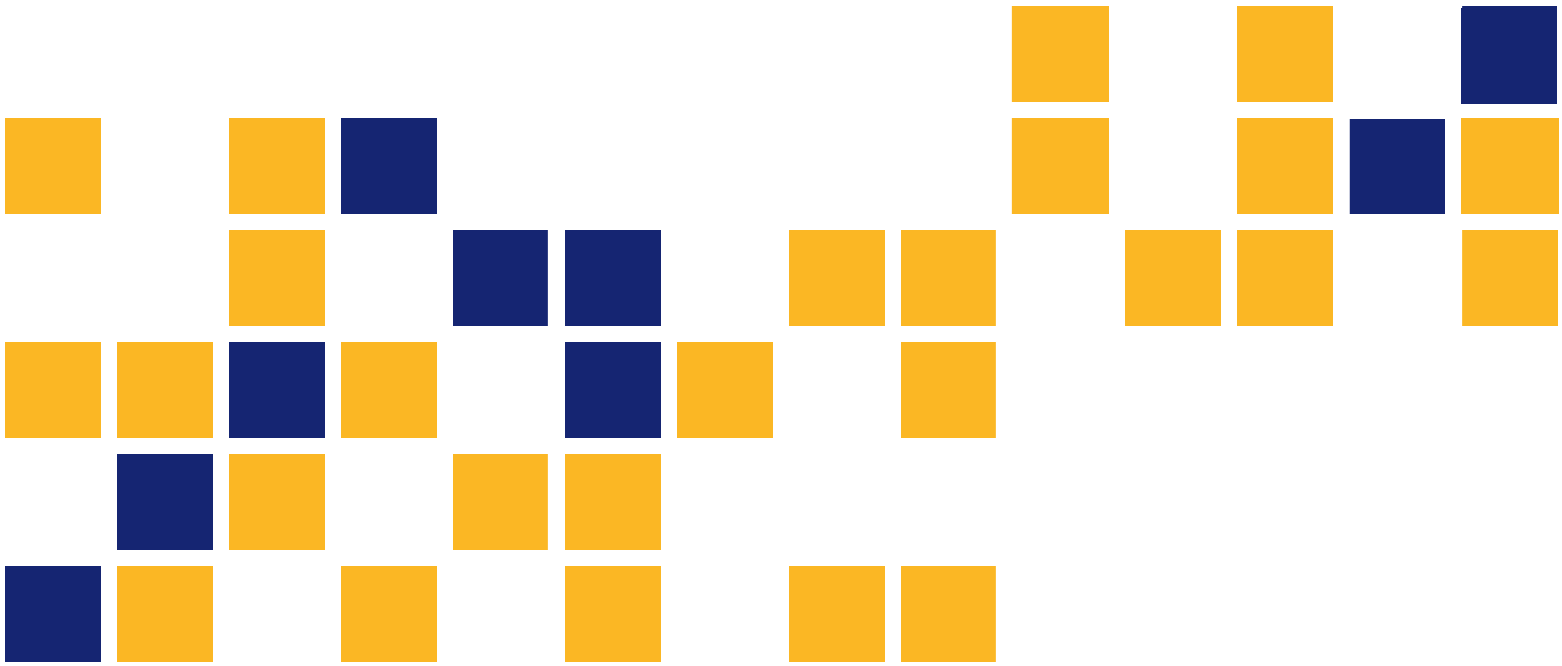

Kansas Department of Transportation

1 Report No. K-TRAN: KSU-18-1	**2 Government Accession No.**	**3 Recipient Catalog No.**
4 Title and Subtitle Kansas Department of Transportation Column Expert: Shear Capacity of Circular Bridge Piers Confined with Fiber-Reinforced Polymer (FRP) Wrapping		**5 Report Date** August 2018 **6 Performing Organization Code**
7 Author(s) AlaaEldin Abouelleil, M.S., Hayder Rasheed, Ph.D., P.E., F.ASCE		**7 Performing Organization Report No.**
9 Performing Organization Name and Address Kansas State University Transportation Center Department of Civil Engineering 2118 Fiedler Hall Manhattan, Kansas 66506		**10 Work Unit No. (TRAIS)** **11 Contract or Grant No.** C2105
12 Sponsoring Agency Name and Address Kansas Department of Transportation Bureau of Research 2300 SW Van Buren Topeka, Kansas 66611-1195		**13 Type of Report and Period Covered** Final Report May 2017–May 2018 **14 Sponsoring Agency Code** RE-0726-01
15 Supplementary Notes For more information write to address in block 9.		

The importance of the analysis of circular columns to accurately predict their ultimate confined (steel and fiber-reinforced polymer [FRP]) capacity under shear-flexure-axial force interaction domain is recognized in light of the extreme load event imposed by the current *AASHTO LRFD Bridge Design Specifications*.

In this study, various procedures for computing the shear strength are reviewed. A formulation conforming to AASHTO (2014) *LRFD Bridge Design Specifications*, based on the Simplified Modified Compression Field Theory, is developed to predict the axial force-shear-moment interaction diagrams of circular confined concrete bridge pier sections reinforced with FRP. Comparisons with a large database of experiments indicate the accuracy of the resulting diagrams. Transverse steel area, spacing, cross section diameter, and applied axial force are the main keys to analyze and increase the shear capacity of the cross section. Treating the cracked concrete as a new different material proved to be a beneficial approach to predict the sections' capacities and behaviors.

Using transverse reinforcement of FRP shows a significant improvement for axial force-bending moment and shear force capacities. The reader is also directed to use KDOT Column Expert for more accurate prediction of the interaction diagrams.

17 Key Words Circular Columns, Shear Capacity, Fiber-Reinforced Polymer Wrapping, Software		**18 Distribution Statement** No restrictions. This document is available to the public through the National Technical Information Service www.ntis.gov.	
19 Security Classification (of this report) Unclassified	**20 Security Classification (of this page)** Unclassified	**21 No. of pages** 96	**22 Price**

Form DOT F 1700.7 (8-72)

This page intentionally left blank.

Kansas Department of Transportation Column Expert: Shear Capacity of Circular Bridge Piers Confined with Fiber-Reinforced Polymer (FRP) Wrapping

Final Report

Prepared by

AlaaEldin Abouelleil, M.S.
Hayder Rasheed, Ph.D., P.E., F.ASCE

Kansas State University Transportation Center

A Report on Research Sponsored by

THE KANSAS DEPARTMENT OF TRANSPORTATION
TOPEKA, KANSAS

and

KANSAS STATE UNIVERSITY TRANSPORTATION CENTER
MANHATTAN, KANSAS

August 2018

PREFACE

The Kansas Department of Transportation's (KDOT) Kansas Transportation Research and New-Developments (K-TRAN) Research Program funded this research project. It is an ongoing, cooperative and comprehensive research program addressing transportation needs of the state of Kansas utilizing academic and research resources from KDOT, Kansas State University and the University of Kansas. Transportation professionals in KDOT and the universities jointly develop the projects included in the research program.

NOTICE

The authors and the state of Kansas do not endorse products or manufacturers. Trade and manufacturers names appear herein solely because they are considered essential to the object of this report.

This information is available in alternative accessible formats. To obtain an alternative format, contact the Office of Public Affairs, Kansas Department of Transportation, 700 SW Harrison, 2nd Floor – West Wing, Topeka, Kansas 66603-3745 or phone (785) 296-3585 (Voice) (TDD).

DISCLAIMER

The contents of this report reflect the views of the authors who are responsible for the facts and accuracy of the data presented herein. The contents do not necessarily reflect the views or the policies of the state of Kansas. This report does not constitute a standard, specification or regulation.

Abstract

The importance of the analysis of circular columns to accurately predict their ultimate confined (steel and fiber-reinforced polymer [FRP]) capacity under shear-flexure-axial force interaction domain is recognized in light of the extreme load event imposed by the current *AASHTO LRFD Bridge Design Specifications*.

In this study, various procedures for computing the shear strength are reviewed. A formulation conforming to AASHTO (2014) *LRFD Bridge Design Specifications*, based on the Simplified Modified Compression Field Theory, is developed to predict the axial force-shear-moment interaction diagrams of circular confined concrete bridge pier sections reinforced with FRP. Comparisons with a large database of experiments indicate the accuracy of the resulting diagrams.

Transverse steel area, spacing, cross section diameter, and applied axial force are the main keys to analyze and increase the shear capacity of the cross section. Treating the cracked concrete as a new different material proved to be a beneficial approach to predict the sections' capacities and behaviors.

Using transverse reinforcement of FRP shows a significant improvement for axial force-bending moment and shear force capacities. The reader is also directed to use KDOT Column Expert for more accurate prediction of the interaction diagrams.

Acknowledgements

This research was made possible through funding from the Kansas Department of Transportation (KDOT) through its Kansas Transportation Research and New-Developments (K-TRAN) Program. Special thanks are extended to John Jones and Mark Hoppe of the KDOT Bureau of Structures and Geotechnical Services, for their interest in this project and their continuous support and feedback that made it possible to arrive at such important findings.

Table of Contents

Abstract v
Acknowledgements vi
Table of Contents vii
List of Tables ix
List of Figures x
Chapter 1: Introduction 1
1.1 Overview 1
1.2 Objectives 1
1.3 Scope 1
Chapter 2: Literature Review 3
2.1 Overview 3
2.2 Theoretical Treatments 3
2.2.1 ACI Committee 318 (2011) 3
2.2.2 Modified Compression Field Theory 5
Chapter 3: Present Formulation 17
3.1 Overview 17
3.2 AASHTO LRFD and NCHRP Report 678 Approach 17
3.2.1 Minimum Transverse Steel 17
3.2.2 Shear Resistance 18
3.2.3 Determination of β and θ 19
3.2.4 Calculation of Longitudinal Axial Strain (εs) 20
3.2.5 Angle of Inclination of Transverse Reinforcement to Longitudinal Axis (α) Calculations 23
3.2.6 Effective Number of Legs of Transverse Steel in Shear Resistance Calculations 24
3.2.7 FRP Shear Strength Contribution 26
Chapter 4: Implementation 29
4.1 Overview 29
4.2 Input Parameters 29
4.3 Effective Shear Area 30
4.3.1 Effective Shear Depth Calculation (d_v) 30

4.4 Analysis Procedure 31
4.4.1 Limits of Constraints 34
Chapter 5: Experimental Verification 37
5.1 Overview 37
5.2 Database Criteria 37
5.3 Comparisons Against Experimental Studies 37
5.3.1 Kawashima, Hosotani, and Yoneda (2000) 41
5.3.2 Liu and Sheikh (2013) 49
5.3.3 Siddiqui, Alsayed, Al-Salloum, Iqbal, and Abbas (2014) 57
5.4 Parametric Study 60
Chapter 6: Software Development 70
6.1 Introduction 70
6.2 Input Interface 70
6.3 Output Interface 72
Chapter 7: Conclusions 77
References 78

List of Tables

Table 2.1: Modified Compression Field Theory Experimental Program 15
Table 5.1: Experimental Data Geometrical and Material Properties 38
Table 5.2: Experimental Data FRP Properties 39
Table 5.3: Experimental Data Loading Properties 40
Table 5.4: Parametric Study FRP Properties 61

List of Figures

Figure 2.1: Ratio of Experimental to Predicted Shear Strength of Different Models 6
Figure 2.2: Loading and Deformation for MCFT Membrane Element 7
Figure 2.3: Mohr's Circle of Strains 8
Figure 2.4: Steel Bilinear Relationship 9
Figure 2.5: Relationship Between Hognestad's Equation and MCFT Suggested Equation for the Principal Compressive Stress 11
Figure 2.6: State of Equilibrium for Plane (a-a) and Plane (b-b) 13
Figure 2.7: Aggregate Interlock 14
Figure 2.8: Modified Compression Field Theory Specimen Loading Installation 16
Figure 3.1: Illustration of b_v and d_v Parameters 19
Figure 3.2: Illustration of Angle (θ) and Angle (α) 19
Figure 3.3: Strain Superimposition due to Moment, Shear, and Axial Force 22
Figure 3.4: Helix/Spiral 3D Plot 24
Figure 3.5: Shear Carried by Transverse Steel in Circular Column 25
Figure 4.1: Moment-Shear Interaction Diagram Under a Constant Axial Compression Force 32
Figure 4.2: Flow Chart of Present Procedure (Case 1: Sections with More than Minimum Transverse Steel) 33
Figure 4.3: Derivation of the Yielding Stress Limit 35
Figure 4.4: Yielding Zone for Different Yielding Strength 36
Figure 5.1: Kawashima et al. (2000) Cross Section 41
Figure 5.2: Kawashima et al. (2000) Control Interaction Diagram (Group 1) 41
Figure 5.3: Kawashima et al. (2000) Cross Section 42
Figure 5.4: Kawashima et al. (2000) Interaction Diagram (One Layer of FRP) 43
Figure 5.5: Kawashima et al. (2000) Cross Section 43
Figure 5.6: Kawashima et al. (2000) Interaction Diagram (Two Layers of FRP) 44
Figure 5.7: Kawashima et al. (2000) Cross Section 45
Figure 5.8: Kawashima et al. (2000) Control Interaction Diagram (Group 2) 45
Figure 5.9: Kawashima et al. (2000) Cross Section 46
Figure 5.10: Kawashima et al. (2000) Interaction Diagram (One Layer of FRP) 47

Figure 5.11: Kawashima et al. (2000) Cross Section 47
Figure 5.12: Kawashima et al. (2000) Interaction Diagram (Two Layers of FRP) 48
Figure 5.13: Liu and Sheikh (2013) Cross Section 49
Figure 5.14: Liu and Sheikh (2013) Interaction Diagram (P=290 kips; One Layer of CFRP) ... 49
Figure 5.15: Liu and Sheikh (2013) Cross Section 50
Figure 5.16: Liu and Sheikh (2013) Interaction Diagram (P=290 kips; One Layer of GFRP) ... 50
Figure 5.17: Liu and Sheikh (2013) Cross Section 51
Figure 5.18: Liu and Sheikh (2013) Interaction Diagram (P=430 kips; One Layer of CFRP) ... 52
Figure 5.19: Liu and Sheikh (2013) Cross Section 52
Figure 5.20: Liu and Sheikh (2013) Interaction Diagram (P=430 kips; One Layer of GFRP) ... 53
Figure 5.21: Liu and Sheikh (2013) Cross Section 54
Figure 5.22: Liu and Sheikh (2013) Interaction Diagram (P=602 kips; Control Column) 54
Figure 5.23: Liu and Sheikh (2013) Cross Section 55
Figure 5.24: Liu and Sheikh (2013) Interaction Diagram (P=602 kips; Two Layers of CFRP).... 55
Figure 5.25: Liu and Sheikh (2013) Cross Section 56
Figure 5.26: Liu and Sheikh (2013) Interaction Diagram (P=602 kips; Three Layers of CFRP).. 56
Figure 5.27: Siddiqui et al. (2014) Cross Section 57
Figure 5.28: Siddiqui et al. (2014) Interaction Diagram (P=112.5 kips; One Layer of CFRP) 58
Figure 5.29: Siddiqui et al. (2014) Cross Section 58
Figure 5.30: Siddiqui et al. (2014) Interaction Diagram (P=78.75 kips; One Layer of CFRP) 59
Figure 5.31: Siddiqui et al. (2014) Cross Section 59
Figure 5.32: Siddiqui et al. (2014) Interaction Diagram (P=72 kips; One Layer of CFRP)..... 60
Figure 5.33: Shear Force-Bending Moment Interaction Diagram (Steel Ratio=0.01; One Layer of GFRP; Different Cross-Sectional Diameter) 61
Figure 5.34: Shear Force-Bending Moment Interaction Diagram (Steel Ratio=0.0125; One Layer of GFRP; Different Cross-Sectional Diameter) 62
Figure 5.35: Shear Force-Bending Moment Interaction Diagram (Steel Ratio=0.01; One Layer of CFRP; Different Cross-Sectional Diameter) 62
Figure 5.36: Shear Force-Bending Moment Interaction Diagram (Steel Ratio=0.0125; One Layer of CFRP; Different Cross-Sectional Diameter) 63

Figure 5.37: Shear Force-Bending Moment Interaction Diagram (Diameter=28 in.; One Layer of GFRP; Different Steel Ratios) 63
Figure 5.38: Shear Force-Bending Moment Interaction Diagram (Diameter=36 in.; One Layer of CFRP; Different Steel Ratios) 64
Figure 5.39: Shear Force-Bending Moment Interaction Diagram (Diameter=28 in.; One Layer of GFRP; Different Transverse Steel Spacing) 64
Figure 5.40: Shear Force-Bending Moment Interaction Diagram (Diameter=36 in.; One Layer of GFRP; Different Transverse Steel Spacing) 65
Figure 5.41: Shear Force-Bending Moment Interaction Diagram (Diameter=28 in.; One Layer of CFRP; Different Transverse Steel Spacing) 65
Figure 5.42: Shear Force-Bending Moment Interaction Diagram (Diameter=36 in.; One Layer of CFRP; Different Transverse Steel Spacing) 66
Figure 5.43: Shear Force-Bending Moment Interaction Diagram (Diameter=28 in.; Two Layers of GFRP; Different f'_c Values) 66
Figure 5.44: Shear Force-Bending Moment Interaction Diagram (Diameter=36 in.; Two Layers of GFRP; Different f'_c Values) 67
Figure 5.45: Shear Force-Bending Moment Interaction Diagram (Diameter=28 in.; Two Layers of CFRP; Different f'_c Values) 67
Figure 5.46: Shear Force-Bending Moment Interaction Diagram (Diameter=36 in.; Two Layers of CFRP; Different f'_c Values) 68
Figure 5.47: Shear Force-Bending Moment Interaction Diagram (Diameter=28 in.; Different Number of Plies) 69
Figure 5.48: Shear Force-Bending Moment Interaction Diagram (Diameter=36 in.; Different Number of Plies) 69
Figure 6.1: KDOT Column Expert Input Interface 71
Figure 6.2: KDOT Column Expert Custom Bars Input 71
Figure 6.3: KDOT Column Expert FRP Parameters Input Window 72
Figure 6.4: KDOT Column Expert Axial Force Input 73
Figure 6.5: KDOT Column Expert FRP Scheme Input Window 73
Figure 6.6: KDOT Column Expert 2D Moment-Shear Interaction Diagram 74
Figure 6.7: KDOT Column Expert 3D Domain 74

Figure 6.8: Minimum Transverse Steel 75
Figure 6.9: Maximum Aggregate Size Input 75
Figure 6.10: Maximum Spacing Error Message 75
Figure 6.11: Lack of Longitudinal Steel Error 76
Figure 6.12: Transverse Steel Exceeded 100 ksi Error 76

This page intentionally left blank.

Chapter 1: Introduction

1.1 Overview

Even though the behavior of concrete elements subjected to shear has been studied for many years, researchers do not have a full agreement on concrete shear resistance. This is mainly because of the many different mechanisms that affect the shear transfer process of concrete, such as aggregate interlock, interface shear transfer across cracks, shear transfer in compression zone, dowel action, and residual tensile stresses normal to cracks. The complexity of the shear understanding increases by introducing fiber-reinforced polymer (FRP) transverse reinforcement to the section. However, researchers agree that aggregate interlock and shear transfer in compression zone are the key components to understanding concrete behavior under full-field shear, flexural, and axial stresses.

1.2 Objectives

The importance of the analysis of circular reinforced concrete columns to accurately predict their confined load carrying capacity under full interaction domain (moment-shear force-axial force) is recognized in light of the extreme load event imposed by the current AASHTO (2014) *LRFD Bridge Design Specifications* based on the Simplified Modified Compression Field Theory (SMCFT). Since these provisions are relatively new to the specification, a detailed evaluation of their predictions is warranted. Objective judgment may be reached if the generated interaction diagrams are compared to experimental results available in the literature.

1.3 Scope

This report is composed of seven chapters covering the development of calculations, analysis procedures, benchmarking, and practical applications.

Chapter 1 introduces the work, highlighting the objectives and scope of the report. Chapter 2 details the literature review as it relates to the shear models and the experimental studies addressing the behavior of circular reinforced-concrete columns under different load combinations. Chapter 3 describes the present formulation used in the analysis procedure to predict the full domain of columns sections. Chapter 4 discusses the implementation procedure to utilize

the formulated equations and limits to generate interaction diagrams that represent the extreme load event of the sections. Chapter 5 provides the final results and comparisons of this study with brief discussions and comments. Chapter 6 briefs the reader on the software development that was coded using the proposed procedure and describes the program interface design and features. Chapter 7 discusses the conclusions and provides recommendations for future relevant work.

Chapter 2: Literature Review

2.1 Overview

This section provides a general review of shear strength provisions implemented by various design codes. Most design codes are based on concrete strength and transverse reinforcement strength and FRP confinement strength to determine the shear capacity of reinforced concrete sections. These three components are simply added together to provide the full shear capacity of the section in the presence of flexure and axial force.

2.2 Theoretical Treatments

2.2.1 ACI Committee 318 (2011)

The ultimate shear strength, including FRP effect, could be obtained by adding the FRP contribution to that of concrete and transverse steel.

$$V_u = V_c + V_s + \Psi_f V_f \qquad \textbf{Equation 2.1}$$

Where:

V_c is the concrete shear capacity, calculated based on ACI 318 (2011), and

V_s is the transverse steel shear capacity calculated based on ACI 318 (2011).

$$V_c = 0.002\left(1 + \frac{P}{2000A_g}\right)\lambda\sqrt{f_c'}bd \ \text{(ksi)} \qquad \textbf{Equation 2.2}$$

$$V_s = \frac{A_v f_{y_t}(\sin\alpha + \cos\alpha)d_s}{s} \qquad \textbf{Equation 2.3}$$

Where: (P) is axial load subjected to the section, (A_g) is gross cross-sectional area, (f'_c) is concrete compressive strength, (b) is the width of section, (d) is the effective depth of section, (A_v) is the area of transverse reinforcement within the spacing (s), (f_{yt}) is the yield stress of transverse steel, (α) is the angle between inclined stirrups and longitudinal axis of the member, and (λ) is a modification factor to account for lightweight concrete.

The value of Ψf is taken as 0.85 for U-wraps and side bonding, and is taken as 0.95 for fully wrapped sections. V_f is the FRP shear capacity and it is calculated similar to transverse steel.

$$V_f = \frac{A_{fv} f_{fe} (\sin\alpha + \cos\alpha) d_{fv}}{s_f}$$ **Equation 2.4**

Where:

$$A_{fv} = 2nt_f w_f$$ **Equation 2.5**

$$f_{fe} = E_f \varepsilon_{fe}$$ **Equation 2.6**

Where: ε_{fe} is the effective tensile strain developed in the FRP shear reinforcement, E_f is the modulus of elasticity of FRP sheets, n is the number of layers, t_f is the thickness of the layer, w_f is the width of the layer, S_f is the spacing of the transverse layers, and d_{fv} is the effective depth of FRP shear reinforcement.

The effective tensile strain developed in the FRP shear reinforcement ε_{fe} is determined based on the wrapping schemes.

- Fully wrapped sections: ε_{fe} is limited to 0.004 due to the early loss of aggregate interlock before reaching the ultimate FRP strain ε_{fu}.

  $$\varepsilon_{fe} = 0.004 \leq 0.75\varepsilon_{fu}$$ **Equation 2.7**

- U-wraps or two sides plies: due to common debonding using these schemes before the loss of aggregate interlock, bond stress is the key to determine the effective strain that could be attained.

  $$\varepsilon_{fe} = k_v \varepsilon_{fu} \leq 0.004$$ **Equation 2.8**

The bond reduction coefficient (k_v) is a function of concrete strength, FRP modulus of elasticity, and geometry of the FRP confinement.

$$k_v = \frac{k_1 k_2 L_e}{468\varepsilon_{fu}} \leq 0.75 \; (U.S.\, customary\ units)$$ **Equation 2.9**

Where:

$$k_1 = \left(\frac{f'_c}{4000}\right)^{\frac{2}{3}} \; (U.S.\, customary\ units)$$ **Equation 2.10**

$$k_2 = \frac{d_{fv} - L_e}{d_{fv}} \;\; for\ U-wraps \;\; and \; k_2 = \frac{d_{fv} - 2L_e}{d_{fv}} \; for\ two\ bonded\ sides$$ **Equation 2.11**

Where: L_e is the active bond length, over which the majority of the bond stress is maintained.

$$L_e = \frac{2500}{(nt_f E_f)^{0.58}} \ (U.S. customary\ units) \qquad \textbf{Equation 2.12}$$

The shear force provided by transverse steel reinforcement and transverse FRP reinforcement is limited according to ACI Committee 318 (2011) to avoid concrete struts crushing.

$$V_s + V_f \leq 8\sqrt{f_c'} b_w d \quad (U.S\ customary\ units) \qquad \textbf{Equation 2.13}$$

2.2.2 Modified Compression Field Theory

In the 1980s, after testing different reinforced concrete members elements subjected to pure shear, pure axial load, and a combination of shear and axial load, a theory called the Modified Compression Field Theory (MCFT) was developed based on the Compression Field Theory (Vecchio & Collins, 1986). The MCFT was able to accurately predict the shear behavior of concrete members subjected to shear and axial forces. The main key of this theory is that significant tensile stresses could exist in the concrete between the cracks even at very high values of average tensile strains. In addition, the value for angle θ of diagonal compressive stresses was considered as variable compared to the fixed value of 45 assumed by ACI (2011) Code.

To simplify the process of predicting the shear strength of a section using the MCFT, the shear stress is assumed to remain constant over the depth of the cross-section and the shear strength of the section can be determined by considering the axial stress and the shear stress at one location in the web. This was the basis of the sectional design model for shear implemented by the *AASHTO LRFD Bridge Design Specifications* based on the work of Bentz, Vecchio, and Collins (2006).

Even though the AASHTO LRFD procedure to predict the shear strength of a section was straight forward in earlier versions of the specification, the contribution of concrete to shear strength of a section is a function of β and varying angle θ, for which values were determined using the tables provided by AASHTO. The factor β indicates the ability of diagonally cracked concrete to transmit tension and shear. The Modified Compression Field Theory was furthermore simplified when simple and direct equations were developed by Bentz et al. (2006) for β and θ to replace the iterative procedure using the tables that was implemented by earlier versions of AASHTO. These

simplified equations were then used to predict the shear strength of different reinforced concrete sections and the results were compared to those obtained from MCFT, as shown in Figure 2.1.

Consequently, the shear strength predicted by the Simplified Modified Compression Field Theory (SMCFT) and Modified Compression Field Theory (MCFT) were compared with experimental results of various beams. It was found that the results of the SMCFT and the MCFT were almost exactly similar and both matched properly the experimental results. In addition, the results were also compared with the ACI (2011) Code where it was pretty much inconsistent in particular for panels with no transverse reinforcements (Bentz et al., 2006; see Figure 2.1).

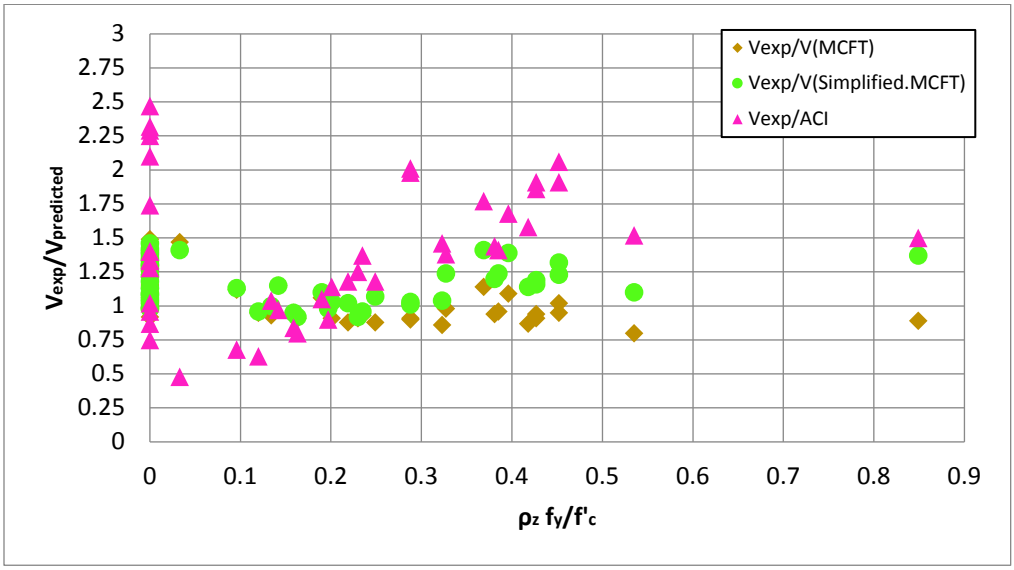

Figure 2.1: Ratio of Experimental to Predicted Shear Strength of Different Models
Graph is reproduced from data collected by Bentz et al. (2006)

Before discussing the Modified Compression Field Theory, it is important to define the basic membrane element used to develop the approach. The reinforced concrete element is defined to have a uniform thickness and a relatively small size. It consists of an orthogonal grid of reinforcement with the longitudinal steel in (X) direction and the transverse steel in (Y) direction (see Figure 2.2).

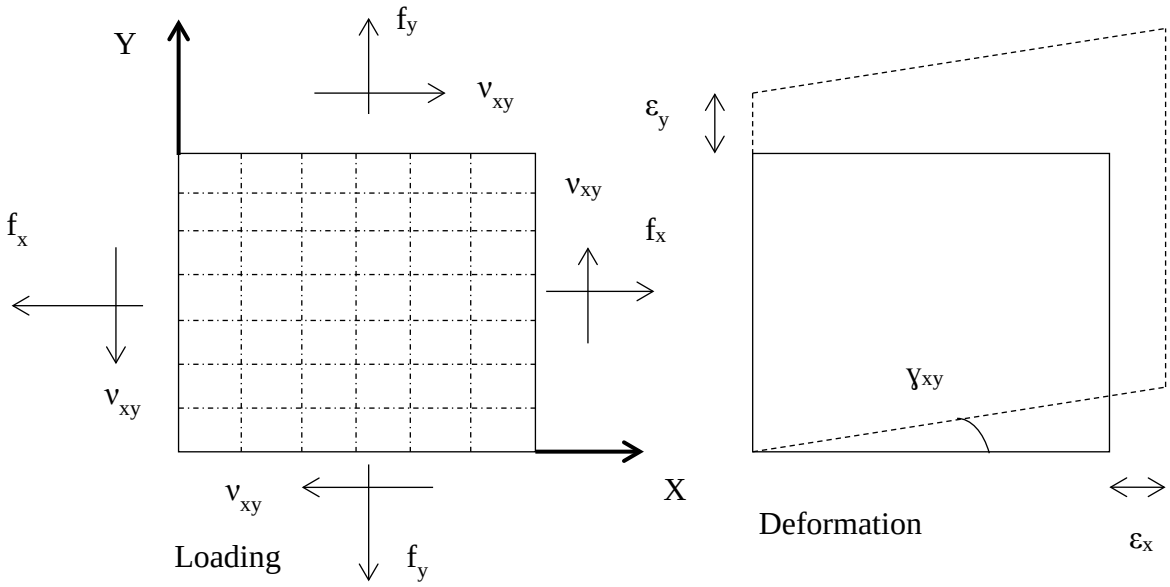

Figure 2.2: Loading and Deformation for MCFT Membrane Element

Uniform axial stresses (fx), (fy) and a uniform shear stress (vxy) are acting on the element causing two normal strains (εx) and (εy) in addition to a shear strain (ɣxy; see Figure 2.2). The main target is to develop a relationship between the stresses and the strains in the member. In order to achieve this relationship, some reasonable assumptions were made:

1. Each strain state is corresponding to one stress state.
2. Stresses and strains could be calculated in terms of average values when taken over areas large enough to include several cracks.
3. A perfect bond exists between the steel and the concrete.
4. A uniform longitudinal and transverse steel distribution over the element.

2.2.2.1 Compatibility Conditions

Assuming a perfect bond between the concrete and the reinforcement requires that any change in concrete strain will cause an equal change in steel strain in the same direction.

$$\varepsilon_c = \varepsilon_s = \varepsilon$$ **Equation 2.14**

By knowing the three strains ε_x, ε_y, and γ_{xy}, the strain in any other direction can be calculated from the geometry of Mohr's circle of strain (see Figure 2.3).

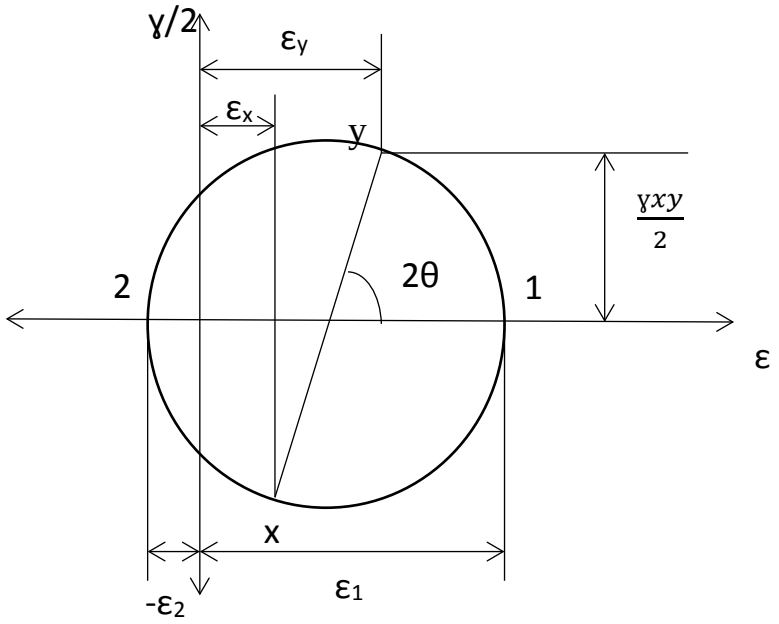

Figure 2.3: Mohr's Circle of Strains

In Figure 2.3, (ε_1) represents the principal tensile strain, while (ε_2) represents the principal compressive strain. (θ) is the angle of the principal direction with respect to the horizontal direction.

2.2.2.2 Equilibrium Conditions

In order to achieve equilibrium, the summation of the applied forces and the resisting forces generated in the element should equal zero in each direction. In (x) direction (Figure 2.2), the state of equilibrium is:

$$\int f_x \, dA = \int f_{cx} dA_c + \int f_{sx} dA_s \qquad \textbf{Equation 2.15}$$

Where:

(f_{cx}) and (A_c) are the stress in concrete and area of concrete, and

(f_{sx}) and (A_s) are the stress in steel and area of steel.

Ignoring the reduction in concrete area due to the steel exists:

$$f_x = f_{cx} + \rho_s f_{sx} \qquad \textbf{Equation 2.16}$$

Similarly,

$$f_y = f_{cy} + \rho_s f_{sy}$$ **Equation 2.17**

$$\nu_{xy} = \nu_{cx} + \rho_s \nu_{sx}$$ **Equation 2.18**

$$\nu_{xy} = \nu_{cy} + \rho_s \nu_{sy}$$ **Equation 2.19**

2.2.2.3 Stress-Strain Relationship

The stress-strain relationships for the concrete and the reinforcement are assumed to be completely independent of each other. The axial stress in steel would be only a result of the axial strain in the steel. Also, shear stresses in the steel on a plane perpendicular to the steel longitudinal axis are assumed to be zero. Regarding the steel axial stress-axial strain relationship, the usual bilinear relationship is assumed (see Figure 2.4).

$$f_s = E_s \varepsilon_s \leq f_y$$ **Equation 2.20**

$$\nu_s = 0$$ **Equation 2.21**

Where:

(E_s) is the modulus of elasticity of steel, and

(f_y) is the yielding stress in steel.

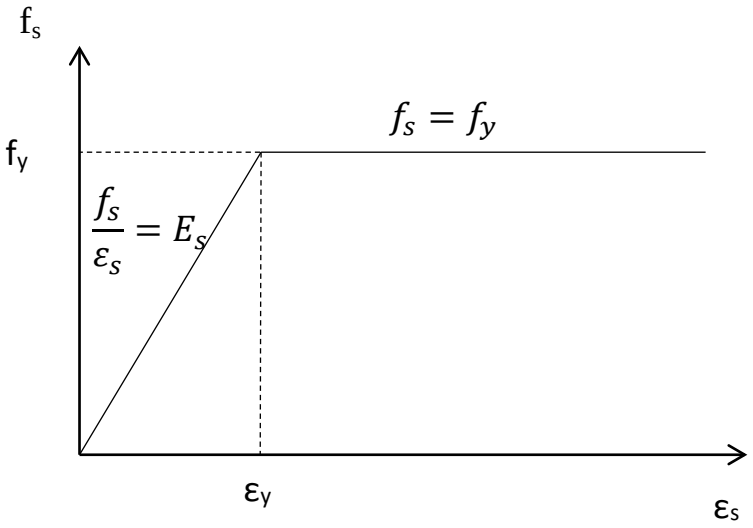

Figure 2.4: Steel Bilinear Relationship

In regard to the concrete stress-strain relationships, 30 reinforced concrete elements were tested under different loading conditions including pure shear, uniaxial compression, biaxial compression, and combined shear and axial load. Longitudinal and transverse steel ratios and concrete strength were also variables in these tests. More details are discussed in this literature review under the experimental works section.

It was assumed that the principal strain direction in concrete (θ) and the principal stress direction in concrete (θ_c) have the same angle $\theta_c = \theta$. However, it was observed that the direction of the principal strain in the concrete deviated from the direction of the principal stress in concrete $\theta_c = \theta \pm 10$ (Vecchio & Collins, 1986).

The principal compressive stress in the concrete (f_{c2}) was found to be a function in both the principal compressive strain (ε_2) and the accompanied principal tensile strain (ε_1); for this reason, the cracked concrete under tensile strains normal to the compression is weaker than concrete standard cylinder test. The suggested relationship is:

$$f_{c2} = f_{c2\max}\left(\frac{2\varepsilon_2}{\varepsilon_c'} - \left(\frac{\varepsilon_2}{\varepsilon_c'}\right)^2\right) \qquad \textbf{Equation 2.22}$$

Where: (ε'_c) is the strain corresponding to the (f_{c2max}).

It is a good observation to mention that the suggested equation is similar in behavior to Hognestad's concrete parabola; they only differ in the maximum values (see Figure 2.5).

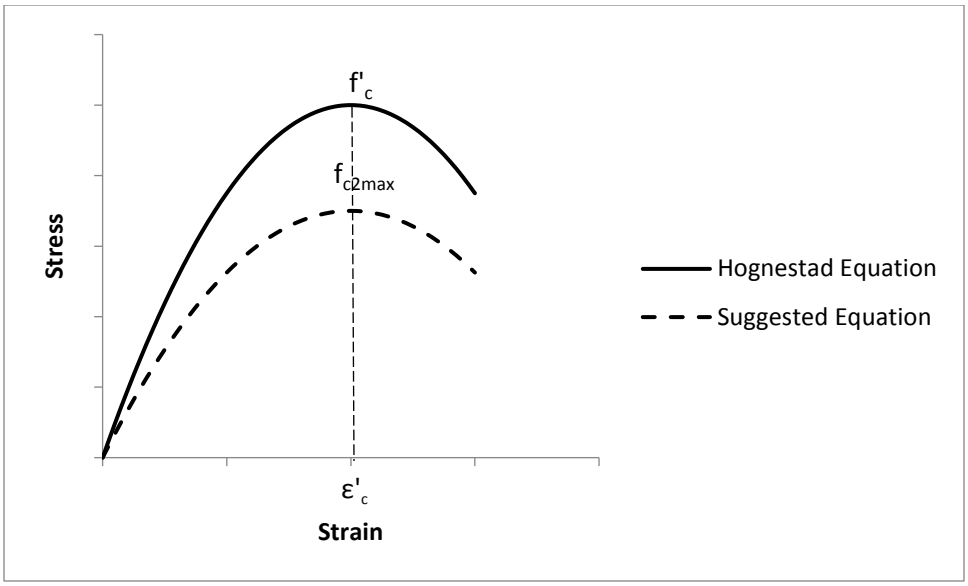

Figure 2.5: Relationship Between Hognestad's Equation and MCFT Suggested Equation for the Principal Compressive Stress

In tension, it was suggested to use the linear stress-strain relationship to define the relationship between the principal tensile stress and the principal tensile strain in concrete prior to cracking.

$$f_{c1} = E_c \varepsilon_1 \qquad \textbf{Equation 2.23}$$

Where: (E_c) is the modulus of elasticity of concrete.

After cracking, the suggested equation is:

$$f_{c1} = \frac{f_{cr}}{1+\sqrt{200\varepsilon_1}} \qquad \textbf{Equation 2.24}$$

Where: (f_{cr}) is the concrete rupture stress.

2.2.2.4 Average Stresses and Average Strains Concept

The Modified Compression Field Theory considers average stresses and average strain across the crack. It does not provide an approach corresponding to local stress/strain variations. The concrete tensile stresses would be minimum value at cracks, and it would reach a value higher than the average in the distance between the two successive cracks. The steel tensile stresses would

be higher than the average at cracks, and it would have a lower value between the cracks due to the contribution of concrete tensile resistance.

2.2.2.5 Transmitting Shear/Tension Across Cracks

The applied stresses (f_x), (f_y), and (ν_{xy}) and the internal stresses should establish a state of equilibrium in the element. Furthermore, the internal stress at a crack plane (plane a-a) should equal the stresses at a parallel plane in the distance between two successive cracks (plane b-b; see Figure 2.6). The internal stresses at the crack are steel stresses (f_{scr}), shear stresses (ν_c), and minor compressive stresses (f_c). The internal stresses at the un-cracked plane parallel to the crack plane are average stresses (f_{c1}) and steel stresses (f_s). In terms of average strain, the average shear stress is zero at plane b-b. By assuming a unit cross area along the crack, the stresses equilibrium in (x) and (y) directions is calculated.

At (x) direction:

$$\rho_s f_s \sin(\theta) + f_{c1} \sin(\theta) = \rho_s f_{scr} \sin(\theta) - f_c \sin(\theta) - \nu_c \cos(\theta) \qquad \textbf{Equation 2.25}$$

At (y) direction:

$$\rho_s f_s \cos(\theta) + f_{c1} \cos(\theta) = \rho_s f_{scr} \cos(\theta) - f_c \cos(\theta) + \nu_c \sin(\theta) \qquad \textbf{Equation 2.26}$$

From Equations 2.25 and 2.26, an equilibrium can't be achieved without the shear stresses especially when the reinforcement at cracking (f_{scr}) is approaching the yielding, as the concrete contribution will then be negligible.

The shear stresses are caused due to the aggregate interlock (see Figure 2.7). Due to the high strength of the aggregate, the concrete crack occurs along the interface of the aggregate. The shear stress across the crack (ν_c) is function in maximum aggregate size (a), crack width (w), and the compressive stress on the crack (f_c; Walraven, 1981).

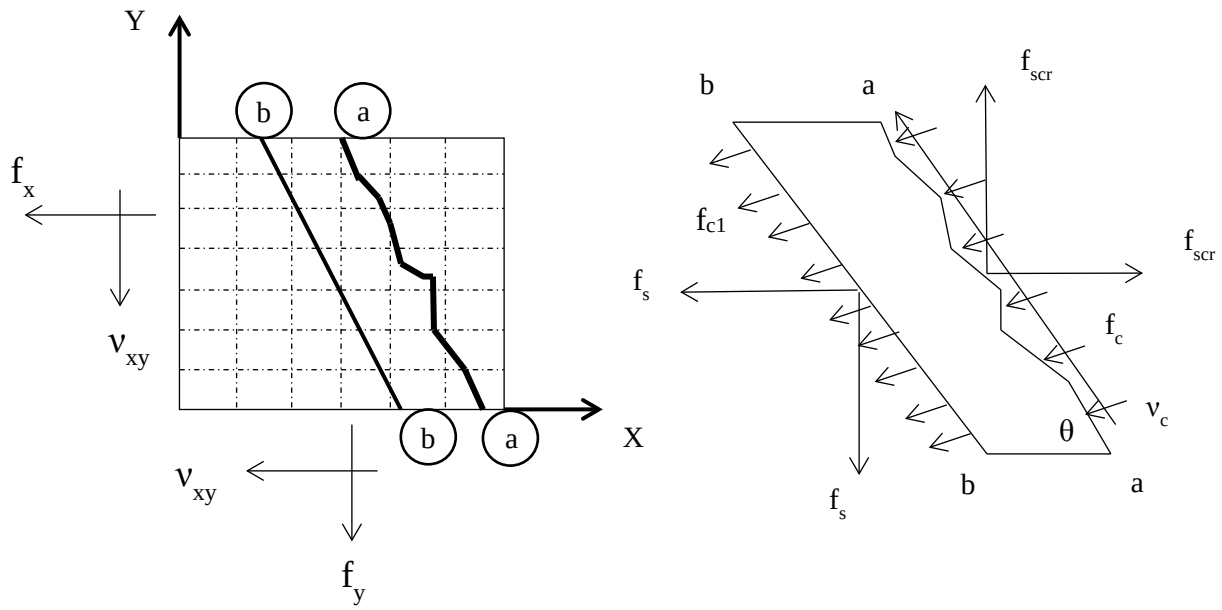

Figure 2.6: State of Equilibrium for Plane (a-a) and Plane (b-b)

Walraven (1981) suggested the following equation based on experimental results.

$$v_c = 0.18v_{cmax} + 1.64f_c - \frac{0.82f_c^2}{v_{cmax}} \qquad \textbf{Equation 2.27}$$

Where:

$$v_{cmax} = \frac{12\sqrt{-f_c'}}{0.31+24\frac{w}{a+0.63}} \ldots \qquad \textbf{Equation 2.28}$$

Where:

(a) is the maximum aggregate size in inches,

(w) is the crack width in inches, and

(f'_c) is the concrete maximum compressive strength in psi.

In Equation 2.28, (f'_c) should be substituted with a negative value as a representation of compression.

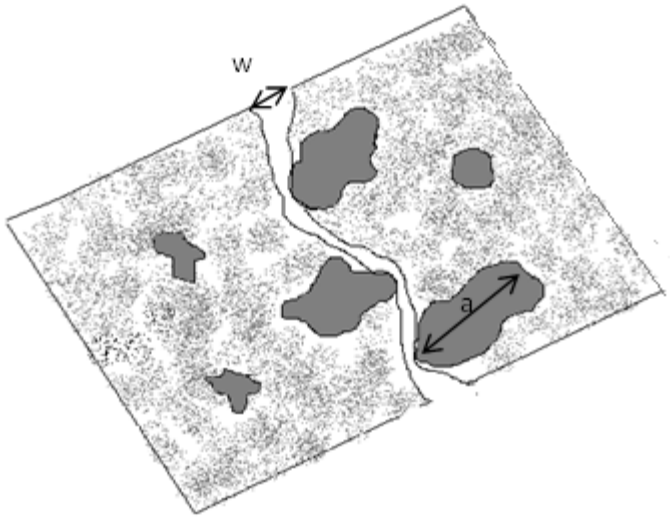

Figure 2.7: Aggregate Interlock

Vecchio and Collins (1986) proposed the Modified Compression Field Theory that deals with the reinforced cracked concrete as a new composite material as described in the theoretical approaches presented in this literature review. In order to justify their approach, 30 reinforced concrete elements were subjected to different load combinations. Two-thirds of the elements were subjected to pure shear, and one-third of the elements were subjected to a combination of shear and axial compression/tension force. Longitudinal steel, transverse steel, and concrete strength were also variables in this experimental program. Table 2.1 shows the loading conditions and also shows the longitudinal and transverse steel ratio and concrete strength for each element. The test specimens were a thin square prism (35 in. × 35 in. × 2.75 in.). They were reinforced with two layers of welded wire mesh with the wires parallel to the square edge. A 0.25-in. clear cover was provided from the longitudinal steel to the element surface. The loads were applied using hydraulic jacks on five steel shear keys pre-casted into each of the four edges (see Figure 2.8). The direct output of these experiments was to determine the average strains and average stresses in the reinforcement. By knowing the external applied forces, the cracked concrete contribution could be calculated. In Table 2.1, compression is represented by negative sign and tension is represented by positive sign. (ρl) and (ρs) are longitudinal steel ratio and transverse steel ratio, respectively.

Table 2.1: Modified Compression Field Theory Experimental Program

Panel	Loading ratio v-f_x-f_y	ρl	f_y (ksi)	ρs	f_{yt} (ksi)	f'$_c$ (ksi)	v_u (ksi) (failure)
PV1	1:00:00	0.0179	70.035	0.0168	70.035	-5.0025	1.1629
PV2	1:00:00	0.0018	62.06	0.0018	62.06	-3.4075	0.1682
PV3	1:00:00	0.0048	95.99	0.0048	95.99	-3.857	0.44515
PV4	1:00:00	0.0106	35.09	0.0106	35.09	-3.857	0.41905
PV5	1:00:00	0.0074	90.045	0.0074	90.045	-4.1035	0.6148
PV6	1:00:00	0.0179	38.57	0.0179	38.57	-4.321	0.65975
PV7	1:00:00	0.0179	65.685	0.0179	65.685	-4.495	0.98745
PV8	1:00:00	0.0262	66.99	0.0262	66.99	-4.321	0.96715
PV9	1:00:00	0.0179	65.975	0.0179	65.975	-1.682	0.5423
PV10	1:00:00	0.0179	40.02	0.01	40.02	-2.1025	0.57565
PV11	1:00:00	0.0179	34.075	0.0131	34.075	-2.262	0.5162
PV12	1:00:00	0.0179	68.005	0.0045	68.005	-2.32	0.45385
PV13	1:00:00	0.0179	35.96	0	0	-2.639	0.29145
PV14	1:00:00	0.0179	65.975	0.0179	65.975	-2.958	0.7598
PV15	00:-1:00	0.0074	36.975	0.0074	36.975	-3.1465	-2.842
PV16	1:00:00	0.0074	36.975	0.0074	36.975	-3.1465	0.3103
PV17	00:-1:00	0.0074	36.975	0.0074	36.975	-2.697	-3.0885
PV18	1:00:00	0.0179	62.495	0.0032	59.74	-2.8275	0.4408
PV19	1:00:00	0.0179	66.41	0.0071	43.355	-2.755	0.57275
PV20	1:00:00	0.0179	66.7	0.0089	43.065	-2.842	0.6177
PV21	1:00:00	0.0179	66.41	0.013	43.79	-2.8275	0.72935
PV22	1:00:00	0.0179	66.41	0.0152	60.9	-2.842	0.88015
PV23	1:-0.39:-0.39	0.0179	75.11	0.0179	75.11	-2.9725	1.28615
PV24	1:-0.83:-0.83	0.0179	71.34	0.0179	71.34	-3.451	1.1513
PV25	1:-0.69:-0.69	0.0179	67.57	0.0179	67.57	-2.784	1.3224
PV26	1:00:00	0.0179	66.12	0.0101	67.135	-3.0885	0.78445
PV27	1:00:00	0.0179	64.09	0.0179	64.09	-2.9725	0.92075
PV28	1:0.32:0.32	0.0179	70.035	0.0179	70.035	-2.755	0.841
PV29	Changing	0.0179	63.945	0.0089	46.98	-3.1465	0.85115
PV30	1:00:00	0.0179	63.365	0.0101	68.44	-2.7695	0.74385

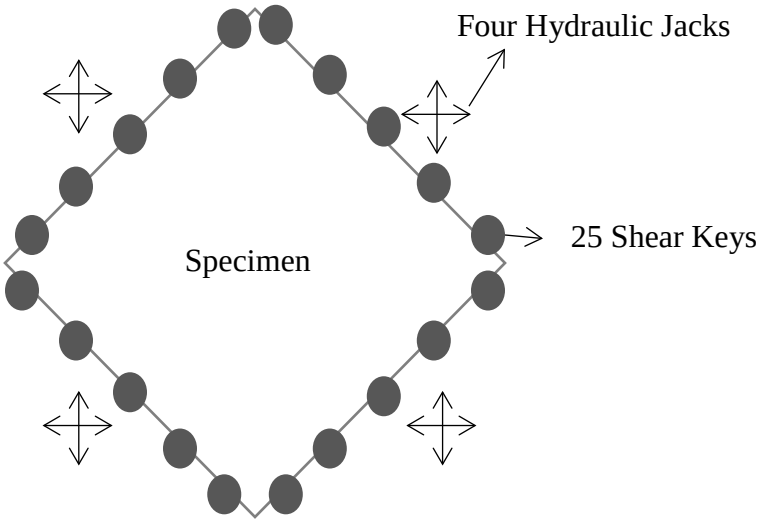

Figure 2.8: Modified Compression Field Theory Specimen Loading Installation

Chapter 3: Present Formulation

3.1 Overview

This section provides the proposed approaches to generate the interaction domain (moment-shear force-axial force) for non-prestressed reinforced concrete columns. The first approach is based on the Simplified Modified Compression Field Theory, AASHTO (2014) *LRFD Bridge Design Specifications,* and NCHRP Report 678 (Belarbi et al., 2011) to account for FRP reinforcement.

3.2 AASHTO LRFD and NCHRP Report 678 Approach

The present procedure is based on the Simplified Modified Compression Field Theory (SMCFT) originally developed by Bentz et al. (2006) and adopted by AASHTO (2014) *LRFD Bridge Design Specifications* and NCHRP Report 678 by Belarbi et al. (2011). This theory was derived based on the MCFT developed earlier by Vecchio and Collins (1986). In this section, shear equations used in this study are presented and specialized for the present application of non-prestressed circular reinforced concrete columns.

3.2.1 Minimum Transverse Steel

The following empirical equation is adopted to signify the minimum transverse reinforcement allowed by AASHTO (2014):

$$A_v \geq .0316\sqrt{f_c'}\frac{b_v s}{f_y} \quad (A_v \geq .083\sqrt{f_c'}\frac{b_v s}{f_y}) \qquad \text{(AASHTO 5.8.2.5-1)} \qquad \textbf{Equation 3.1}$$

Where:

A_v = area of transverse reinforcement within spacing (s) in inches^2 (mm^2)

f'_c = concrete compressive capacity in ksi (MPa)

b_v = effective web width taken as the minimum web width, measured parallel to the neutral axis, between the tensile resultant and compressive force due to flexure, or for circular sections, it is taken as the diameter of the section in inches (mm); see Figure 3.1.

s = spacing of transverse reinforcement in inches (mm)

f_y = yield strength in transverse steel in ksi (MPa)

A minimum amount of transverse reinforcement is necessary to control the growth of shear diagonal cracking. Based on this equation, there are two cases of analysis as described below.

3.2.2 Shear Resistance

The section nominal shear capacity is determined as the summation of concrete shear contribution and transverse steel shear contribution. Concrete shear contribution is a function in the effective shear area (b_v*d_v), concrete strength, and (β), which indicates the ability of the diagonally cracked concrete to transmit shear along its axis. Transverse steel shear contribution depends on the transverse steel yielding strength, area of transverse steel, the angle of cracking (θ), and the angle of inclination of transverse reinforcement to the longitudinal axis (α).

$$V_n = V_c + V_s + V_f$$ (AASHTO 5.8.3.3-1) **Equation 3.2**

In which:

$$V_c = .0316\beta\sqrt{f_c'}b_v d_v \ \ (V_c = \beta\sqrt{f_c'}b_v d_v)$$ (AASHTO 5.8.3.3-3) **Equation 3.3**

$$V_s = \frac{\pi}{2}\frac{A_v f_y d_v (cot\theta + cot\alpha)sin\alpha}{s}$$ (AASHTO 5.8.3.3-4) **Equation 3.4**

$$V_f = \frac{A_f f_{fe} d_f (cot\theta + cot\alpha)sin\alpha}{s_f}$$ (NCHRP 678) **Equation 3.5**

Where:

V_c = concrete shear strength that relies on the tensile stresses in concrete in ksi (MPa)

V_s = steel shear strength that relies on the tensile stresses in transverse steel in ksi (MPa)

V_f = FRP shear strength that relies on the tensile stresses in transverse FRP in ksi

d_v = effective shear depth taken as the distance, measured perpendicular to the neutral axis, between the tensile resultant and compressive force due to flexure. It needs not be taken to be less than the greater of $0.9d_e$ or 0.72h in inches (mm); see Figure 3.1.

β = factor indicating ability of diagonally cracked concrete to transmit tension and shear

θ = angle of inclination of diagonal compressive stresses (˚)

α = angle of inclination of transverse reinforcement to longitudinal axis (˚); see Figure 3.2.

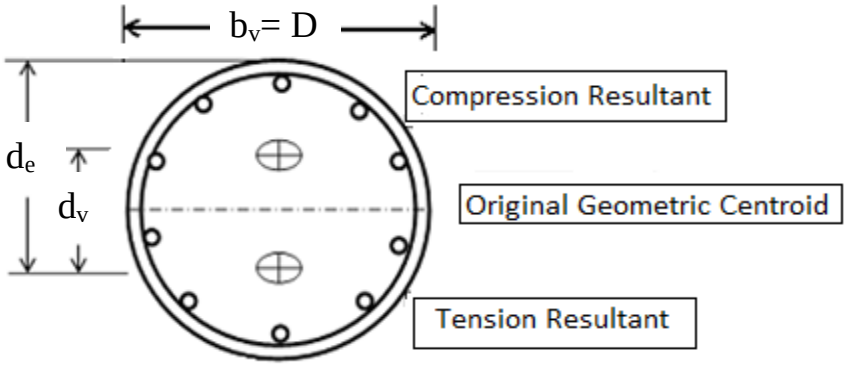

Figure 3.1: Illustration of b_v and d_v Parameters

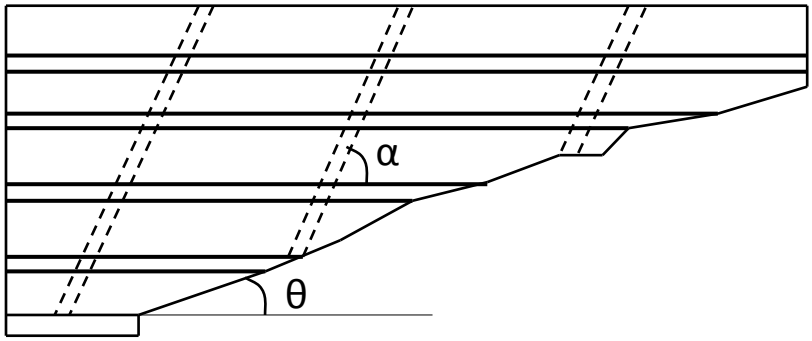

Figure 3.2: Illustration of Angle (θ) and Angle (α)

3.2.3 Determination of β and θ

In the case of more transverse steel than the minimum transverse steel required by AASHTO (2014) LRFD Specification (Equation 3.1), β and θ are calculated based on the longitudinal axial strain at the centroid of tensile steel (ε_s). This is identified as Case 1 in this study:

$$\beta = \frac{4.8}{1+750\varepsilon_s} \quad \left(\beta = \frac{0.4}{1+750\varepsilon_s}\right) \qquad \text{(AASHTO 5.8.3.4.2-1)} \qquad \textbf{Equation 3.6}$$

$$\theta = 29(degree) + 3500\varepsilon_s \leq 75^{\circ} \qquad \text{(AASHTO 5.8.3.4.2-3)} \qquad \textbf{Equation 3.7}$$

Note that Equation 3.6 is for the kip-in. units (SI units) system.

In the case of less transverse steel than the minimum transverse steel required by AASHTO (2014) LRFD Specification (Equation 3.1), β and θ are calculated based on the longitudinal axial strain at the centroid of tensile steel (ε_s) and crack spacing parameter (s_{xe}). This is identified as Case 2 in this study:

$$\beta = \frac{4.8}{1+750\varepsilon_s}\frac{51}{39+s_{xe}} \quad \left(\beta = \frac{0.4}{1+750\varepsilon_s}\frac{1300}{1000+s_{xe}}\right) \qquad \text{(AASHTO 5.8.3.4.2-2)} \qquad \textbf{Equation 3.8}$$

$$\theta = (29(degree) + 3500\varepsilon_s) \qquad \text{(AASHTO 5.8.3.4.2-3)} \qquad \textbf{Equation 3.9}$$

$$s_{xe} = s_x\frac{1.38}{a_g+0.63} \quad \left(s_{xe} = s_x\frac{35}{a_g+16}\right) \geq 12\ in \qquad \text{(AASHTO 5.8.3.4.2-5)} \qquad \textbf{Equation 3.10}$$

Where:

s_x = the lesser of d_v or the vertical distance between horizontal layers of longitudinal crack control reinforcement in inches (mm)

a_g = maximum aggregate size in inches (mm), and must equal zero when $f'_c \geq 10\ ksi\ (69\ MPa)$

Note that Equations 3.8 and 3.10 are for the kip-in. units (SI units) system.

If the section has transverse steel less than the minimum transverse steel defined by AASHTO LRFD (Case 2), the specification allows one to check the shear contribution due to aggregate size ($1.38/(a_g+0.63)$) and longitudinal steel (S_x). However, if there is enough longitudinal steel and the aggregate size is efficient, (S_{xe}) must not be less than 12 inches so the factor $\left(\frac{51}{39+s_{xe}}\right) \leq 1$.

3.2.4 Calculation of Longitudinal Axial Strain (ε_s)

Longitudinal axial strain (ε_s) is calculated based on the superimposed effect of the forces in the tension side of the section (see Figure 3.3) as follows:

$$\varepsilon_s = \frac{\frac{|M|}{d_v}+0.5N+V}{A_sE_s} \qquad \text{(AASHTO 5.8.3.4.2-4)} \qquad \textbf{Equation 3.11}$$

Where:

ε_s must not exceed 0.006 to maintain a reasonable crack widening.

If the value of (ε_s) computed from this case is negative (which means the section is under compression), the concrete rigidity is added to the denominator:

$$\varepsilon_s = \frac{\frac{|M|}{d_v} + 0.5N + V}{(A_s E_s + A_c E_c)}$$ (AASHTO 5.8.3.4.2) **Equation 3.12**

Where:

M = moment in k-in. (N-mm)

V = shear force in kip (Newton)

N = axial force, taken as positive if tensile and negative if compressive in kip (Newton)

A_s = area of non-prestressed steel on the flexural tension side of the section in inches^2 (mm^2). This is considered to be the area of flexural reinforcement under the original geometric centroid of the section.

A_c = area of concrete on the flexural tension side of the section in inches^2 (mm^2). This is considered to be the area of concrete below the original geometric centroid of the section.

E_s = modulus of elasticity of steel in ksi (MPa)

E_c = modulus of elasticity of concrete in ksi (MPa)

This procedure assumes a constant distribution of shear stress over an area of depth d_v and width b_v. That means the direction of principal compressive stresses doesn't change over the depth and also shear stresses could be computed from any point of this area.

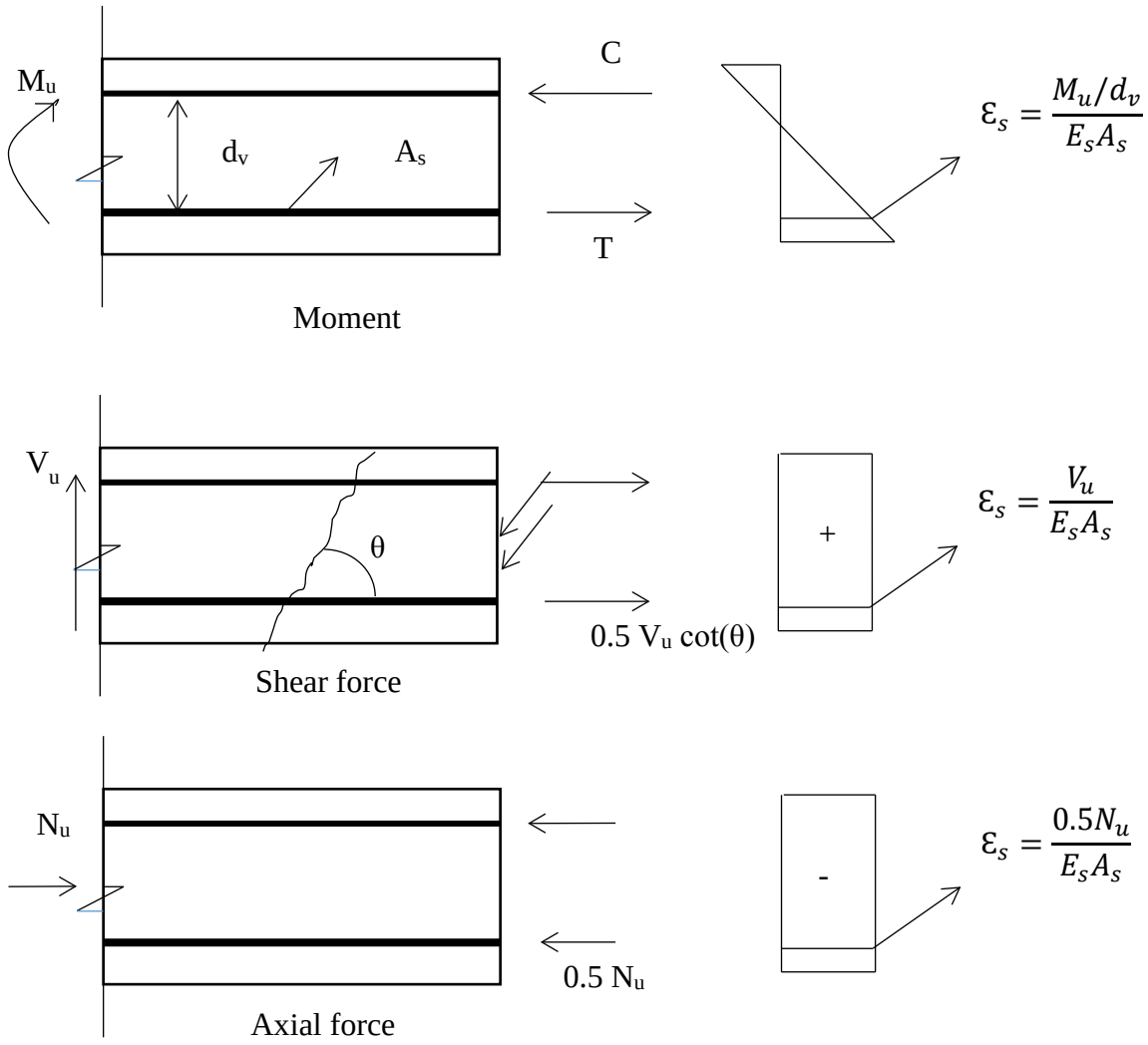

Figure 3.3: Strain Superimposition due to Moment, Shear, and Axial Force

Sections containing at least the minimum transverse steel have the capacity to redistribute shear stresses uniformly over the section (Case 1). Sections containing less than the minimum transverse steel have less capacity to redistribute shear stresses uniformly over the section (Case 2). That is why the crack axial parameter (S_{xe}) and the maximum aggregate size (a_g) are included for further calculations.

3.2.5 Angle of Inclination of Transverse Reinforcement to Longitudinal Axis (α) Calculations

In order to calculate the angle of inclination (α) of transverse spiral reinforcement with respect to the longitudinal axis, the normalized tangent vector of Helix/Spiral equation is calculated. By computing the dot product of the unit tangent vector and the unit vector in the axial direction, the angle of inclination of the transverse spiral reinforcement is determined.

A circular helix of radius ($D_r/2$; core radius) and pitch/spacing (s) is described by the following parameterization (see Figure 3.4 for helix 3D plotting):

$$x(g) = \frac{D_r}{2}\cos(g) \qquad \textbf{Equation 3.13}$$

$$y(g) = \frac{D_r}{2}\sin(g) \qquad \textbf{Equation 3.14}$$

$$z(g) = \frac{s}{2\pi}g \qquad \textbf{Equation 3.15}$$

Tangent vector $= < -\frac{D_r}{2}\sin(g)\,,\ \frac{D_r}{2}\cos(g)\,,\ \frac{s}{2\pi} >$

||Tangent vector|| $= \sqrt{\left(\frac{D_r}{2}\right)^2 + \left(\frac{s}{2\pi}\right)^2}$

Unit tangent vector $(t) = \frac{\text{Tangent vector}}{||\text{ Tangent vector}||}$

Unit vector in the axial direction of the column (k) $= <0, 0, 1>$

The dot product of $< k >.< t > = \frac{s/2\pi}{\sqrt{\left(\frac{D_r}{2}\right)^2+\left(\frac{s}{2\pi}\right)^2}} = 1 * 1 * \cos\alpha$

In the case of the section containing transverse reinforcement of hoops, the angle of inclination of transverse steel to the axial direction (α) is 90°. For sections that contain spiral transverse reinforcement:

$$\alpha = \cos^{-1}\left(\frac{s/2\pi}{\sqrt{\left(\frac{D_r}{2}\right)^2+\left(\frac{s}{2\pi}\right)^2}}\right)$$

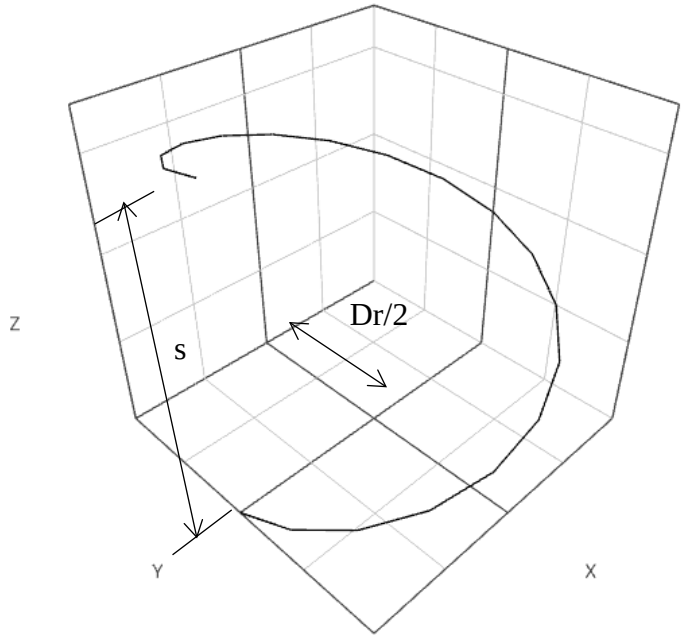

Figure 3.4: Helix/Spiral 3D Plot

3.2.6 Effective Number of Legs of Transverse Steel in Shear Resistance Calculations

Most design codes assume two legs of transverse steel are resisting the shear force, taking $A_v=2A_h$ for circular and rectangular sections. However, a new value for the effective number of legs in circular sections has been defined based on a 45-degree angle of diagonal cracking (Ghee, Priestley, & Paulay, 1989). The new assigned value equals to ($\pi/2$) as an average integrated value along a 45-degree crack; see Figure 3.5 for the geometrical details.

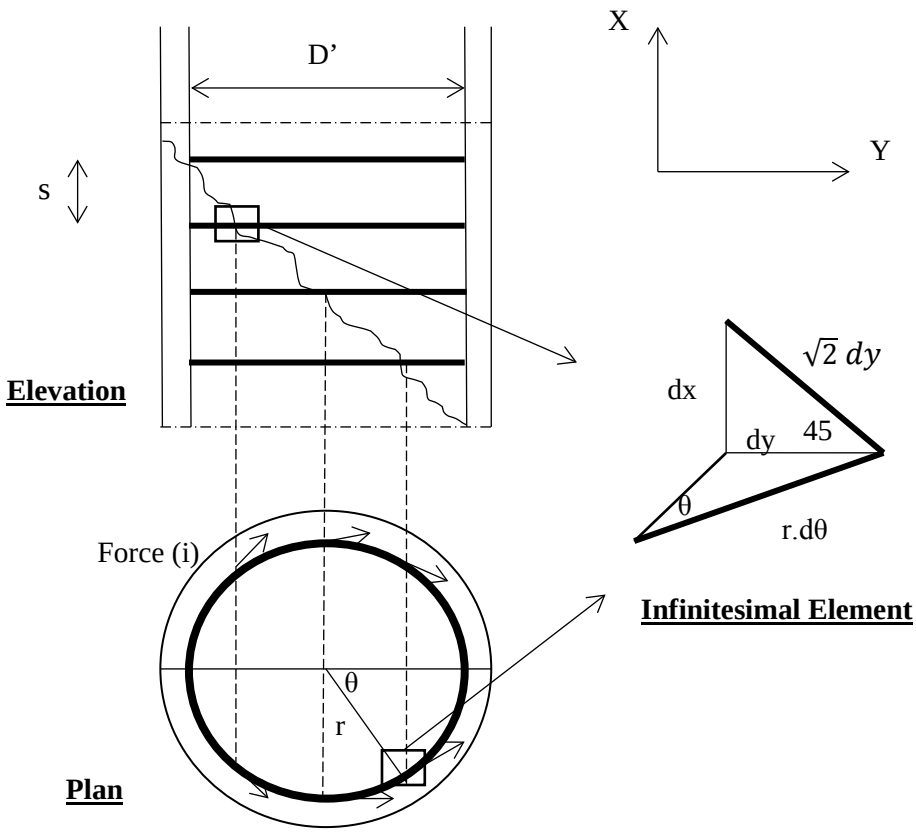

Figure 3.5: Shear Carried by Transverse Steel in Circular Column

The average total force in the transverse steel over the crack length is the summation of each hoop force divided by the length of the crack ($\sqrt{2}\,D'$); in other words, it is the integration of the forces over the length of the crack.

$$V_s = \frac{\int_0^{D'} Forces(i).\sqrt{2}\,dy}{\sqrt{2}\,D'}$$ **Equation 3.16**

Where:

V_s = transverse steel shear resistance.

Force (i) = the transverse steel force in the hoop at the crack location (see Figure 3.5).

In each single hoop, the force in (Y) direction is calculated as follows:

$$Force(i) = 2A_{sh}f_y \sin(\theta)$$ **Equation 3.17**

Where:

A_{sh}= transverse steel single hoop area

Substitute in Equation 3.16:

$$V_s = \frac{\int_0^{D'} 2A_{sh}f_y \sin(\theta).\sqrt{2}\,dy}{\sqrt{2}\,D'}$$ **Equation 3.18**

But from geometry:

$$dy = rd\theta \sin(\theta)$$ **Equation 3.19**

$$D' = 2r$$ **Equation 3.20**

Then:

$$V_s = 2\int_0^{\pi/2} 2A_{sh}f_y sin^2(\theta).d\theta$$ **Equation 3.21**

$$V_s = 2\int_0^{\pi/2} 2A_{sh}f_y \frac{1-\cos(2\theta)}{2}d\theta$$ **Equation 3.22**

$$V_s = 2A_{sh}f_y \left[\frac{\theta}{2} - \frac{sin2\theta}{2}\right]_0^{\pi/2}$$ **Equation 3.23**

$$V_s = \frac{\pi}{2}A_{sh}f_y$$ **Equation 3.24**

3.2.7 FRP Shear Strength Contribution

The FRP shear contribution is calculated based on the transverse FRP reinforcement. FRP shear strength is estimated based on the same model as the transverse steel and it is a function of the effective strain εfe, FRP material stiffness, and FRP reinforcement geometry.

$$V_f = \frac{A_f f_{fe} d_f (cot\theta + cot\alpha) sin\alpha}{s_f}$$ **Equation 3.25**

Where:

A_f = area of FRP shear reinforcement within a distance s_f ($in.^2$)

d_f = effective depth of FRP shear reinforcement equal to d_v for circular sections (in.)

f_{fe} = effective stress of FRP shear reinforcement (ksi)

s_f = center-to-center spacing of FRP shear reinforcement (in.)

V_f = shear resistance provided by FRP shear reinforcement (kip), may only be used when minimum steel shear reinforcement is provided or when the member depth or maximum spacing of distributed longitudinal reinforcement is less than 12 inches.

α_f = angle of inclination of FRP transverse reinforcement to longitudinal axis (°)

The effective stress of FRP shear reinforcement f_{fe} shall be determined as:

$$f_{fe} = E_f \varepsilon_{fe}$$ (NCHRP 678) **Equation 3.26**

In which:

$$\varepsilon_{fe} = R_f \varepsilon_{fu}$$ (NCHRP 678) **Equation 3.27**

Where:

E_f = modulus of elasticity of FRP reinforcement (ksi)

R_f = strain reduction factor to account for the effectiveness of FRP strengthening

ε_{fe} = effective strain of FRP reinforcement; limited to 0.012 when Equation 3.29 is used

ε_{fu} = failure tensile strain of FRP reinforcement

The strain reduction factor (R_f) shall be determined as:

- For completely wrapped or properly anchored U-wrap configurations

$$R_f = 0.088 \leq 4\left(\rho_f E_f\right)^{-0.67} \leq 1$$ (NCHRP 678) **Equation 3.28**

- For un-anchored U-wrap or Two-side bonding configurations

$$R_f = 0.066 \leq 3\left(\rho_f E_f\right)^{-0.67} \leq 1$$ (NCHRP 678) **Equation 3.29**

Where:

ρ_f = FRP shear reinforcement ratio

The FRP shear reinforcement ratio ρ_f shall be determined as:

- For discrete strips:

$$\rho_f = \frac{2n_f t_f w_f}{b_v s_f}$$ (NCHRP 678) **Equation 3.30**

- For continuous sheets:

$$\rho_f = \frac{2n_f t_f}{b_v}$$ (NCHRP 678) **Equation 3.31**

Where:

n_f = number of plies of FRP shear reinforcement

s_f = center-to-center spacing of FRP shear reinforcement strips (in.)

t_f = thickness of FRP plies (in.)

w_f = width of FRP shear reinforcement strips (in.)

Chapter 4: Implementation

4.1 Overview

As a general guideline for our numerical solution approach, the mathematical procedure is based on finding the shear capacity of the section corresponding to a certain level of moment and axial force. By applying this procedure for the full range of moments under a constant axial force, we were able to develop a 2D moment-shear force interaction diagram under a specific axial force. The collection of all the 2D interaction diagrams yielded a 3D interaction diagram of a circular reinforced concrete cross section.

4.2 Input Parameters

In order to apply our numerical approach, a set of parameters needs to be pre-defined. These parameters could be classified into material properties, reinforcement, and geometry.

1. Material Properties: Yielding strength for longitudinal (f_y) and transverse bars (f_{yh}), concrete compressive strength (f'_c), modulus of elasticity of steel (E_s), and the modulus of elasticity for FRP (E_f) and FRP ultimate strain (ε_{fu}) were defined as the material properties. Modulus of elasticity of concrete (E_c) was calculated based on the concrete compressive strength $E_c = 57\sqrt{f'c}$ ($E_c = 4700\sqrt{f'c}$) where f'_c is in psi (MPa) units and E_c is in ksi (MPa) units.

2. Reinforcement Properties: The reinforcement parameters are the number of longitudinal bars, longitudinal bars' cross-section dimensions (diameter, area [A_s]), transverse bars' cross-section dimensions (diameter, area [A_v]), the type of transverse reinforcement (hoop or spiral), and the transverse bars spacing (s). For FRP reinforcement, the number of plies (n) and the thickness of each ply (t_f) were determined, as well as the plies spacing (s_f) and width (w_f).

3. Geometric Properties: Circular cross-section diameter (d) and clear cover (cc) were the two direct geometrical parameters used in this analysis. Effective shear depth (d_v) and effective web width (b_v) are two indirect geometrical parameters needed to calculate steel and concrete shear capacities.

4.3 Effective Shear Area

In our case of reinforced concrete circular sections, it was agreed to use the effective web width as the diameter of the circular section per the AASHTO requirements, although it is less conservative as it increases the value of concrete shear capacity (V_c). It also seems to contradict the main definition of effective web width as the minimum web width of the section. However, according to the specifications, circular members typically have the longitudinal steel uniformly distributed around the perimeter of the section, and when the member cracks, the highest shear stresses occur near the mid-depth of the cross section. It is for this reason the effective web width was taken by AASHTO to be the diameter. For the centroid location of the tensile force, the neutral axis of the cross section is assumed by AASHTO LRFD to be always across the middle of the section at a depth equal to d/2. This assumption was expected to decrease the moment capacity of the section, which is more conservative than Figure 3.1.

4.3.1 Effective Shear Depth Calculation (d_v)

- $d_v = \text{Max}\{0.72h, 0.9d_e, d_v\}$
- d_e = the distance from the upper compressive fiber to the resultant of tensile forces in inches (mm)

$$d_e = d/2 + d_r/\pi$$ (AASHTO C5.8.2.9-2) **Equation 4.1**

Where:

d = diameter of section in inches (mm)

d_r = diameter of the circle passing through the centers of the longitudinal bars in inches (mm)

The second term in Equation 4.1 represents the geometric centroid of a semicircular ring.

- d_v = distance between the compressive resultant point of action and the tensile resultant point of action in inches (mm). According to AASHTO specification (d_v) could be approximated as follows by assuming ALL the tensile steel to yield:

$$d_v = \frac{M}{A_s f_y} \qquad \text{(AASHTO C5.8.2.9-1)} \qquad \textbf{Equation 4.2}$$

4.4 Analysis Procedure

Under a constant axial compressive force (N), the moment-shear interaction diagram is determined by increasing the value of the moment from zero to the ultimate confined moment capacity corresponding to zero-shear while solving for the total shear capacity under every moment step. The ultimate confined moment capacity at zero-shear and axial force (N) is readily available from the procedure developed earlier by Abd El Fattah, Rasheed, and Esmaeily (2011). At a zero moment value, the shear capacity is estimated first based on a 45° angle of shear crack (cot θ=1) and a concrete strength based on ($\varepsilon_s = 0.00457$, β= 1.084). This shear capacity is then used along with the axial force (N) to determine (ε_s), based on Equation 3.10. The longitudinal strain at the centroid of tensile reinforcement (ε_s) is then used to compute θ and β based on Equations 3.10 and 3.6 or Equations 3.7, 3.8, and 3.9 for sections having less transverse steel than minimum transverse steel defined by AASHTO LRFD (Equation 3.1). The concrete and steel shear capacities are determined next using Equations 3.3 and 3.4 and totaled using Equation 3.2 to update the section shear strength (V). If that value is equal to the initially estimated shear capacity, then convergence is achieved. Otherwise, the updated shear capacity is used to re-iterate until convergence of the newly updated shear capacity (see Figure 4.2). Once the new moment step is input, the shear capacity of the previous step, along with (N), is used to compute (ε_s) and iterations are resumed until the new shear capacity convergences. The interaction diagram is concluded when the moment step reaches the ultimate confined moment capacity corresponding to zero-shear (see Figure 4.1).

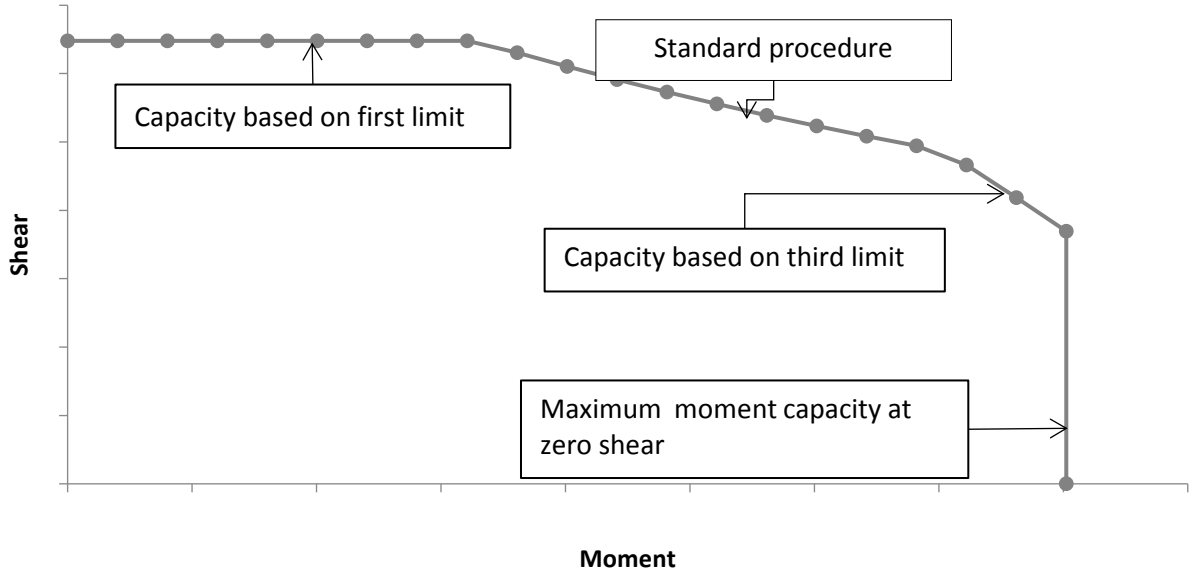

Figure 4.1: Moment-Shear Interaction Diagram Under a Constant Axial Compression Force

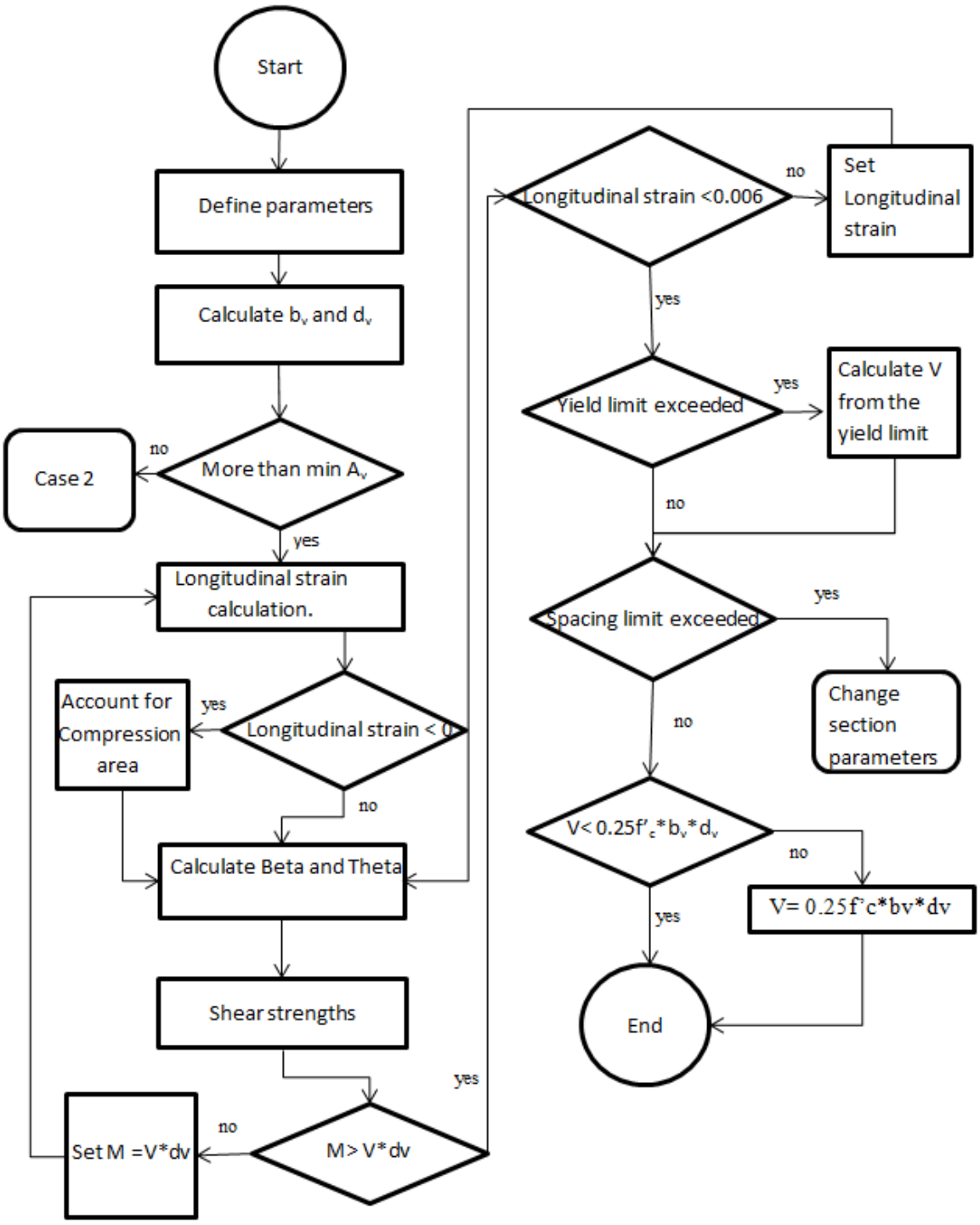

Figure 4.2: Flow Chart of Present Procedure (Case 1: Sections with More than Minimum Transverse Steel)

4.4.1 Limits of Constraints

The value of the shear capacity (V) should satisfy five other limits according to AASHTO LRFD Specifications.

1. The first limit is $[M \geq V d_v]$. If this limit is not achieved at a moment step, the iteration should be repeated with an initial value of moment (M) equal to ($V.d_v$).
2. The second limit is $[\varepsilon_s \leq 0.006]$. If not, ($\varepsilon_s$) is set to 0.006, and the shear capacity (V) is directly calculated.
3. The third limit or the yield limit is $[A_s f_y \geq \frac{M}{d_v} + \frac{N}{2} + V\cot(\theta) - 0.5V_s\cot(\theta) - -0.5V_f\cot(\theta)]$. If not, the shear capacity value (V) should be reduced according to this limit.
4. The fourth limit is the spacing limit; if $[v_u = \frac{V}{b_v d_v} < 0.125 f_c']$, then the max spacing of transverse steel and transverse FRP plies equals $0.8 * d_v \leq 24\ in.\ (609.6\ mm)$. And if $[v_u = \frac{V}{b_v d_v} \geq 0.125 f_c']$, then the max spacing equals $0.4 * d_v \leq 12\ \ in.\ (304.8\ mm)$. If this limit is not achieved, the analysis is stopped warning the user to decrease the spacing to satisfy this limit.
5. The fifth limit is $[V \leq 0.25 * f_c' * d_v * b_v]$, otherwise the shear value set to be $[V = 0.25 * f_c' * d_v * b_v]$.

The first limit controls when the moment value approaches the point of zero moment (e.g., simple beam support). The specification assigned a moment value equal to $V.d_v$ over the length where moment is negligible. This limit causes a horizontal line at the top of shear-moment interaction diagram (see Figure 4.1). The second limit illustrates that the tensile strain of longitudinal steel on the tension side should not exceed an excessive value in order to keep cracks width within a reasonable value in order to effectively transmit tension along the member. The third limit formula could be derived from Figure 4.3, by taking the moment summation around point O, and it aims to ensure that the force in the longitudinal steel is equal to or less than the maximum force which could be carried by the steel. The fourth limit is to minimize the diagonal

shear crack width by having enough transverse steel within the spacing (s) to resist shear stresses. The fifth limit was intended to ensure that the concrete strut will not crush before the transverse steel yields.

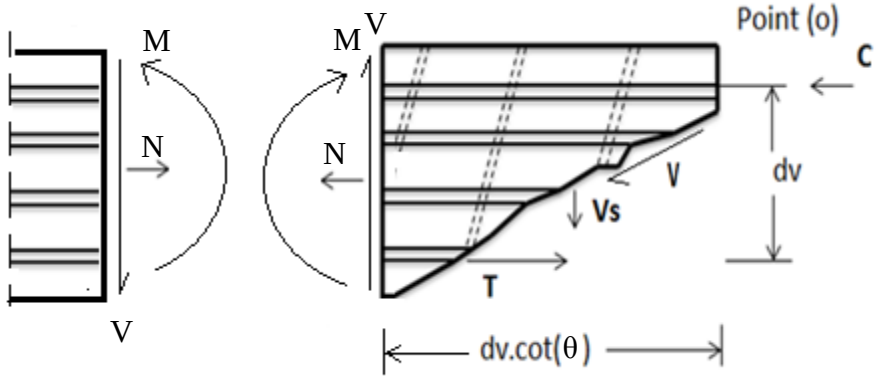

Figure 4.3: Derivation of the Yielding Stress Limit

There are two more conditions that cause the AASHTO LRFD to consider the section invalid if one of them was met, and new section properties are then recommended.

The first condition is in the case of sections having less than the minimum transverse steel defined by AASHTO LRFD (Equation 3.1). If the section doesn't have enough longitudinal steel to control cracks along its diameter according to the following equation, the section is considered invalid:

$$A_{layer} = 0.003 b_v s_x \qquad \textbf{Equation 4.3}$$

Where: (A_{layer}) is the area of longitudinal steel in each layer of reinforcement ($in.^2$)

More longitudinal bars or bigger bars are then recommended to control cracks.

The second condition is to make sure that there is a clear yielding zone in the steel stress-strain curve. Thus, the steel yielding strength should not exceed 100 ksi (see Figure 4.4). This value was verified for both prestressed and non-prestressed members for nonseismic applications (Shahrooz, Miller, Harries, & Russell, 2011).

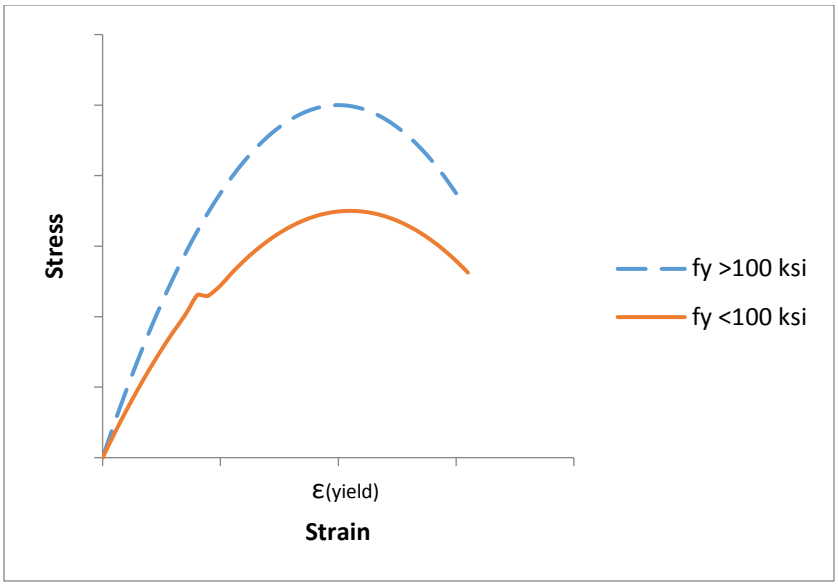

Figure 4.4: Yielding Zone for Different Yielding Strength

Chapter 5: Experimental Verification

5.1 Overview

The proposed formulations were verified against various experimental data performed by different researchers in different countries. The selected sections are discussed in detail with necessary comments in this chapter. A parametric study to examine the effect of the different geometrical and material variables was performed and is presented in this chapter.

5.2 Database Criteria

The database presented in this chapter represents various experimental studies. However, the selected sections in this study had to match certain criteria defined by AASHTO (2014) *LRFD Bridge Design Specification* and the research goals regarding loads, geometry, and materials. The first condition regarding loads is that the axial force applied on the section should be compressive force $N \leq 0\ kips$ (assuming negative sign for compression); the interaction diagrams in this study were generated for the axial compression forces range. In terms of geometry, the transverse steel spacing must not exceed the maximum spacing defined by AASHTO LRFD (see Section 4.4.1). The last condition is that the steel yielding strength should not exceed 100 ksi in order to have a clear yielding zone.

5.3 Comparisons Against Experimental Studies

Seventeen different sections were selected from literature to be discussed in this chapter (see Table 5.1). Table 5.2 shows their material and geometrical properties. The table also shows the applied constant axial force, and moment and shear failure values. The ratio (L_a/D) in the table is the ratio of the effective column length to its diameter and it tends to relate the applied lateral force to the resulting moment according to the following relationship.

$$\frac{M}{VD} = \frac{L_a}{D}$$ **Equation 5.1**

Where:

(M) is the moment at the base of the cantilever,

(V) is the applied shear force,

(D) is column diameter, and

(L) is the effective length of the column.

In case of a cantilever column, the effective length is the full length of the column.

Table 5.1: Experimental Data Geometrical and Material Properties

Reference	D (in.)	CC (in.)	# of bars	Bar Diameter (in.)	Spacing (in.)	Trans. bar Diameter (in.)	f'_c (ksi)	f_y (ksi)	f_{yt} (ksi)
Kawashima, Hosotani, and Yoneda (2000)	15.76	0.985	12	0.625	5.91	0.23	4.35	52.36	52.635
	15.76	0.985	12	0.625	5.91	0.23	4.35	52.36	52.635
	15.76	0.985	12	0.625	5.91	0.23	3.9875	52.36	52.635
	15.76	0.985	12	0.625	11.82	0.23	4.35	52.36	52.635
	15.76	0.985	12	0.625	11.82	0.23	4.35	52.36	52.635
	15.76	0.985	12	0.625	11.82	0.23	3.98	52.36	52.635
Liu and Sheikh (2013)	**D (in.)**	**CC (in.)**	**# of bars**	**Bar Diameter (in.)**	**Spacing (in.)**	**Trans. bar Diameter (in.)**	**f'_c (ksi)**	**f_y (ksi)**	**f_{yt} (ksi)**
	14	0.8	6	0.79	12	0.375	5.8	72	72
	14	0.8	6	0.79	12	0.375	5.8	72	72
	14	0.8	6	0.79	12	0.375	5.8	72	72
	14	0.8	6	0.79	12	0.375	5.8	72	72
	14	0.8	6	0.79	12	0.375	5.8	72	72
	14	0.8	6	0.79	12	0.375	5.8	72	72
	14	0.8	6	0.79	12	0.375	5.8	72	72
	14	0.8	6	0.79	12	0.375	5.8	72	72
Siddiqui, Alsayed, Al-Salloum, Iqbal, and Abbas (2014)	**D (in.)**	**CC (in.)**	**# of bars**	**Bar Diameter (in.)**	**Spacing (in.)**	**Trans. bar Diameter (in.)**	**f'_c (ksi)**	**f_y (ksi)**	**f_{yt} (ksi)**
	5.91	0.985	4	0.31	3.94	0.23	5.09	61	40
	5.91	0.985	4	0.31	3.94	0.23	5.09	61	40
	5.91	0.985	4	0.31	3.94	0.23	5.09	61	40

Table 5.2: Experimental Data FRP Properties

Unit	# of FRP layers	FRP scheme	Thickness (in.)	E (ksi)	εfu
Kawashima, Hosotani, and Yoneda (2000)	0		0.0043734	38,570	0.0163
	1	Fully Wrapped	0.0043734	38,570	0.0163
	2	Fully Wrapped	0.0043734	38,570	0.0163
	0		0.0043734	38,570	0.0163
	1	Fully Wrapped	0.0043734	38,570	0.0163
	2	Fully Wrapped	0.0043734	38,570	0.0163
Liu and Sheikh (2013)	**# of FRP layers**	**FRP scheme**	**Thickness (in.)**	**E (ksi)**	**εfu**
	1	Fully Wrapped	0.039	11,083	0.01229
	2	Fully Wrapped	0.049	3,696	0.02031
	0		0		
	1	Fully Wrapped	0.039	11,083	0.01229
	1	Fully Wrapped	0.049	3,696	0.02031
	0		0		
	2	Fully Wrapped	0.039	11,083	0.01229
	3	Fully Wrapped	0.049	3,696	0.02031
Siddiqui, Alsayed, Al-Salloum, Iqbal, and Abbas (2014)	**# of FRP layers**	**FRP scheme**	**Thickness (in.)**	**E (ksi)**	**εfu**
	1	Fully Wrapped	0.03941	11,208	0.011
	1	Fully Wrapped	0.03941	11,208	0.011
	1	Fully Wrapped	0.03941	11,208	0.011

Table 5.3: Experimental Data Loading Properties

Unit	Axial force (kips)	Moment (k.ft)	Shear Force (kips)
Kawashima, Hosotani, and Yoneda (2000)	41.625	1,394.243	26.2125
	41.625	1,531.872	28.8
	41.625	1,603.679	30.15
	41.625	1,412.195	26.55
	41.625	1,546.832	29.08125
	41.625	1,621.63	30.4875
Liu and Sheikh (2013)	**Axial force (kips)**	**Moment (k.ft)**	**Shear Force (kips)**
	290.639232	2,340	26.7
	290.639232	2,220	23.6
	430.57664	1,596	20.9
	430.57664	2,316	22.2
	430.57664	2,280	26
	602.807296	1,668	20.5
	602.807296	2,928	22
	602.807296	2,988	24.6
Siddiqui, Alsayed, Al-Salloum, Iqbal, and Abbas (2014)	**Axial force (kips)**	**Moment (k.ft)**	**Shear Force (kips)**
	112.5	154.77	6.5469543
	78.75	123.816	3.491709
	72	106.128	2.2446701

5.3.1 Kawashima, Hosotani, and Yoneda (2000)

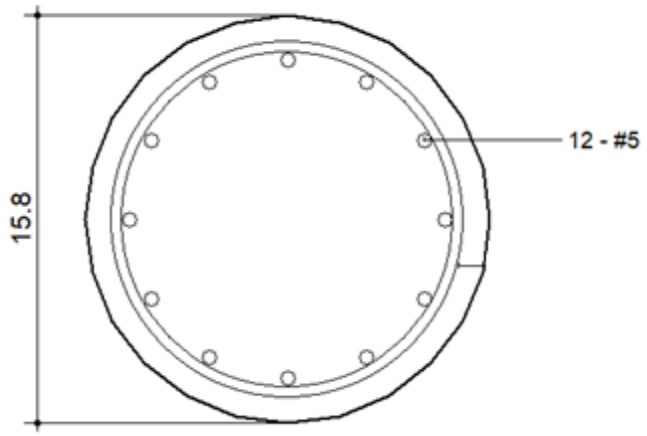

Figure 5.1: Kawashima et al. (2000) Cross Section

f_y = 52.36 ksi

f_{yt} = 55.63 ksi

f'_c = 4.35 ksi

Axial force = 41.6 kips

Transverse steel spacing = 5.9 in.

Unstrengthened Control Column

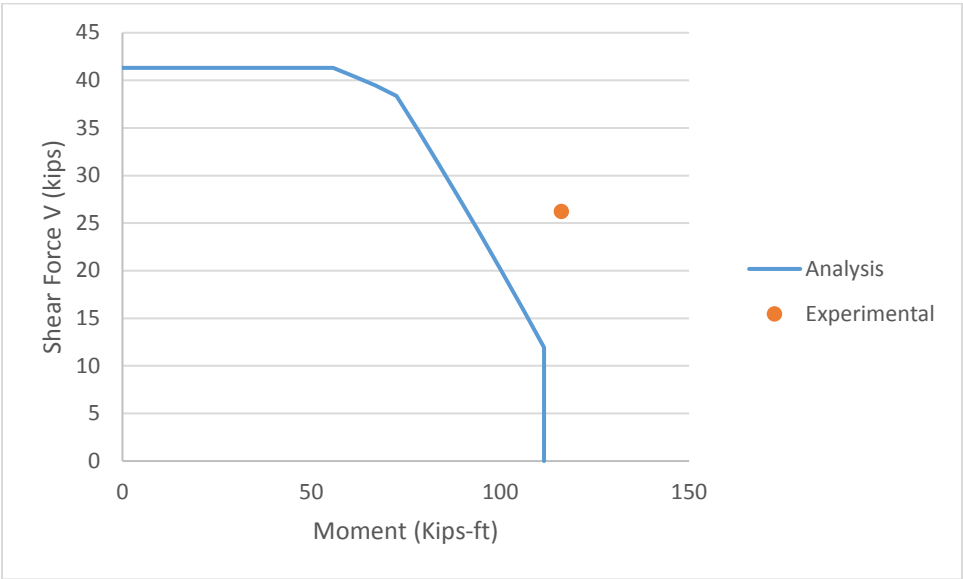

Figure 5.2: Kawashima et al. (2000) Control Interaction Diagram (Group 1)

This column was tested by Kawashima, Hosotani, and Yoneda (2000) under 42.6 kips applied axial force. The section is unstrengthened section. The section failed due to moment-shear effect close to the inclined zone of the interaction diagram. The proposed interaction diagram is conservative and fairly accurate comparing to the failure point.

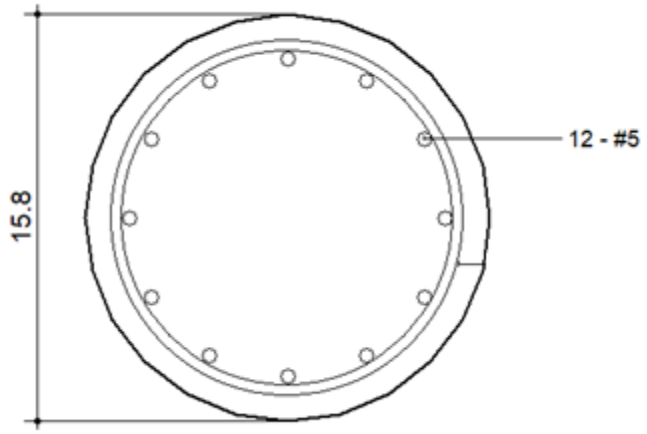

Figure 5.3: Kawashima et al. (2000) Cross Section

f_y = 52.36 ksi

f_{yt} = 55.63 ksi

f'_c = 4.35 ksi

Transverse steel spacing = 5.9 in.

Axial force = 41.6 kips

One layer of carbon fiber-reinforced polymer (CFRP)

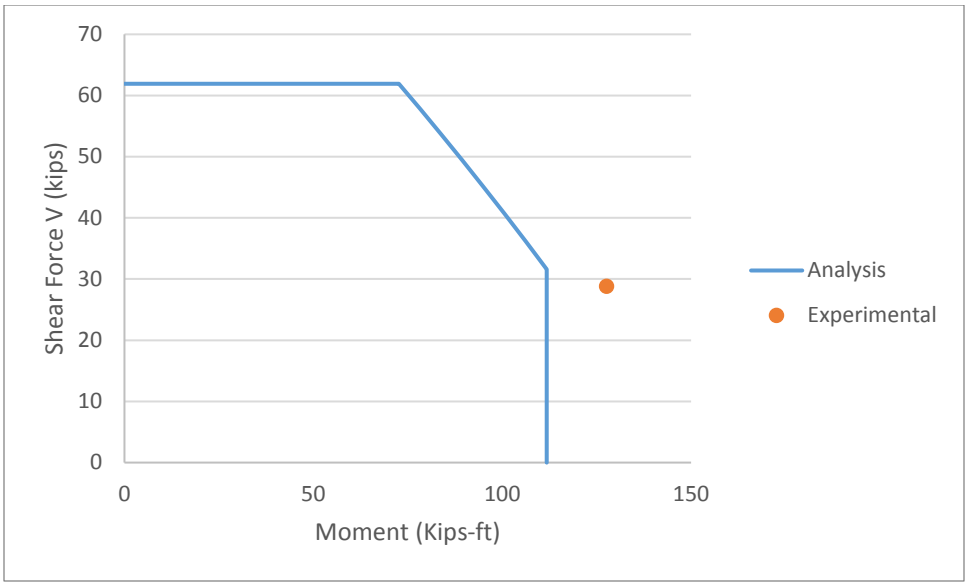

Figure 5.4: Kawashima et al. (2000) Interaction Diagram (One Layer of FRP)

This column was tested by Kawashima et al. (2000) under 42.6 kips applied axial force. The column was fully wrapped with one layer of CFRP as an external reinforcement. The section failed due to moment-shear effect close to the inclined zone of the interaction diagram. The proposed interaction diagram is conservative and fairly accurate comparing to the failure point. The interaction diagram shows a significant improvement over the previous control column; 20 kips at the flat plateau was observed over the control column.

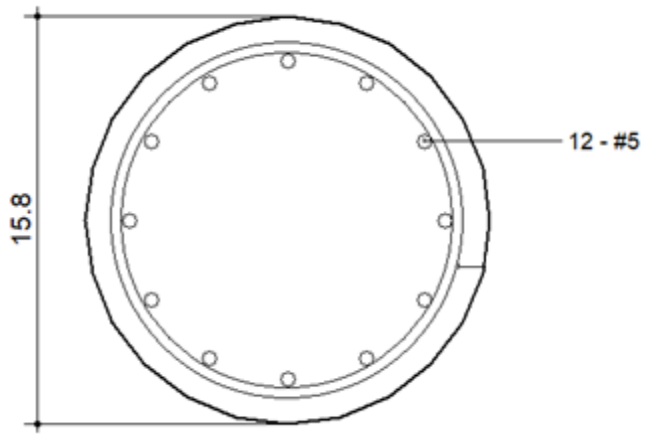

Figure 5.5: Kawashima et al. (2000) Cross Section

f_y = 52.36 ksi

f_{yt} = 55.63 ksi

f'_c = 3.98 ksi

Transverse steel spacing = 5.9 in.

Axial force = 41.6 kips

Two layers of CFRP

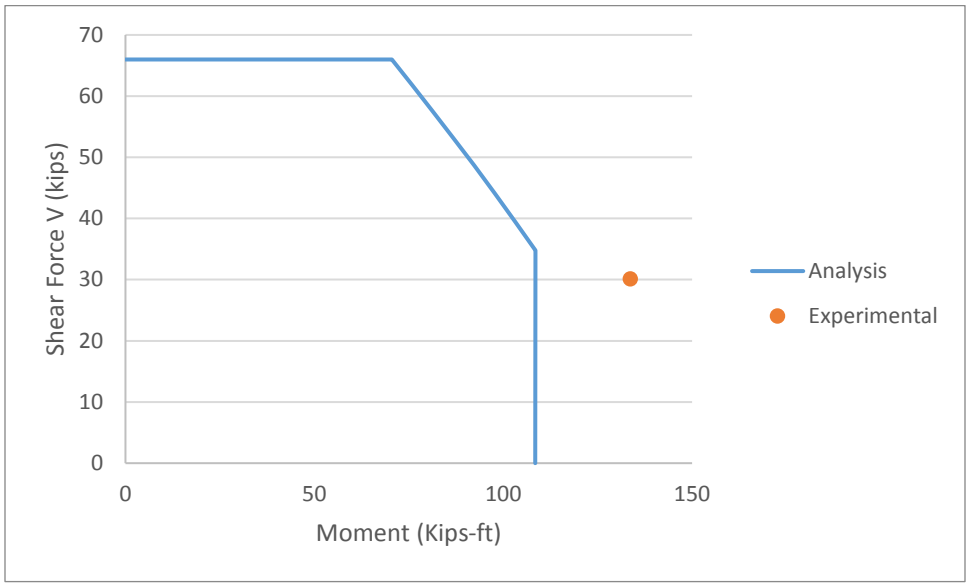

Figure 5.6: Kawashima et al. (2000) Interaction Diagram (Two Layers of FRP)

This column was tested by Kawashima et al. (2000) under 42.6 kips applied axial force. The column was fully wrapped with two layers of CFRP as an external reinforcement. The section failed due to moment-shear effect close to the inclined zone of the interaction diagram. The proposed interaction diagram is conservative and fairly accurate comparing to the failure point. The interaction diagram shows a significant improvement over the control column; however, two layers of CFRP only shows 5 kips difference over one layer of CFRP at the constant shear zone.

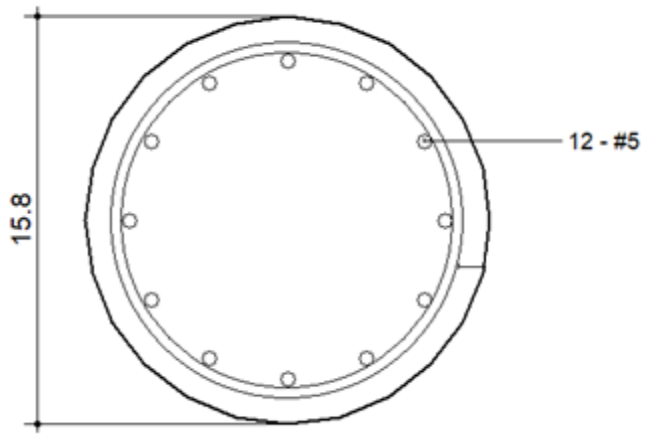

Figure 5.7: Kawashima et al. (2000) Cross Section

f_y = 52.36 ksi

f_{yt} = 55.63 ksi

f'_c = 4.35 ksi

Transverse steel spacing = 11.8 in.

Axial force = 41.6 kips

Unstrengthened Control Column

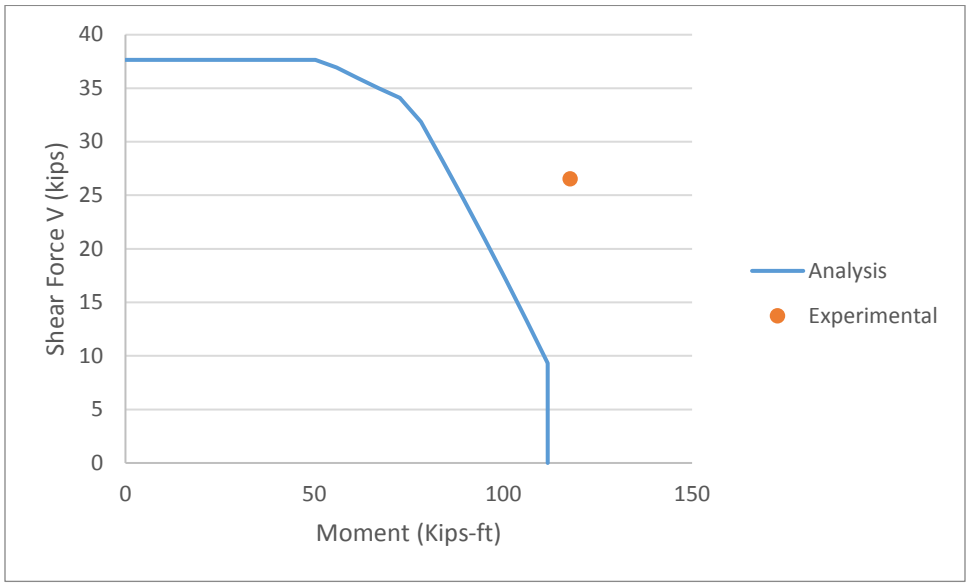

Figure 5.8: Kawashima et al. (2000) Control Interaction Diagram (Group 2)

This column is the second control column tested by Kawashima et al. (2000) under 42.6 kips applied axial force and double the transverse steel spacing. The section is unstrengthened. The section failed due to moment-shear effect close to the inclined zone of the interaction diagram. The proposed interaction diagram is conservative and fairly accurate comparing to the failure point.

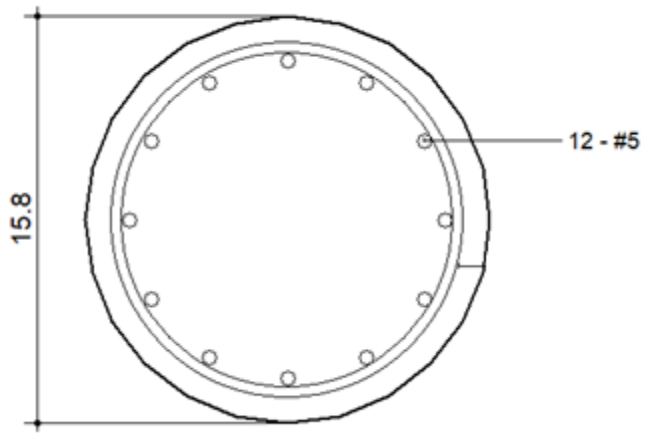

Figure 5.9: Kawashima et al. (2000) Cross Section

f_y = 52.36 ksi

f_{yt} = 55.63 ksi

f'_c = 4.35 ksi

Transverse steel spacing = 11.8 in.

Axial force = 41.6 kips

One layer of CFRP

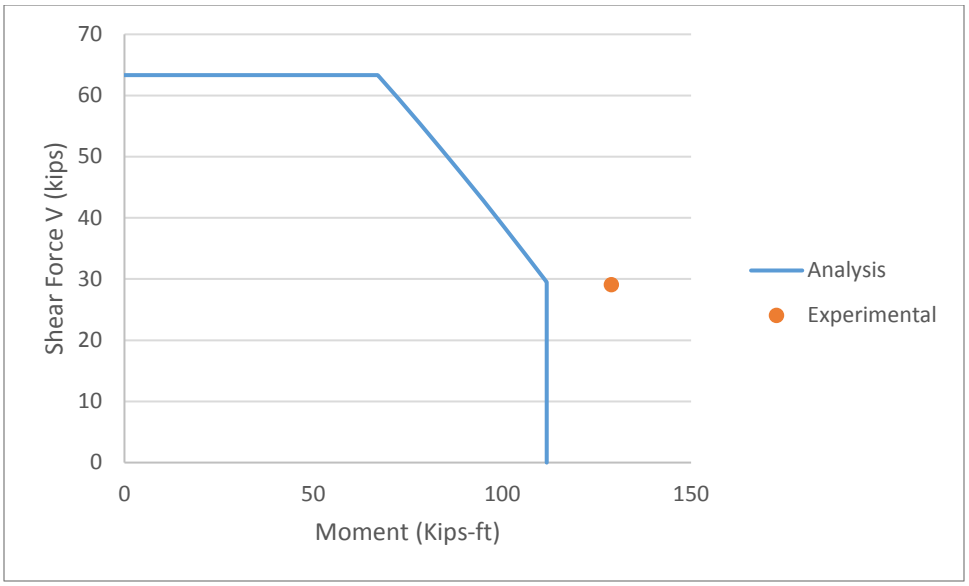

Figure 5.10: Kawashima et al. (2000) Interaction Diagram (One Layer of FRP)

This column was tested by Kawashima et al. (2000) under 42.6 kips applied axial force. The column was fully wrapped with one layer of CFRP as an external reinforcement. The section failed due to moment-shear effect close to the inclined zone of the interaction diagram. The proposed interaction diagram is conservative and fairly accurate comparing to the failure point. The interaction diagram shows a significant improvement over the previous control column; 25 kips at the flat plateau was observed over the control column.

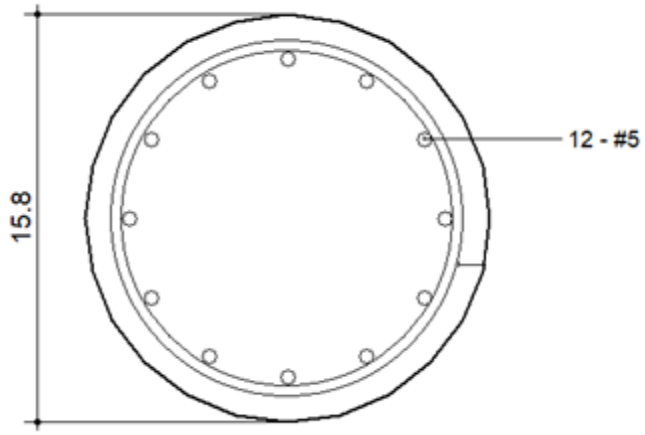

Figure 5.11: Kawashima et al. (2000) Cross Section

f_y = 52.36 ksi

f_{yt} = 55.63 ksi

f'_c = 3.98 ksi

Transverse steel spacing = 11.8 in

Axial force = 41.6 kips

Two layers of CFRP

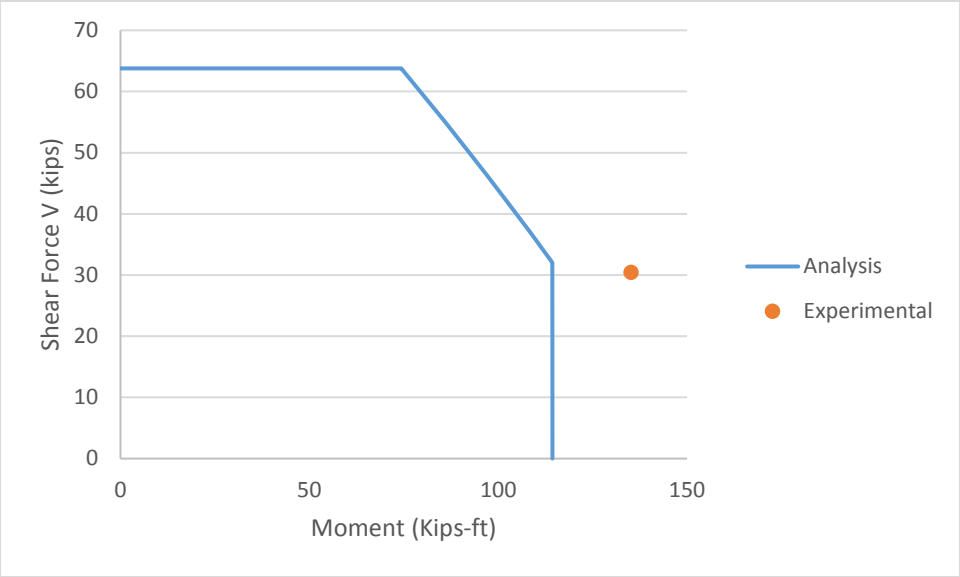

Figure 5.12: Kawashima et al. (2000) Interaction Diagram (Two Layers of FRP)

This column was tested by Kawashima et al. (2000) under 42.6 kips applied axial force. The column was fully wrapped with two layers of CFRP as an external reinforcement. The section failed due to moment-shear effect close to the inclined zone of the interaction diagram. The proposed interaction diagram is conservative and fairly accurate comparing to the failure point. The interaction diagram shows a significant improvement over the control column; however, two layers of CFRP shows insignificant improvement over one layer of CFRP.

5.3.2 Liu and Sheikh (2013)

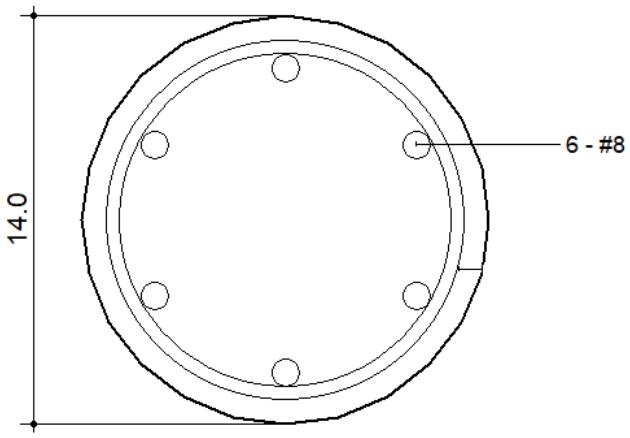

Figure 5.13: Liu and Sheikh (2013) Cross Section

f_y = 72 ksi

f_{yt} = 72 ksi

f'_c = 5.8 ksi

Axial force = 290 kips

One layer of CFRP

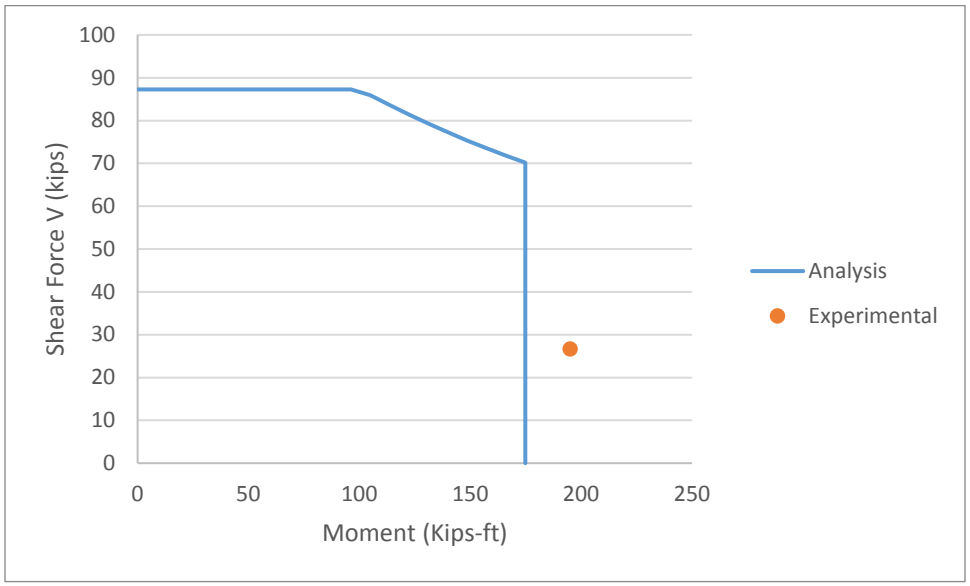

Figure 5.14: Liu and Sheikh (2013) Interaction Diagram (P=290 kips; One Layer of CFRP)

This column was tested by Liu and Sheikh (2013) under 290 kips axial force. The section was strengthened by one layer of CFRP, fully wrapped over the column length. The proposed interaction diagram is conservative and fairly accurate comparing to the failure point.

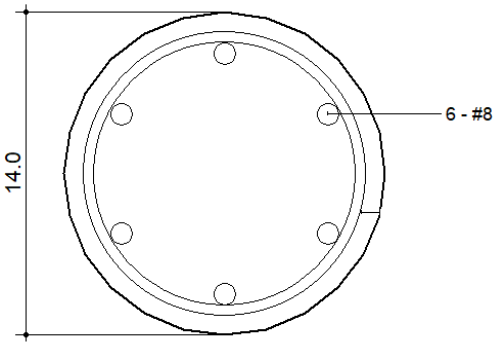

Figure 5.15: Liu and Sheikh (2013) Cross Section

f_y = 72 ksi

f_{yt} = 72 ksi

f'_c = 5.8 ksi

Axial force = 290 kips

Two layers of glass fiber-reinforced polymer (GFRP)

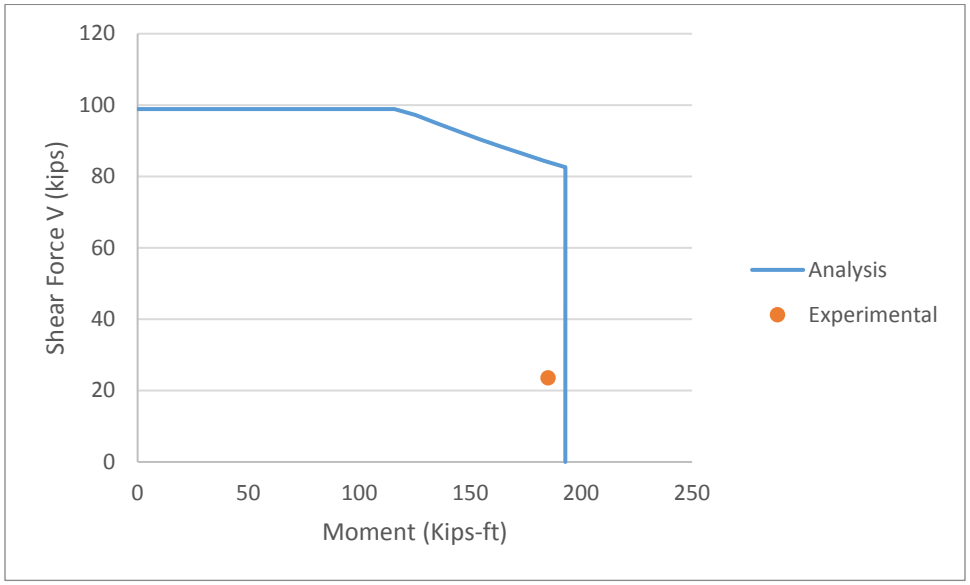

Figure 5.16: Liu and Sheikh (2013) Interaction Diagram (P=290 kips; One Layer of GFRP)

This column was tested by Liu and Sheikh (2013) under 290 kips axial force. The section was strengthened by two layers of GFRP, fully wrapped over the column length. The proposed interaction diagram slightly over-predicted the pure bending moment within 3% difference; however, the interaction diagram is fairly accurate comparing to the failure point. Two layers of GFRP shows a significant improvement over one layer of CFRP by 12 kips difference at pure shear point.

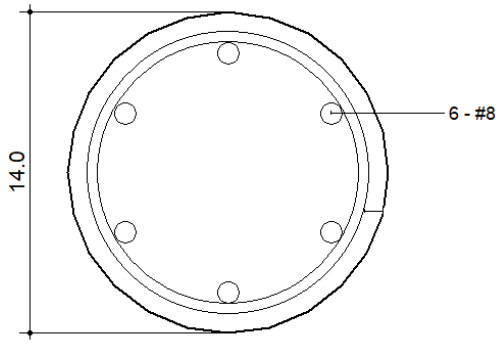

Figure 5.17: Liu and Sheikh (2013) Cross Section

f_y = 72 ksi

f_{yt} = 72 ksi

f'_c = 5.8 ksi

Axial force = 430 kips

One layer of CFRP

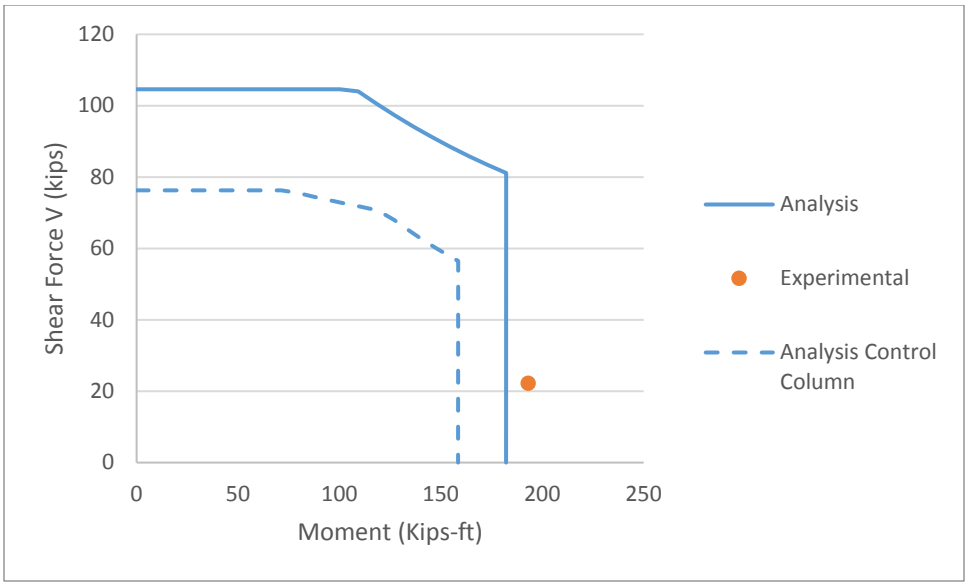

Figure 5.18: Liu and Sheikh (2013) Interaction Diagram (P=430 kips; One Layer of CFRP)

This column was tested by Liu and Sheikh (2013) under 430 kips axial force. The section was strengthened by one layer of CFRP, fully wrapped over the column length. The proposed interaction diagram is conservative and fairly accurate comparing to the failure point.

One layer of CFRP shows a significant improvement over the control column under the same axial load; one layer of CFRP added around 24 kips-ft for the bending moment capacity and over 20 kips for pure shear capacity.

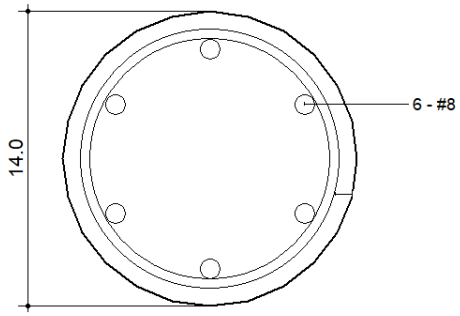

Figure 5.19: Liu and Sheikh (2013) Cross Section

f_y = 72 ksi

f_{yt} = 72 ksi

f'_c = 5.8 ksi

Axial force = 430 kips

One layer of GFRP

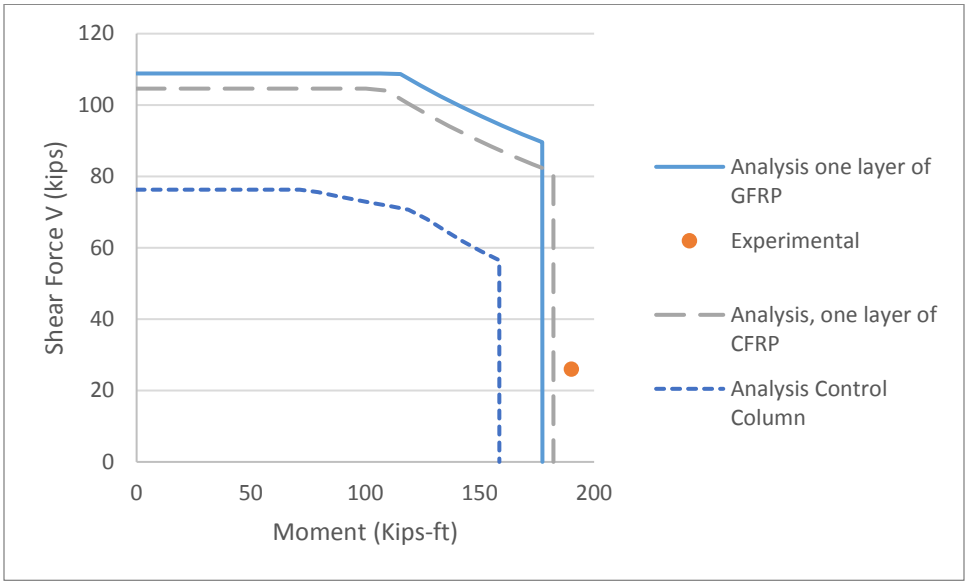

Figure 5.20: Liu and Sheikh (2013) Interaction Diagram (P=430 kips; One Layer of GFRP)

This column was tested by Liu and Sheikh (2013) under 430 kips axial force. The section was strengthened by one layer of GFRP, fully wrapped over the column length. The proposed interaction diagram is conservative and fairly accurate comparing to the failure point.

One layer of GFRP shows a significant improvement over the control column under the same axial load. However, one layer of GFRP with 0.049-in. thickness shows a similar improvement in shear and bending of one layer of CFRP with 0.039-in. thickness.

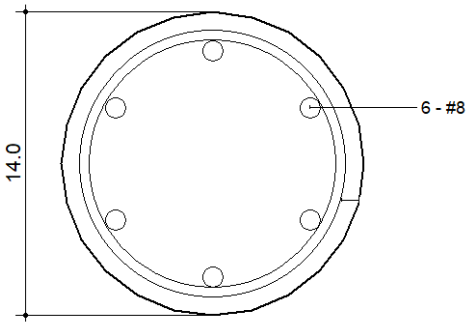

Figure 5.21: Liu and Sheikh (2013) Cross Section

f_y = 72 ksi

f_{yt} = 72 ksi

f'_c = 5.8 ksi

Axial force = 602 kips

Unstrengthened Control Column

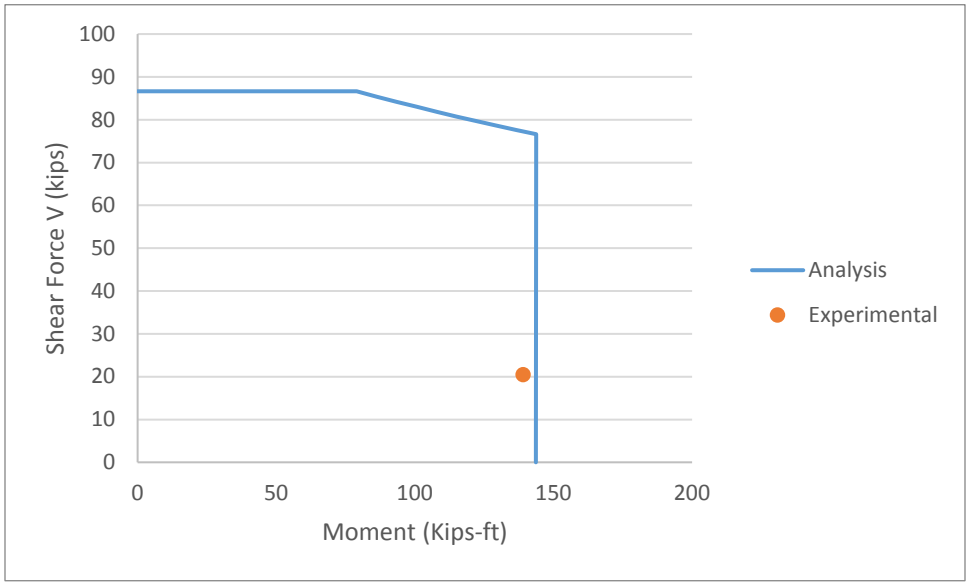

Figure 5.22: Liu and Sheikh (2013) Interaction Diagram (P=602 kips; Control Column)

This column was tested by Liu and Sheikh (2013) under 602 kips axial force. The section was unstrengthened. The proposed interaction diagram is fairly accurate comparing to the failure point.

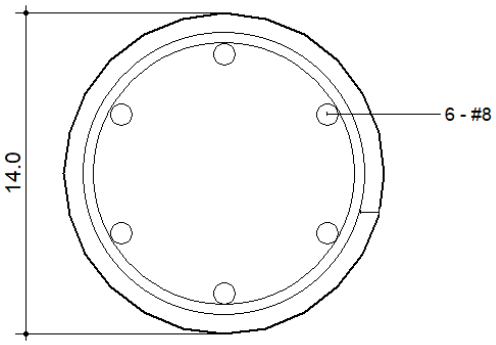

Figure 5.23: Liu and Sheikh (2013) Cross Section

f_y = 72 ksi

f_{yt} = 72 ksi

f'_c = 5.8 ksi

Axial force = 602 kips

Two layers of CFRP

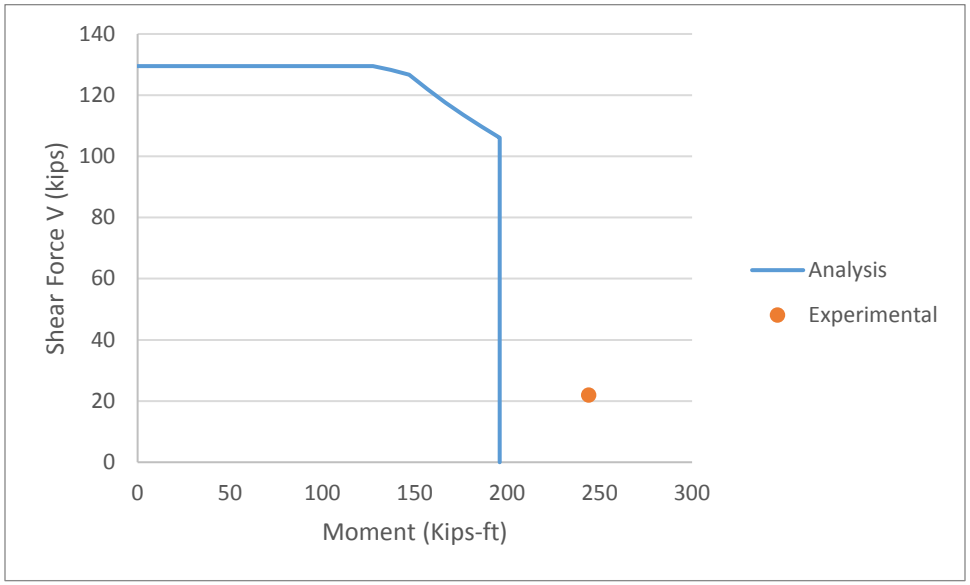

Figure 5.24: Liu and Sheikh (2013) Interaction Diagram (P=602 kips; Two Layers of CFRP)

This column was tested by Liu and Sheikh (2013) under 602 kips axial force. The section was strengthened by two layers of CFRP, fully wrapped over the column length. The proposed interaction diagram is conservative and fairly accurate comparing to the failure point. Similar to

the previous results, one layer of CFRP shows a significant improvement over the control column under the same axial load.

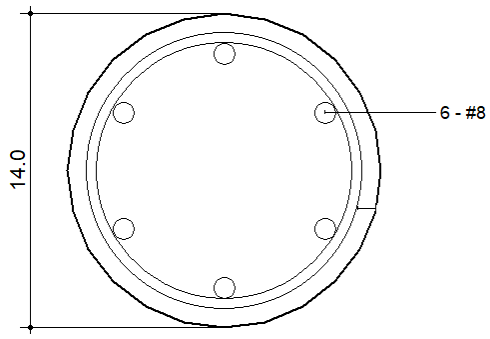

Figure 5.25: Liu and Sheikh (2013) Cross Section

f_y = 72 ksi

f_{yt} = 72 ksi

f'_c = 5.8 ksi

Axial force = 602 kips

Three layers of GFRP

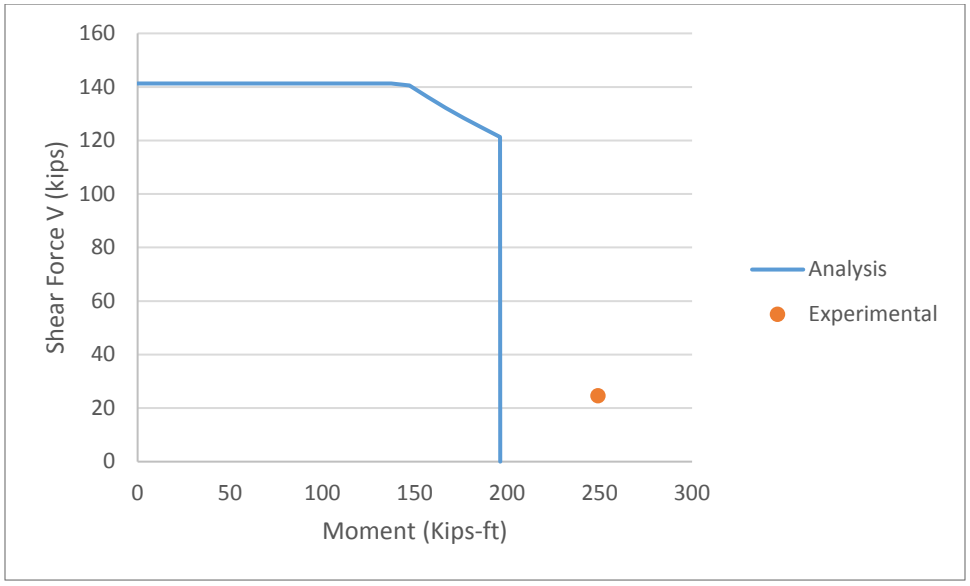

Figure 5.26: Liu and Sheikh (2013) Interaction Diagram (P=602 kips; Three Layers of CFRP)

This column was tested by Liu and Sheikh (2013) under 602 kips axial force. The section was strengthened by three layers of GFRP, fully wrapped over the column length. The proposed interaction diagram is conservative and fairly accurate comparing to the failure point. The use of three layers of GFRP didn't show a significant improvement over two layers of CFRP at the vertical zone corresponding to pure moment, and it only shows around 10 kips improvement at pure shear.

5.3.3 Siddiqui, Alsayed, Al-Salloum, Iqbal, and Abbas (2014)

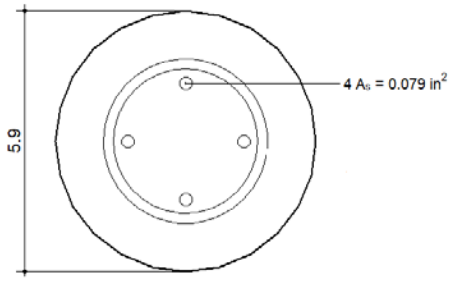

Figure 5.27: Siddiqui et al. (2014) Cross Section

f_y = 61 ksi

f_{yt} = 44 ksi

f'_c = 5.09 ksi

Axial force = 112.5 kips

One layer of CFRP

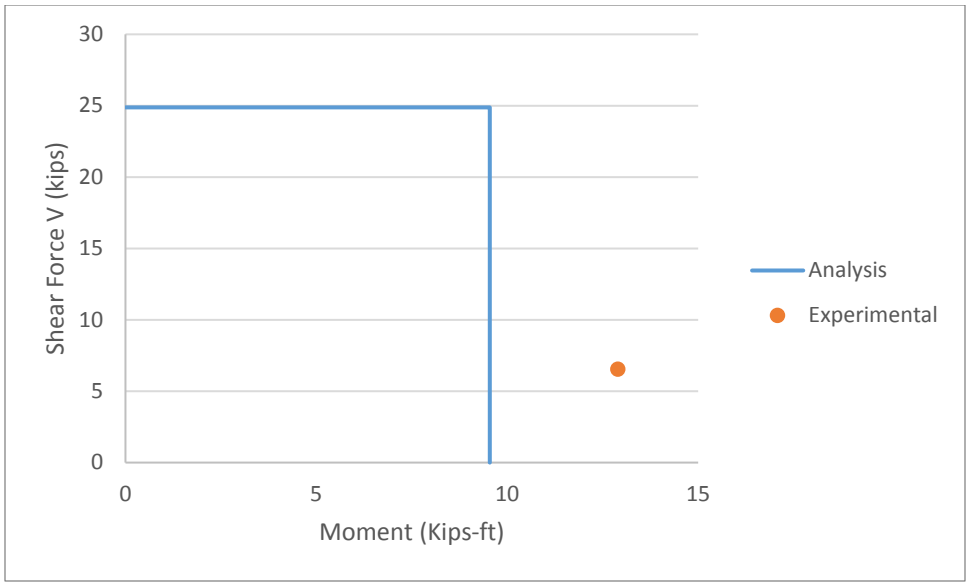

Figure 5.28: Siddiqui et al. (2014) Interaction Diagram (P=112.5 kips; One Layer of CFRP)

This column was tested by Siddiqui, Alsayed, Al-Salloum, Iqbal, and Abbas (2014) under 112.5 kips axial force. The section was strengthened by one layer of CFRP, fully wrapped over the column length. The proposed interaction diagram is conservative and fairly accurate comparing to the failure point.

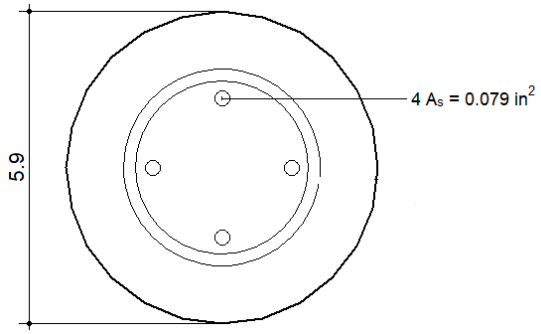

Figure 5.29: Siddiqui et al. (2014) Cross Section

f_y = 61 ksi

f_{yt} = 44 ksi

f'_c = 5.09 ksi

Axial force = 78.5 kips

One layer of CFRP

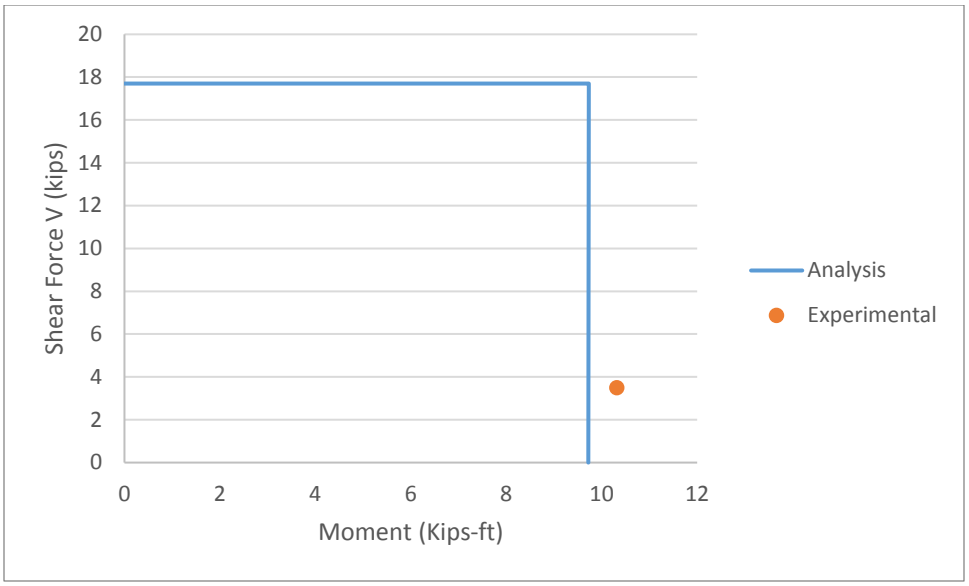

Figure 5.30: Siddiqui et al. (2014) Interaction Diagram (P=78.75 kips; One Layer of CFRP)

This column was tested by Siddiqui et al. (2014) under 78.75 kips axial force. The section was strengthened by one layer of CFRP, fully wrapped over the column length. The proposed interaction diagram is conservative and fairly accurate comparing to the failure point. The section failed in flexure with only 22% of its shear capacity.

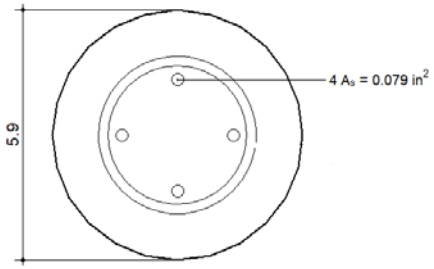

Figure 5.31: Siddiqui et al. (2014) Cross Section

f_y = 61 ksi

f_{yt} = 44 ksi

f'_c = 5.09 ksi

Axial force = 72.5 kips

One layer of CFRP

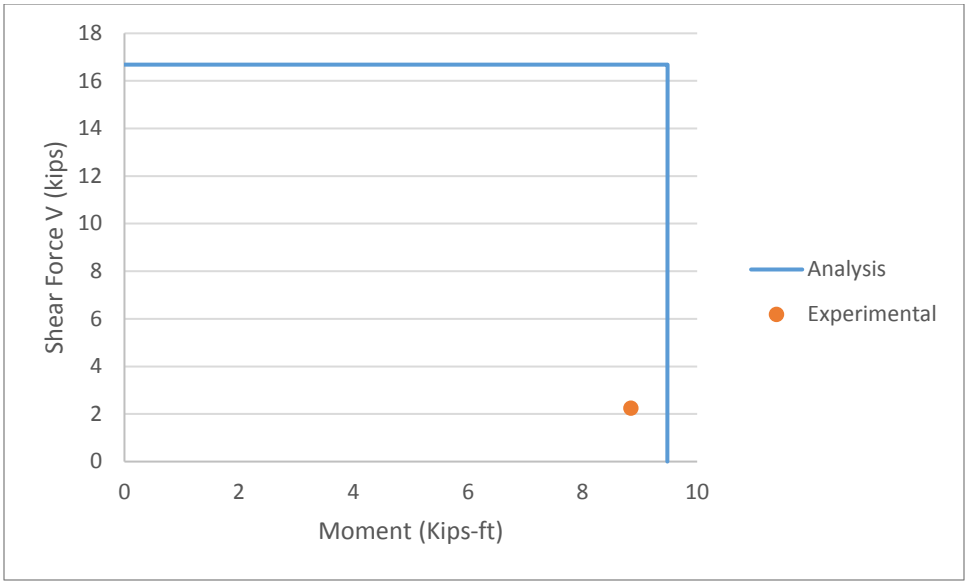

Figure 5.32: Siddiqui et al. (2014) Interaction Diagram (P=72 kips; One Layer of CFRP)

This column was tested by Siddiqui et al. (2014) under 72 kips axial force. The section was strengthened by one layer of CFRP, fully wrapped over the column length. The proposed interaction diagram is fairly accurate comparing to the failure point. Although the axial force was reduced by only 7 kips, the failure experimental bending moment strength was reduced by 20%.

5.4 Parametric Study

In this section, a parametric study is presented to examine the effect of changing the geometrical, material, and loading parameters on the Moment-Shear Force interaction diagram. The geometrical parameters are the cross-sectional diameter, longitudinal bar area, and transverse steel spacing. The material parameters include concrete compressive strength, steel yielding strength, and FRP material (CFRP and GFRP), as well as the number of plies. The sections were subject to four relative levels of axial load.

Table 5.4 shows the FRP parameters used in this parametric study. The cross-sectional diameter was varied between 28, 36, and 44 inches. Steel ratios was varied between 0.01, 0.1025, and 0.015. For transverse steel spacing, 2 inches and 4 inches were considered. For materials, the compressive concrete strength varied between 4, 6, and 8 ksi. For steel yielding strength, 45, 60, and 72 ksi were taken. Number of FRP plies were varied between 1, 2, 3, 4, and 5 plies. The applied

axial force was relative to each section. Four levels of axial force were considered for each section Max P, two-thirds of Max P, one-third of Max P, and zero.

$$Max\ P = 0.85(A_c - A_s)f_c' + A_s f_y$$

Where:

A_c= Cross sectional area (in.^{2})

A_s= Total Longitudinal steel area (in.^{2})

Table 5.4: Parametric Study FRP Properties

Type	E_f (ksi)	ε_{cu}	Thickness (in.)
CFRP	9450	0.011	0.04
GFRP	3430	0.022	0.04

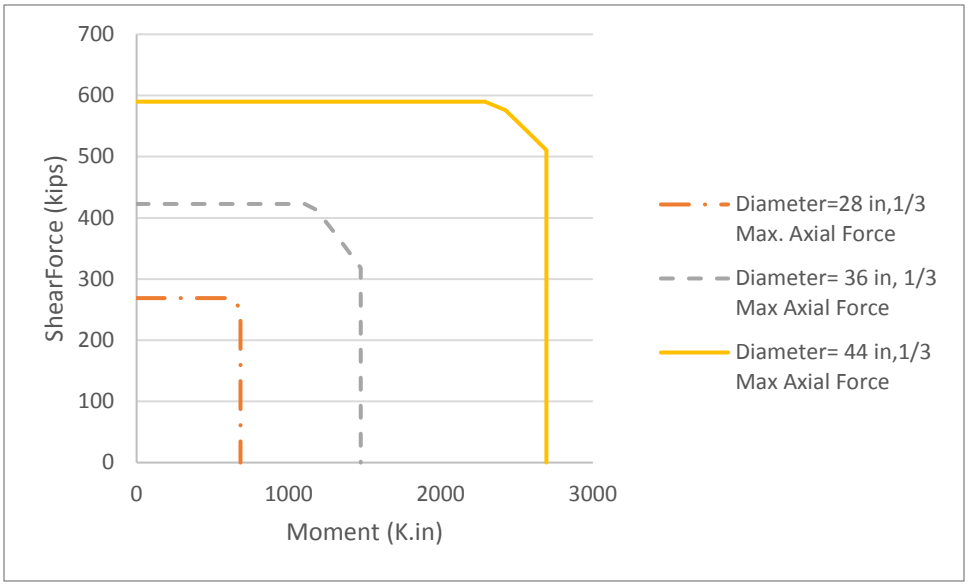

Figure 5.33: Shear Force-Bending Moment Interaction Diagram (Steel Ratio=0.01; One Layer of GFRP; Different Cross-Sectional Diameter)

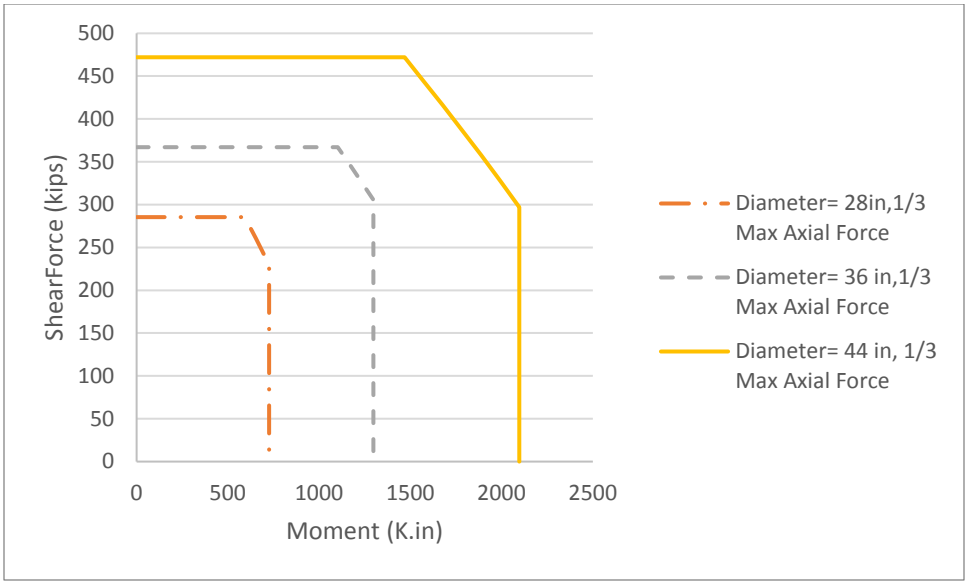

Figure 5.34: Shear Force-Bending Moment Interaction Diagram (Steel Ratio=0.0125; One Layer of GFRP; Different Cross-Sectional Diameter)

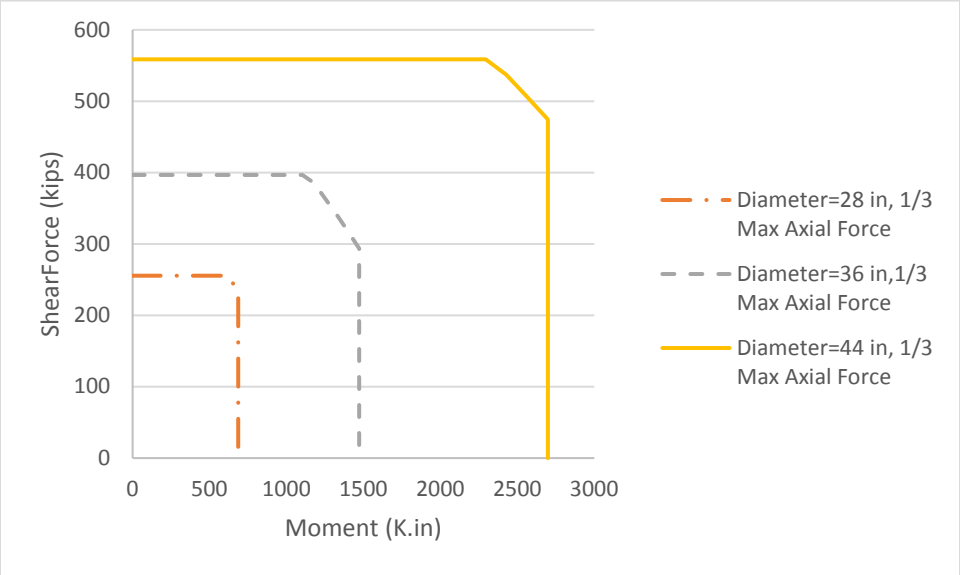

Figure 5.35: Shear Force-Bending Moment Interaction Diagram (Steel Ratio=0.01; One Layer of CFRP; Different Cross-Sectional Diameter)

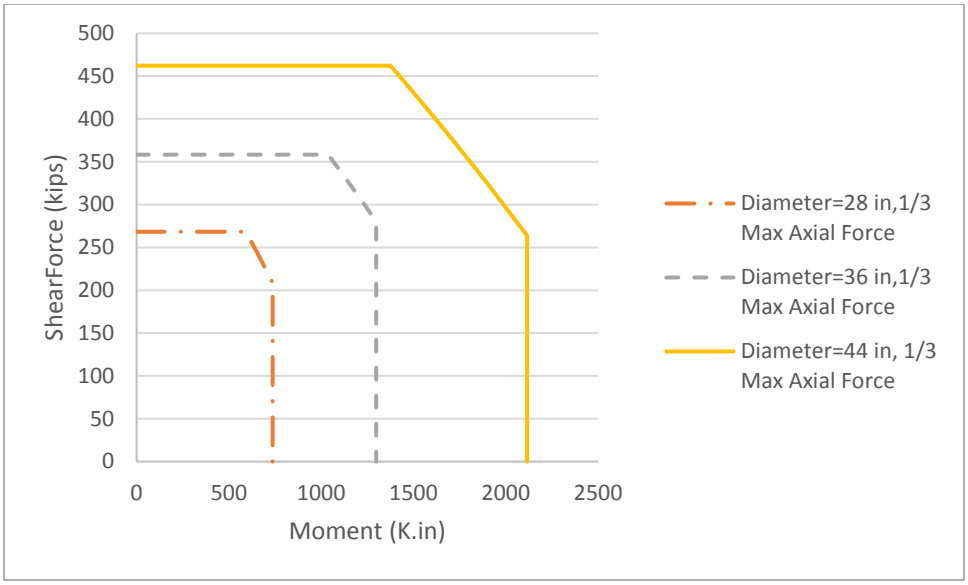

Figure 5.36: Shear Force-Bending Moment Interaction Diagram (Steel Ratio=0.0125; One Layer of CFRP; Different Cross-Sectional Diameter)

The first varied parameter is the cross-sectional diameter. The diameter was varied between 28, 36, and 44 inches. By increasing the cross-sectional diameter, the moment capacity and shear capacity shows a big improvement. For different longitudinal steel ratio and FRP materials, adding 8 inches of diameter increased the shear strength of a section by 100 kips and pure moment capacity by 700–1,200 kips-in.

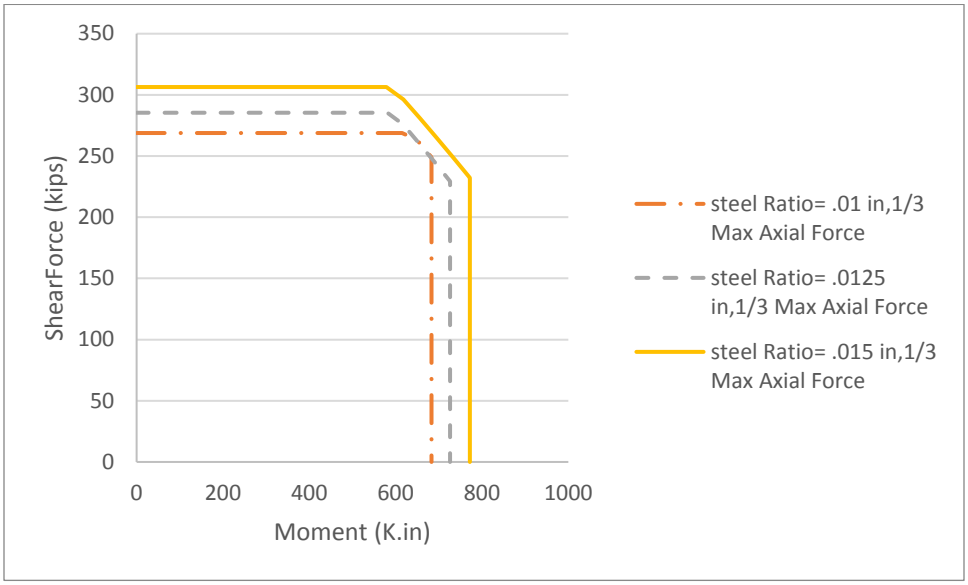

Figure 5.37: Shear Force-Bending Moment Interaction Diagram (Diameter=28 in.; One Layer of GFRP; Different Steel Ratios)

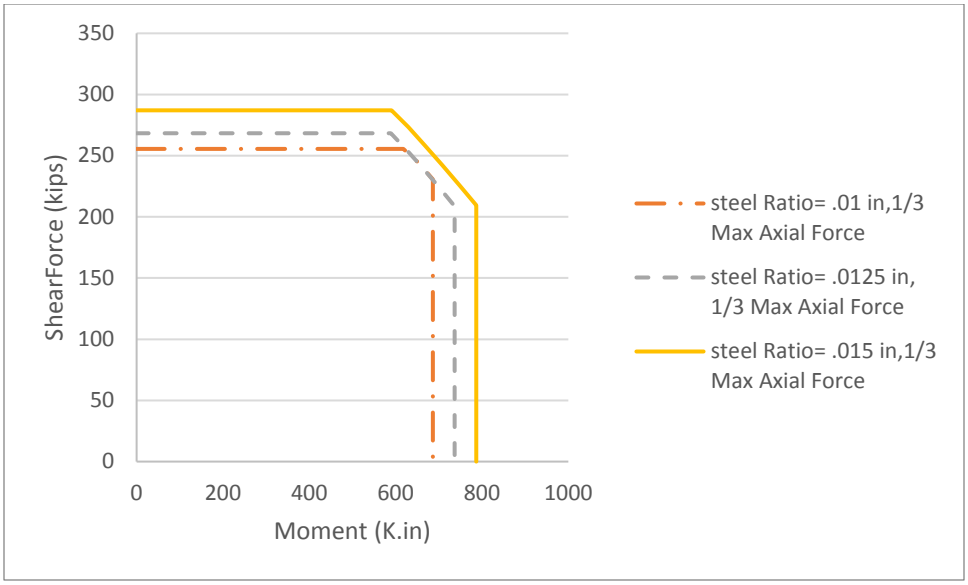

Figure 5.38: Shear Force-Bending Moment Interaction Diagram (Diameter=36 in.; One Layer of CFRP; Different Steel Ratios)

The second parameter examined was the longitudinal steel ratio. The ratio was varied between 0.01, 0.0125, and 0.015 inches. By increasing the cross-sectional diameter, the moment capacity and shear capacity show a slight improvement due to the applied relative axial force. Since the applied axial force is a function of the longitudinal steel ratio, the improvement of shear and moment capacities are limited.

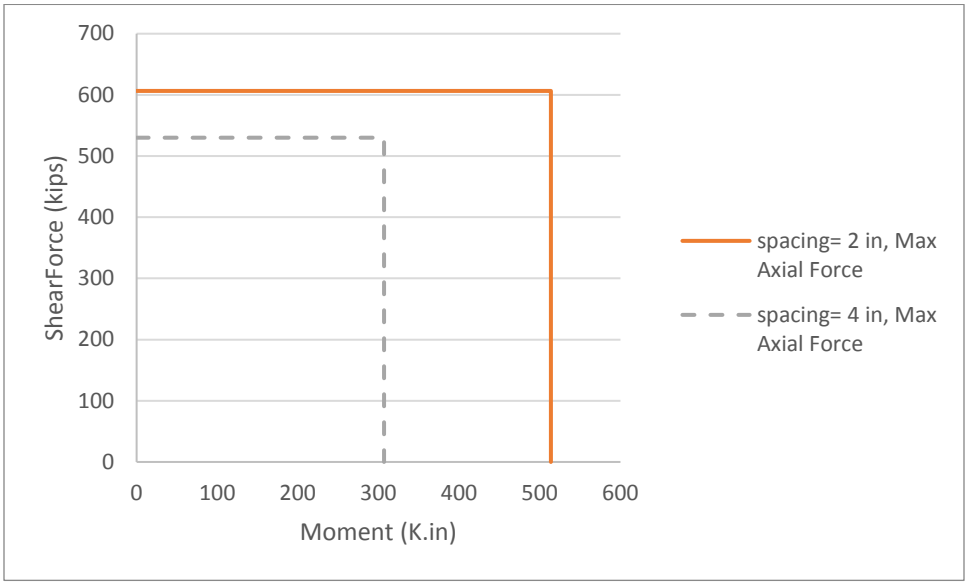

Figure 5.39: Shear Force-Bending Moment Interaction Diagram (Diameter=28 in.; One Layer of GFRP; Different Transverse Steel Spacing)

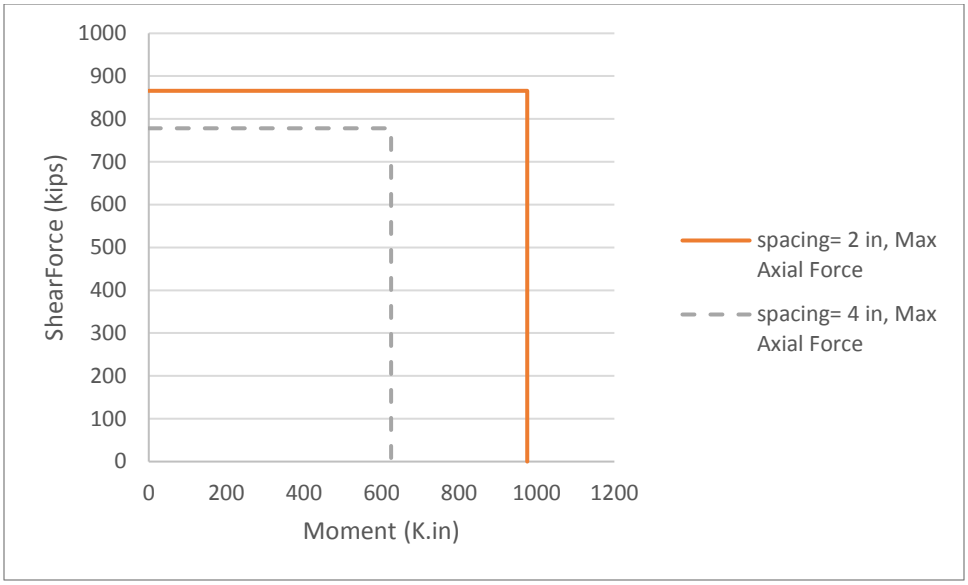

Figure 5.40: Shear Force-Bending Moment Interaction Diagram (Diameter=36 in.; One Layer of GFRP; Different Transverse Steel Spacing)

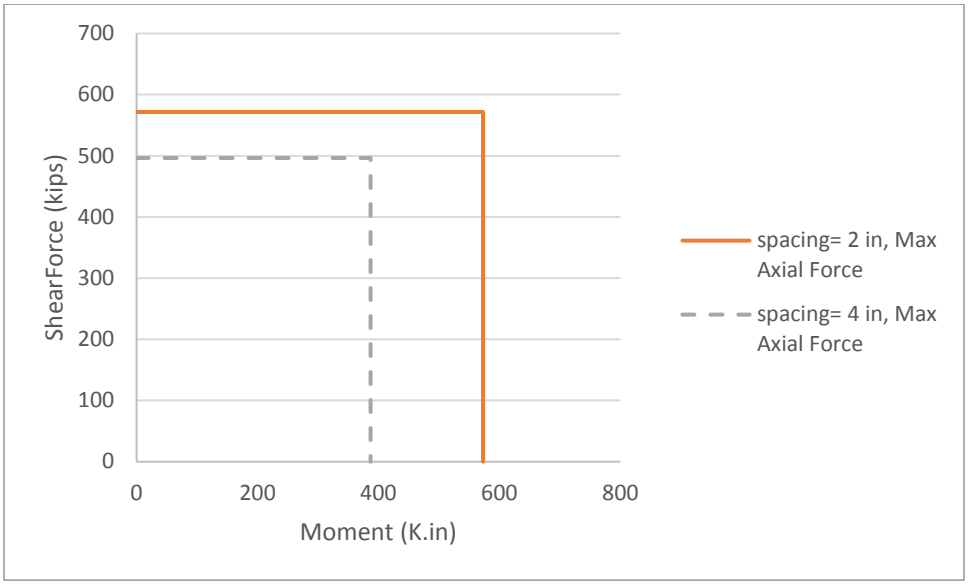

Figure 5.41: Shear Force-Bending Moment Interaction Diagram (Diameter=28 in.; One Layer of CFRP; Different Transverse Steel Spacing)

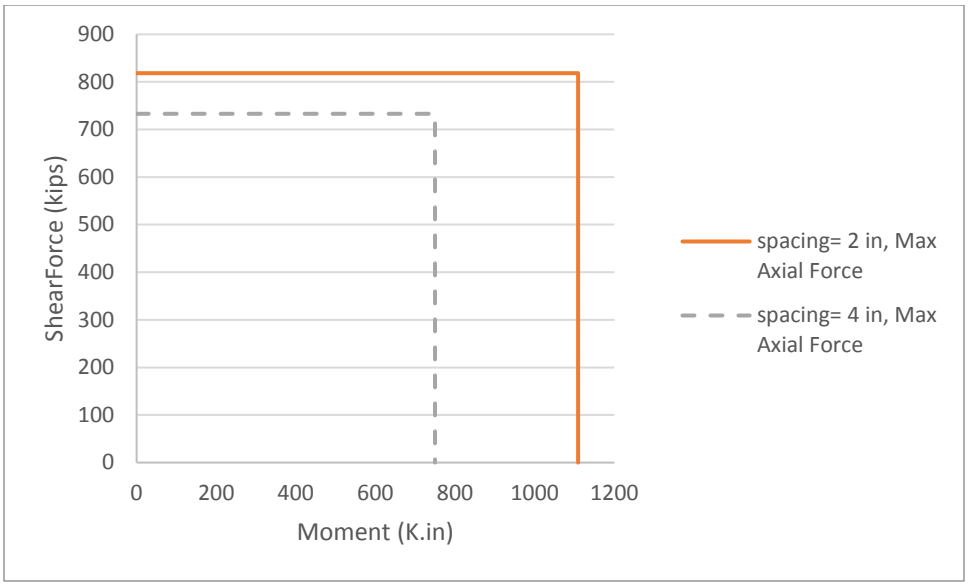

Figure 5.42: Shear Force-Bending Moment Interaction Diagram (Diameter=36 in.; One Layer of CFRP; Different Transverse Steel Spacing)

Transverse steel spacing is the third parameter and it was varied between 2 inches and 4 inches. Around 60 kips were the difference in shear capacity by using 2-inch spacing over 4-inch spacing. Also, 200 kips-in. increase were observed in pure moment capacity when using 2-inch transverse steel spacing over 4 inches, for a diameter of 28 inches. And 400 kips-in. increase were observed for 36-inch cross-sectional diameter.

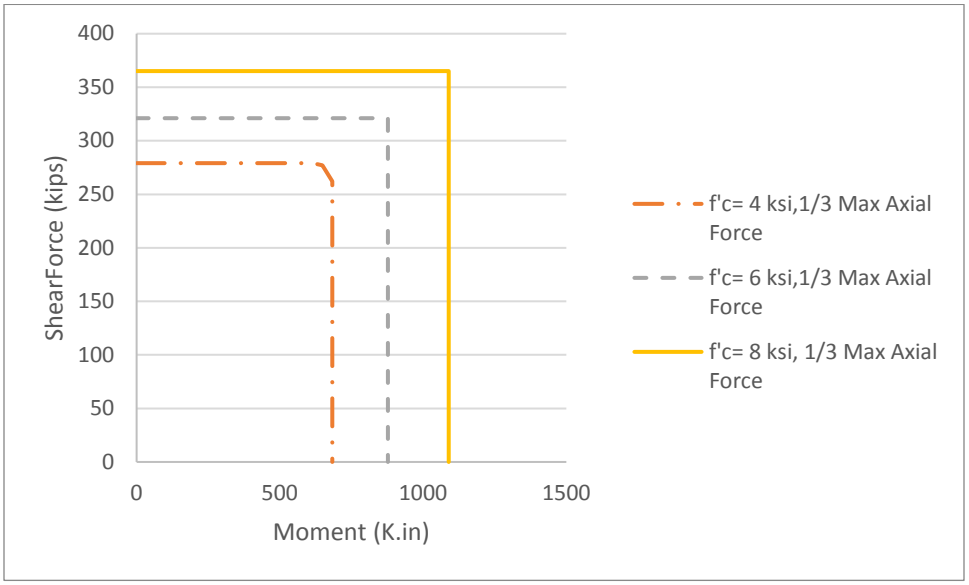

Figure 5.43: Shear Force-Bending Moment Interaction Diagram (Diameter=28 in.; Two Layers of GFRP; Different f'_c Values)

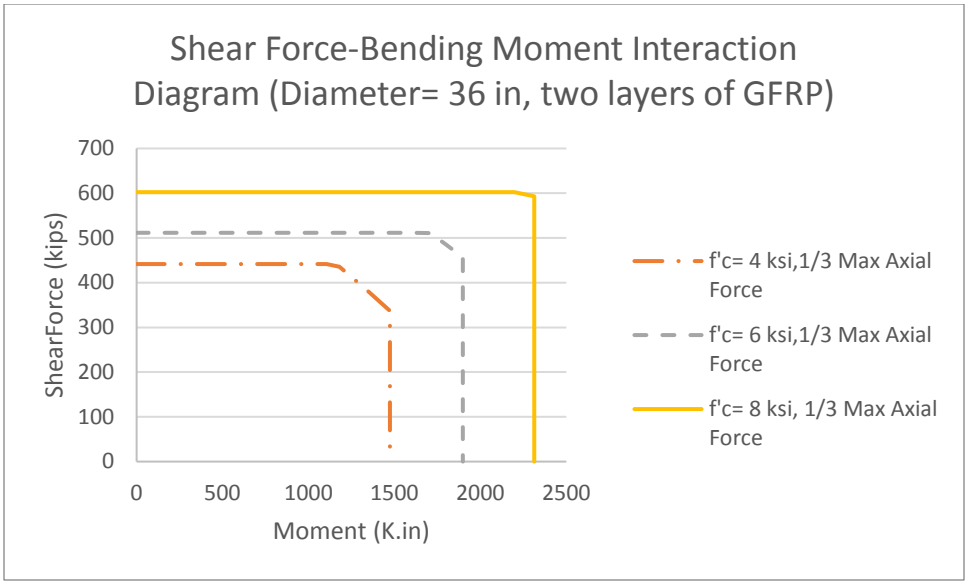

Figure 5.44: Shear Force-Bending Moment Interaction Diagram (Diameter=36 in.; Two Layers of GFRP; Different f'$_c$ Values)

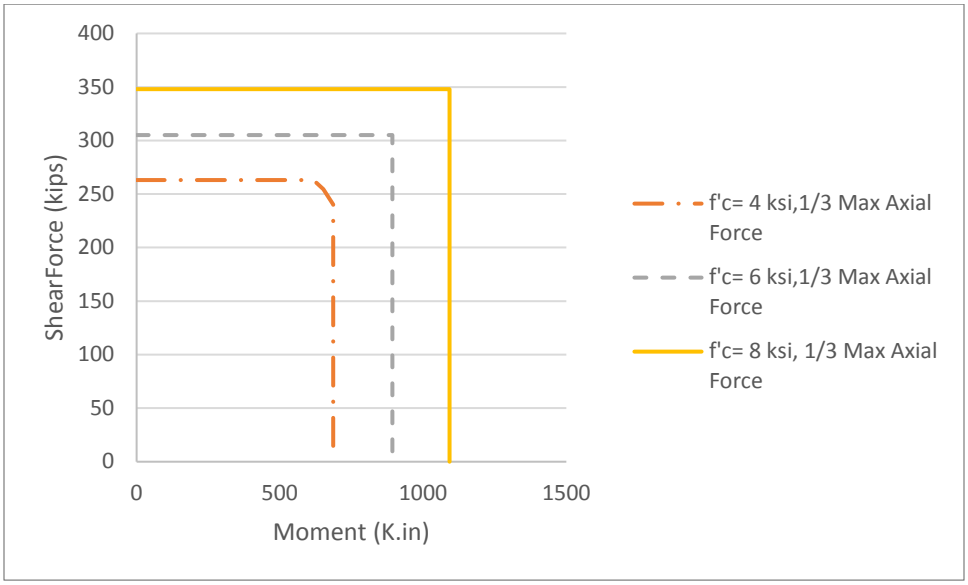

Figure 5.45: Shear Force-Bending Moment Interaction Diagram (Diameter=28 in.; Two Layers of CFRP; Different f'$_c$ Values)

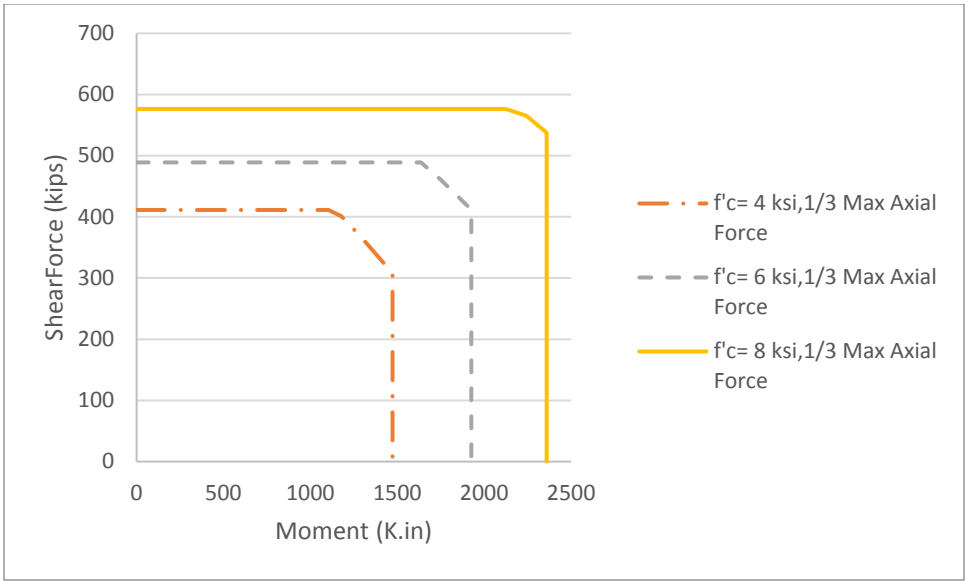

Figure 5.46: Shear Force-Bending Moment Interaction Diagram (Diameter=36 in.; Two Layers of CFRP; Different f'$_c$ Values)

The concrete compressive force was varied between 4, 6, and 8 ksi. A significant gain in strength is observed with increasing f'c. For 28-inch cross-sectional diameter and two layers of CFRP transverse reinforcement under one-third of the max axial load, a linear increase of 50 kips in pure shear strength and 200 kips-in. in pure flexural strength were observed for each 4 ksi increase in concrete compressive strength, while f'$_c$>4 ksi. The same trend was observed with different diameters and number of FRP plies.

By examining the behavior of different numbers of FRP plies (1, 2, 3, 4, and 5 plies) with different steel ratio and cross-sectional diameters, the gain in shear strength and moment capacity is limited after the first ply. Less than 10 kips increase were observed by increasing an FRP ply after the first ply.

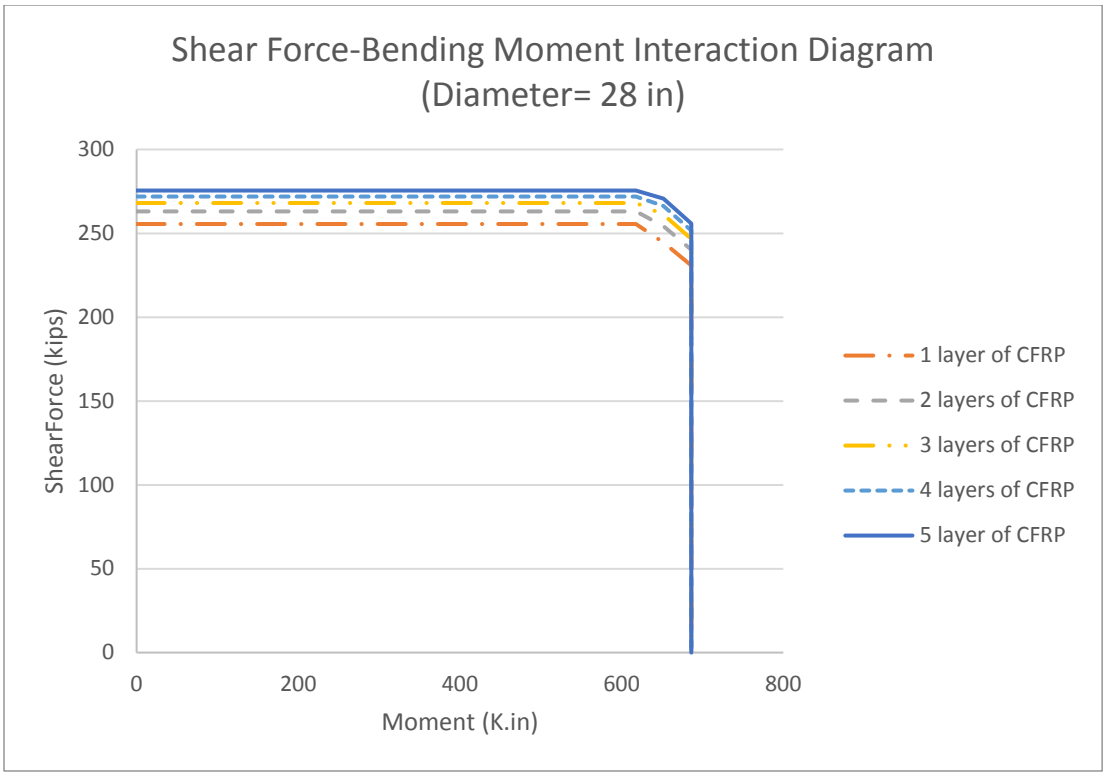

Figure 5.47: Shear Force-Bending Moment Interaction Diagram (Diameter=28 in.; Different Number of Plies)

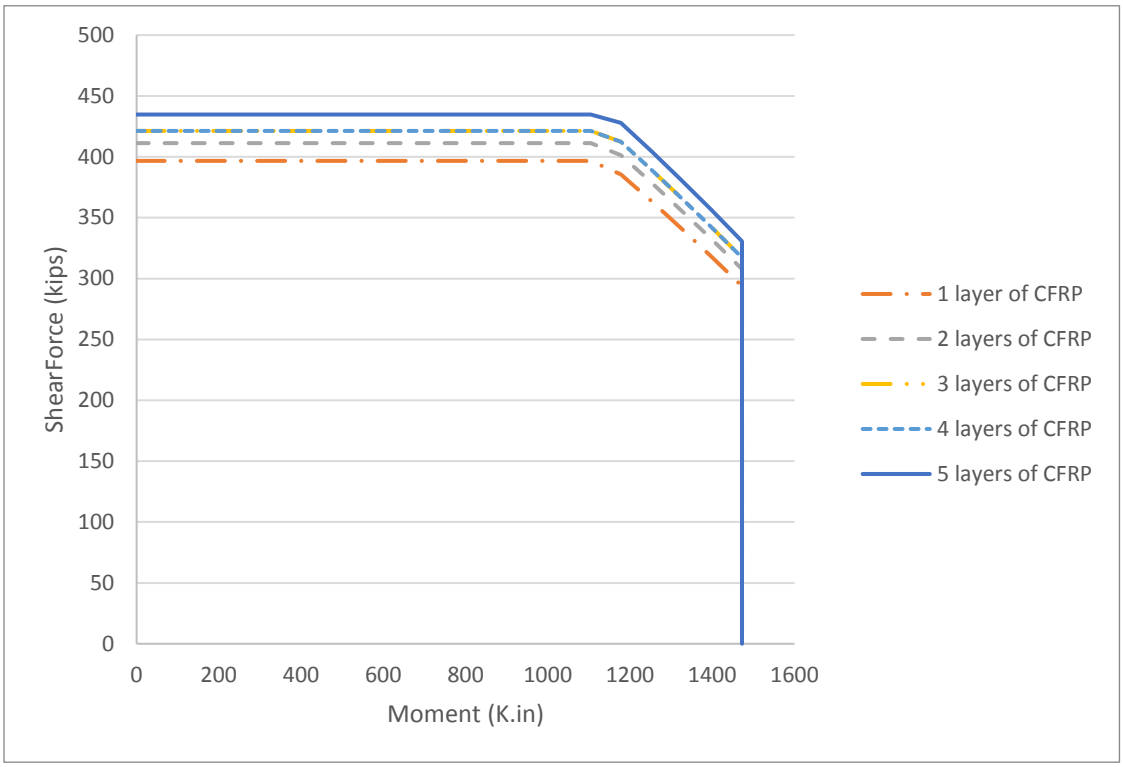

Figure 5.48: Shear Force-Bending Moment Interaction Diagram (Diameter=36 in.; Different Number of Plies)

Chapter 6: Software Development

6.1 Introduction

The proposed procedure was built into the software KDOT Column Expert (Rasheed, Abd El-Fattah, Esmaeily, Jones, & Hurst, 2012) in order to compute the full domain moment-shear-axial force interaction diagram for circular reinforced concrete column sections. KDOT Column Expert is an object-oriented program written within the framework of the visual C# language. This software can predict the steel confined and unconfined moment-axial force capacity for circular and rectangular sections. By adding the shear analysis to the software, KDOT Column Expert can predict the full domain of the sections under the three major loads (moment-axial-shear force combinations). In this chapter, input interface and output interface are discussed for circular sections for the cases where shear is a key design of the load combinations.

6.2 Input Interface

The input data is divided into four sub-sections. The geometrical properties are the first sub-section, including section diameter, clear cover, number of bars, longitudinal and transverse bars number, and spacing. The second sub-section is the concrete properties, including the concrete compressive strength and its corresponding strain, as well as the maximum strain. The third and the fourth sub-sections are for the longitudinal and transverse steel properties. Steel properties are Young's modulus and yielding strength of the steel. Additionally, the user has the option to choose the transverse steel order between the two main orders, spiral and hoops. Figure 6.1 shows the input properties interface of the section.

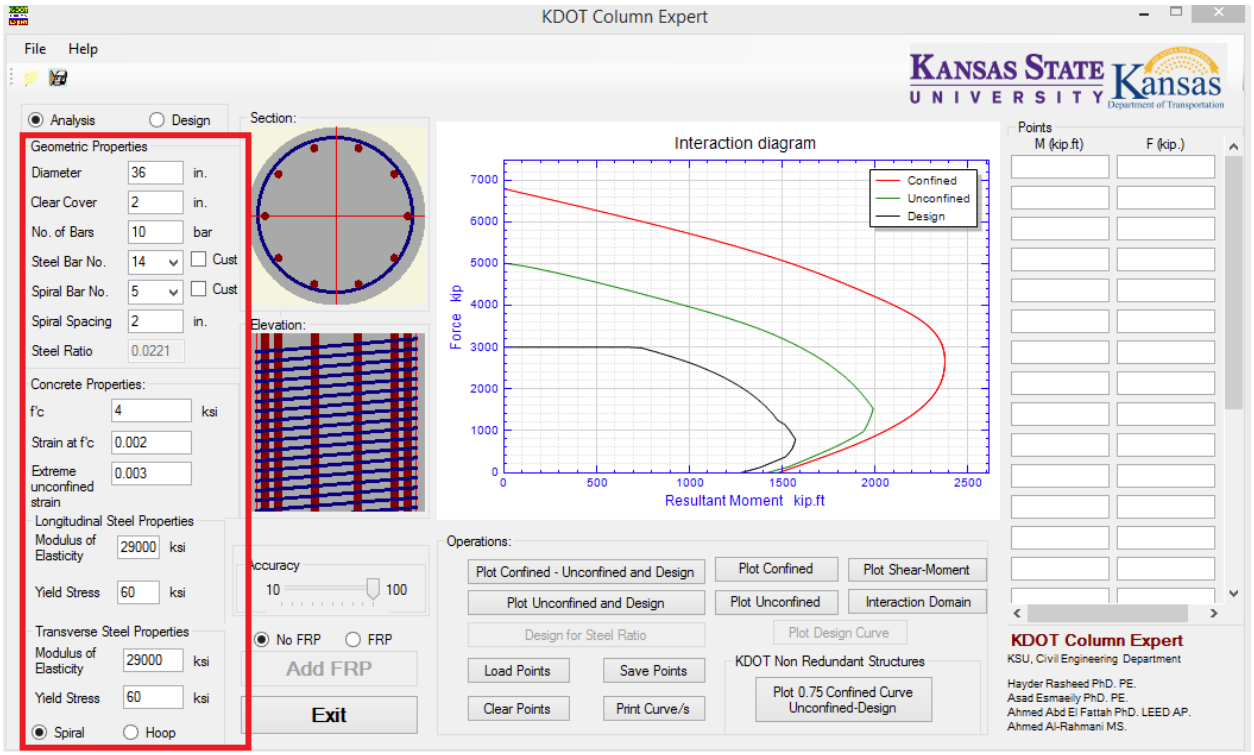

Figure 6.1: KDOT Column Expert Input Interface

The custom check box beside the steel bar textbox is to give the user the option to define the steel bar diameter if the bar diameter is not within the US rebar size charts (see Figure 6.2).

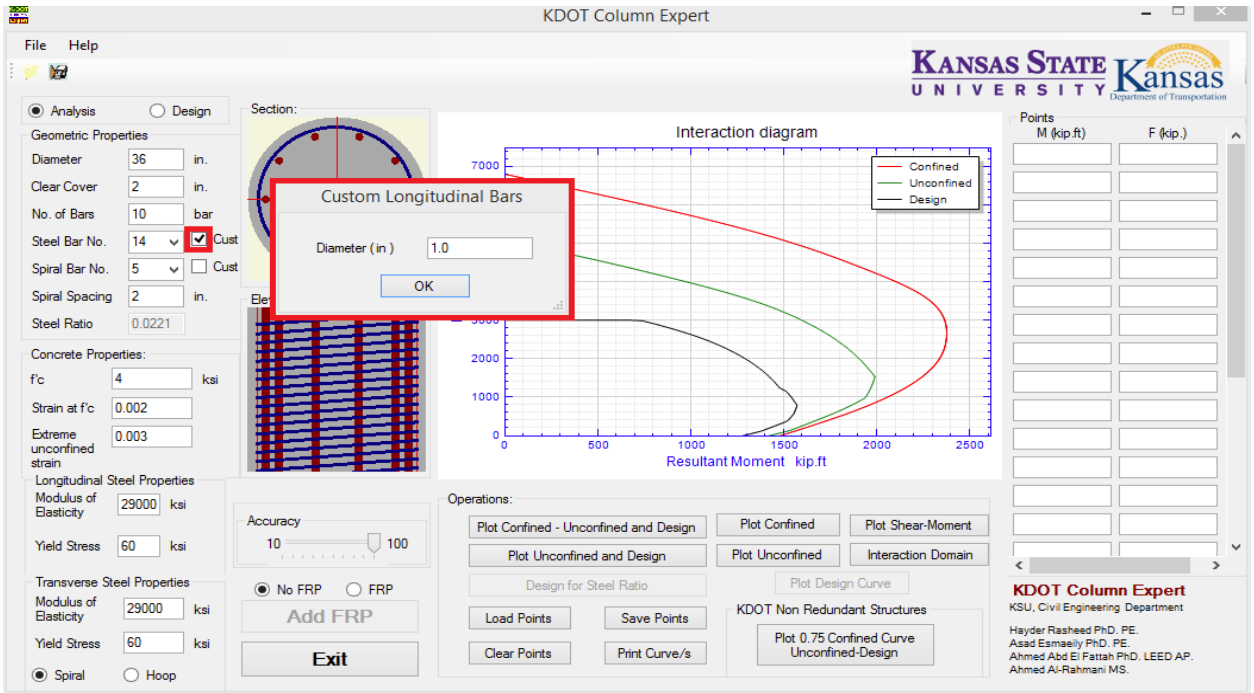

Figure 6.2: KDOT Column Expert Custom Bars Input

Figure 6.3 shows FRP parameters input window. These parameters are E_f, ε_{fu}, thickness, and number of layers. Also this window includes some manufactured FRP parameters.

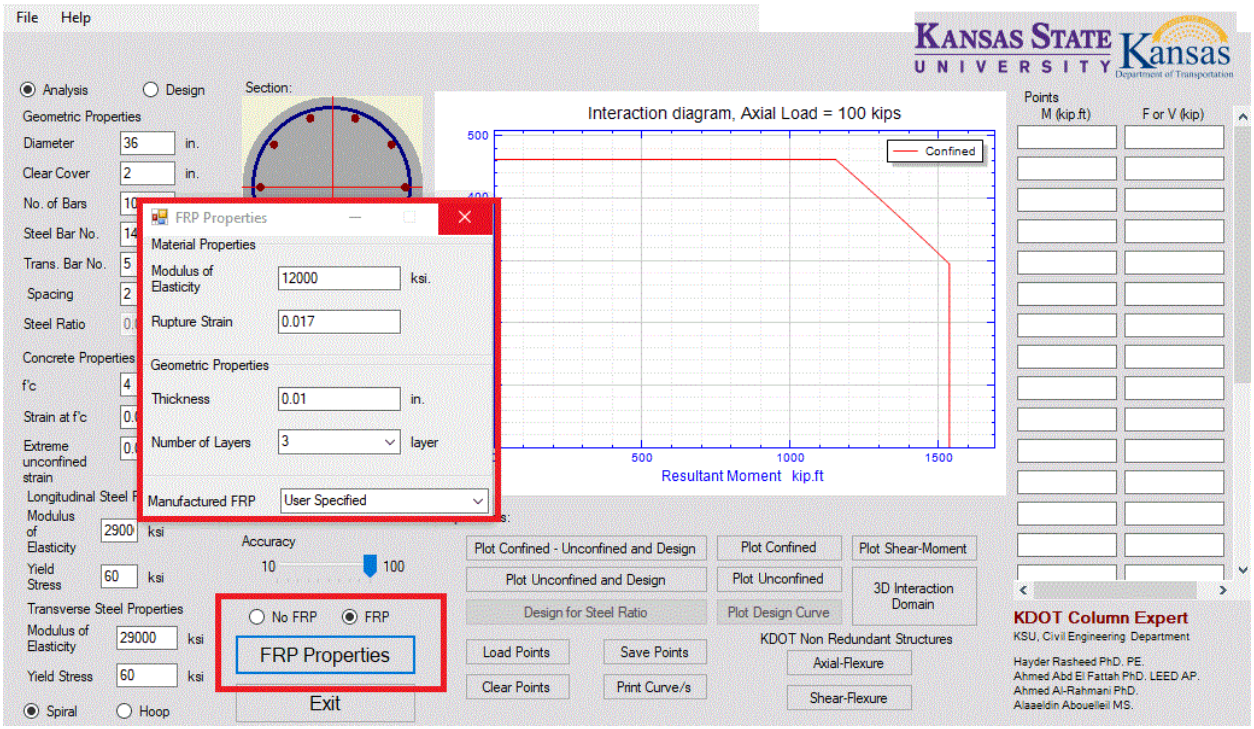

Figure 6.3: KDOT Column Expert FRP Parameters Input Window

6.3 Output Interface

The default output interaction diagram is the moment versus axial force with zero shear value (see Figure 6.1). It shows the steel confined (red curve) and unconfined (green curve) section capacities.

In order to account for the shear calculations, the “Plot Shear-Moment” button was added. This button generates the interaction diagram for moment and shear force at a constant axial force defined by the user (see Figure 6.4). Figure 6.6 shows the final output of “Plot Shear-Moment” button for constant axial force. The full domain could be generated using “Interaction Domain” button where the calculation in “Plot Shear-Moment” is repeated for a series of axial forces up to the maximum confined axial load capacity. Figure 6.7 shows the full domain of moment-axial force-shear force combination.

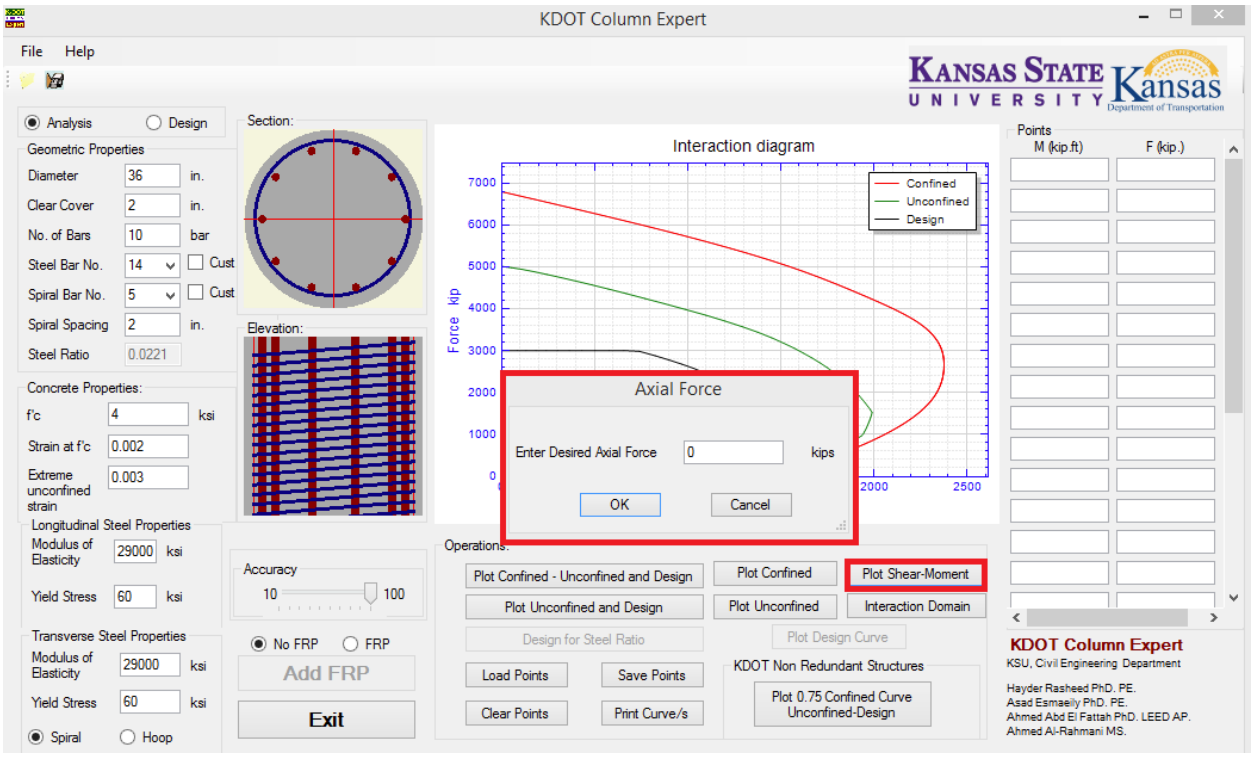

Figure 6.4: KDOT Column Expert Axial Force Input

If FRP button is activated, the window in Figure 6.5 will appear to let the user determine the FRP reinforcement scheme, FRP sheet length, and spacing.

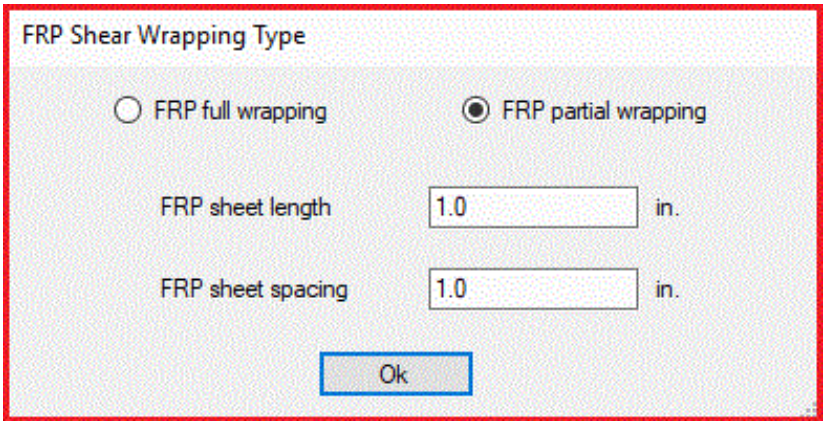

Figure 6.5: KDOT Column Expert FRP Scheme Input Window

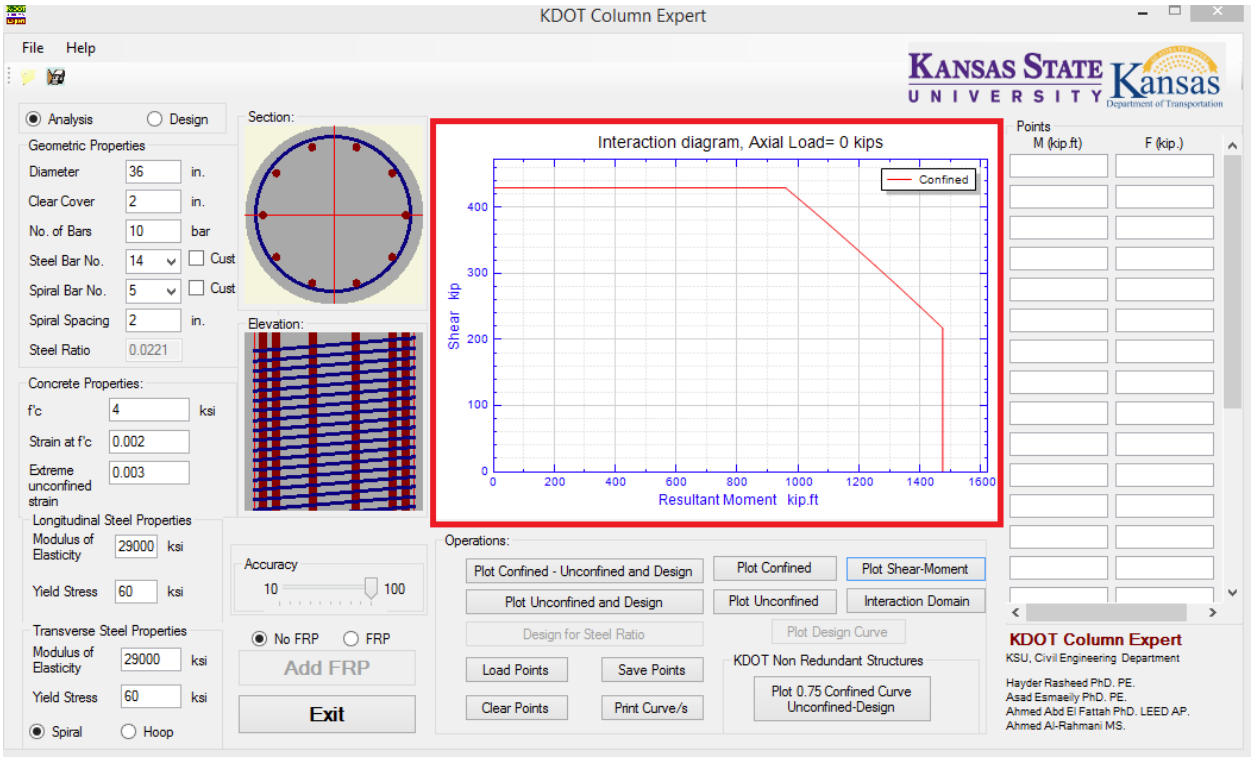

Figure 6.6: KDOT Column Expert 2D Moment-Shear Interaction Diagram

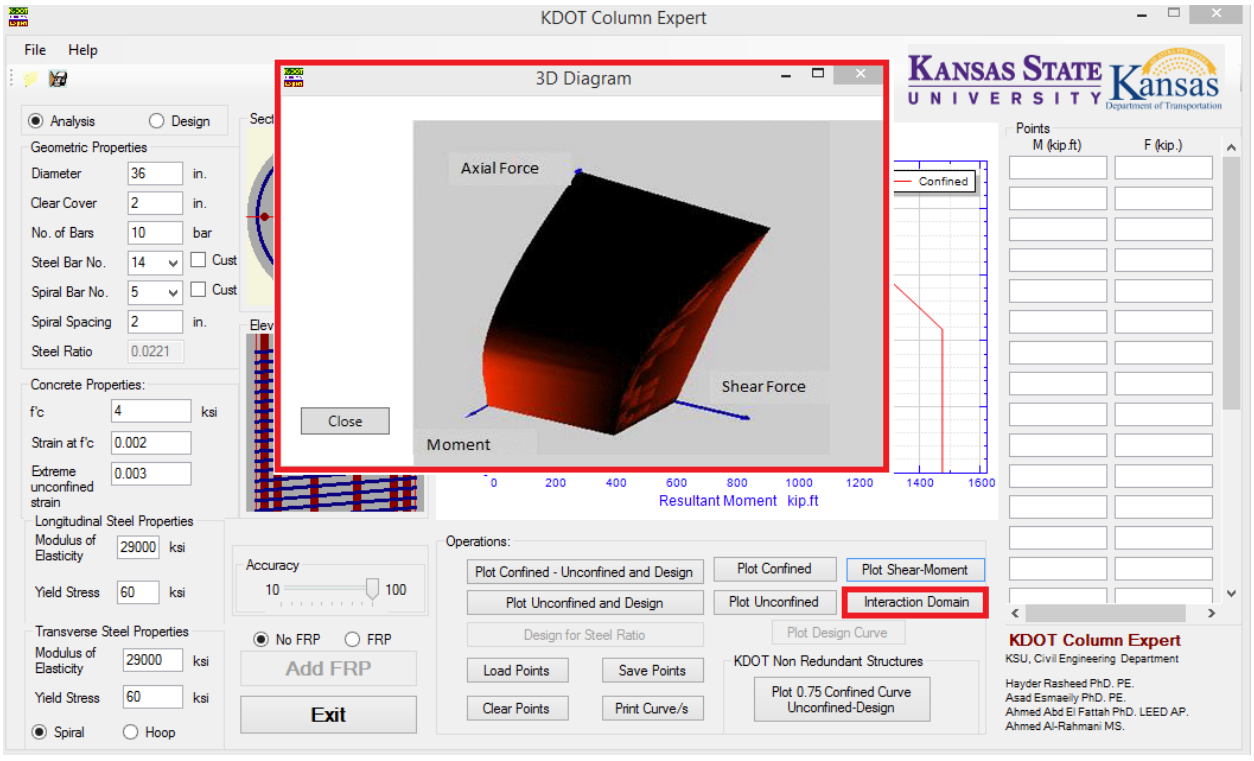

Figure 6.7: KDOT Column Expert 3D Domain

In the case of sections having transverse steel less than the minimum transverse steel defined by AASHTO LRFD, the user is asked to provide a value of maximum aggregate size (see Figures 6.8 and 6.9).

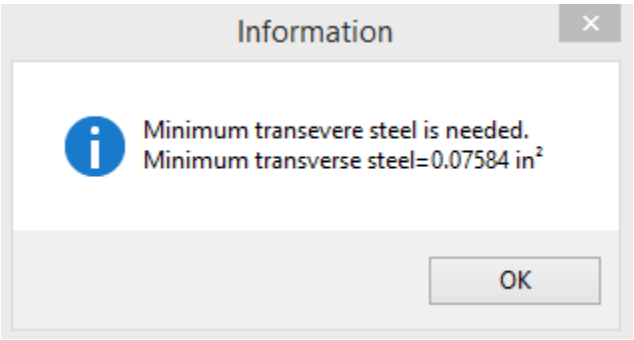

Figure 6.8: Minimum Transverse Steel

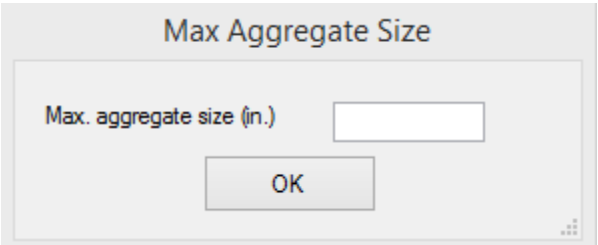

Figure 6.9: Maximum Aggregate Size Input

There are three cases in which AASHTO LRFD consider the section invalid and ask to change the properties of the section. In KDOT Column Expert, the user is notified to change the section properties if any of these cases matched. The first case happens if the transverse steel spacing exceeded the maximum; in this case, the message shown in Figure 6.10 appears and the analysis stops.

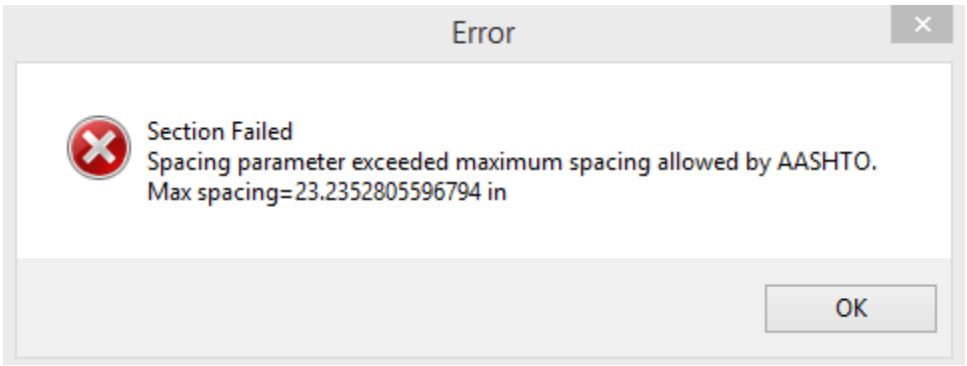

Figure 6.10: Maximum Spacing Error Message

The second case is to make sure that the section has enough longitudinal steel to resist cracks in case of sections having transverse steel less than the minimum transverse steel defined by AASHTO LRFD. Figure 6.11 shows KDOT Column Expert message to the user in this case.

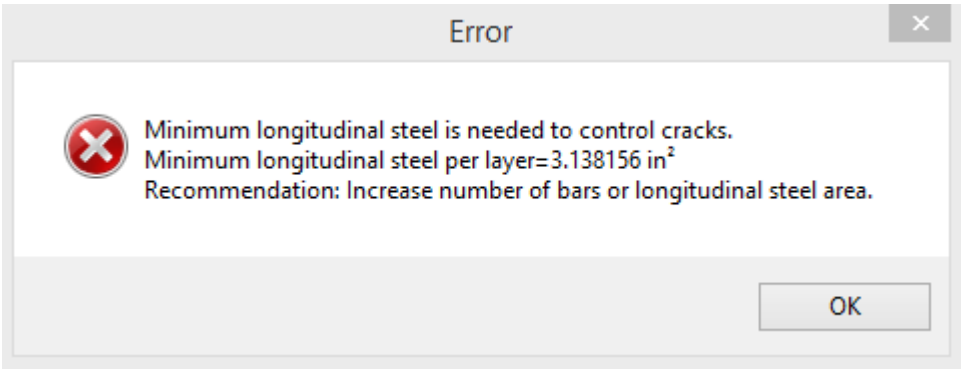

Figure 6.11: Lack of Longitudinal Steel Error

The third case is to confirm that the transverse steel yielding strength is less than 100 ksi. This limit is established to have a clear yielding zone in the steel stress-strain curve. If the transverse steel yielding strength exceeded 100 ksi, the yielding zone vanishes. Figure 6.12 shows the KDOT Column Expert message to the user in this case.

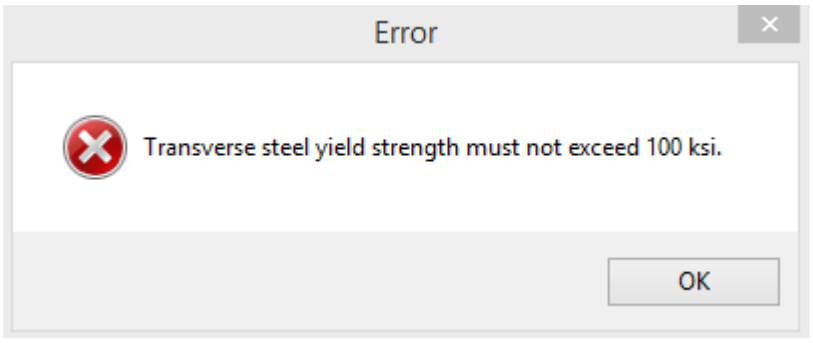

Figure 6.12: Transverse Steel Exceeded 100 ksi Error

Chapter 7: Conclusions

In this study, a formulation conforming to AASHTO (2014) *LRFD Bridge Design Specifications* is developed to predict the axial force-shear-moment interaction diagrams of circular confined concrete bridge pier sections reinforced with FRP. Comparisons with a large database of experiments indicate the accuracy of the resulting diagrams. A further step was taken to improve the accuracy of the calculations.

Transverse steel area, spacing, cross section diameter, and applied axial force are the main keys to analyze and increase the shear capacity of the cross section. Treating the cracked concrete as a new different material proved to be a beneficial approach to predict the sections' capacities and behaviors.

Using transverse reinforcement of FRP shows a significant improvement for axial force-bending moment and shear force capacities. The reader is also directed to use KDOT Column Expert for more accurate prediction of the interaction diagrams.

References

Abd El-Fattah, A., Rasheed, H. A., & Esmaeily, A. (2011). A new eccentricity-based simulation to generate ultimate confined interaction diagrams for circular concrete columns. *Journal of the Franklin Institute, 348*(7), 1163–1176.

ACI Committee 318. (2011). *Building code requirements for structural concrete*. Farmington Hills, MI: American Concrete Institute.

American Association of State Highway and Transportation Officials (AASHTO). (2014). *AASHTO LRFD bridge design specifications* (7th ed.). Washington, DC: Author.

Belarbi, A., Bae, S.-W., Ayoub, A., Kuchma, D., Mirmiran, A., & Okeil, A. (2011). *Design of FRP systems for strengthening concrete girders in shear* (NCHRP Report 678). Washington, DC: Transportation Research Board.

Bentz, E. C., Vecchio, F. J., & Collins, M. P. (2006). Simplified modified compression field theory for calculating shear strength of reinforced concrete elements. *ACI Structural Journal, 103*(4), 614–624.

Ghee, A. B., Priestley, M. J. N., & Paulay, T. (1989). Seismic shear strength of circular reinforced concrete columns. *ACI Structural Journal, 86*(1), 45–59.

Kawashima, K., Hosotani, M., & Yoneda, K. (2000) Carbon fiber sheet retrofit of reinforced concrete bridge piers. In *Proceedings of the International Workshop on Annual Commemoration of Chi-Chi Earthquake, Vol. II - Technical Aspect* (pp. 124–135). Taipei, Taiwan, ROC: National Center for Research on Earthquake Engineering.

Liu, J., & Sheikh, S. A. (2013). Fiber-reinforced polymer-confined circular columns under simulated seismic loads. *ACI Structural Journal, 110*(6), 941–952.

Rasheed, H. A., Abd El-Fattah, A. M., Esmaeily, A., Jones, J. P., & Hurst, K. F. (2012). Software for adaptable eccentric analysis of confined concrete circular columns. *Computers and Concrete, 10*(4), 331–347.

Shahrooz, B. M., Miller, R. A., Harries, K. A., & Russell, H. G. (2011). *Design of concrete structures using high-strength steel reinforcement* (NCHRP Report 679). Washington, DC: Transportation Research Board.

Siddiqui, N. A., Alsayed, S. H., Al-Salloum, Y. A., Iqbal, R. A., & Abbas, H. (2014). Experimental investigation of slender circular RC columns strengthened with FRP composites. *Construction and Building Materials, 69*, 323–334.

Vecchio, F. J., & Collins, M. P. (1986). The modified compression-field theory for reinforced concrete elements subjected to shear. *ACI Journal Proceedings, 83*(2), 219–231.

Walraven, J. C. (1981). Fundamental analysis of aggregate interlock. *Journal of the Structural Division, 107*(11), 2245–2270.

K-TRAN

KANSAS TRANSPORTATION RESEARCH AND NEW-DEVELOPMENT PROGRAM

AD ASTRA PER ASPERA

Kansas

Department of Transportation